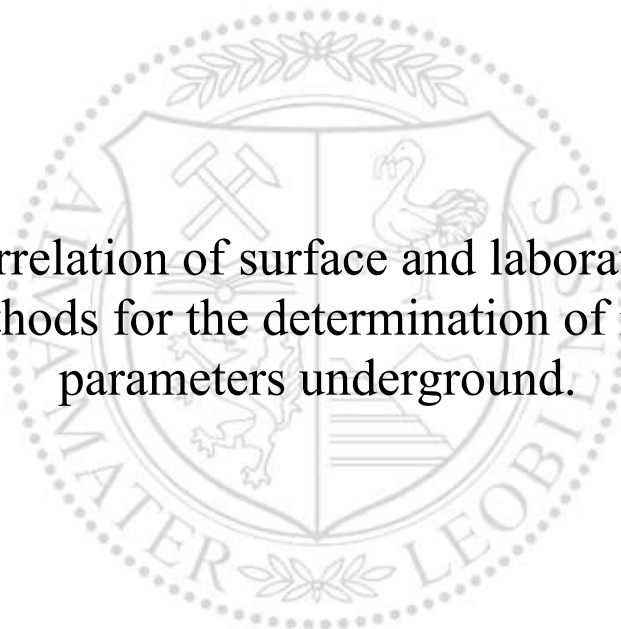




Chair of Subsurface Engineering

Master's Thesis



Correlation of surface and laboratory
methods for the determination of rock
parameters underground.

Dominik Kumertz, BSc

May 2024



AFFIDAVIT

I declare on oath that I wrote this thesis independently, did not use any sources and aids other than those specified, have fully and truthfully reported the use of generative methods and models of artificial intelligence, and did not otherwise use any other unauthorized aids.

I declare that I have read, understood and complied with the "Good Scientific Practice" of the Montanuniversität Leoben.

Furthermore, I declare that the electronic and printed versions of the submitted thesis are identical in form and content.

Date 08.05.2024

A handwritten signature in blue ink, consisting of a large, stylized 'D' followed by a long horizontal stroke.

Signature Author
Dominik Kumertz

Acknowledgement

I would like to take this opportunity to thank all the people who have supported me in writing this master's thesis!

Special gratitude belongs to my supervisor assoz. Prof. Marlene Villeneuve, PhD, who always provided me with help and advice to realize my ideas. I am also grateful for all the support from the University of Leoben, the Chair of Subsurface Engineering, the Zentrum am Berg and the Chair of Applied Geophysics.

Ao. Univ.-Prof. Dr. phil. Robert Scholger, Andrew Greenwood, MSc, PhD and Jörg Krainz helped me immensely with the data collection, processing and by giving me advice, for which I am very thankful.

I would also like to thank everyone who helped me with the collection of data and samples, as well as the processing and evaluation, in particular Ralf Neumeier, Ruben Winstel and my family.

To conclude, I want to thank St. Barbara for her protection underground and for the accident-free completion of the study.

Zusammenfassung

Die Herstellung von untertägigen Bauwerken in bestehende Stollensysteme stellt die Planer vor eine Vielzahl an Herausforderungen. Die Aufzeichnungen zum Bau sind oft mangelhaft und es muss daher eine Bewertung anhand des Ist-Zustands durchgeführt werden.

Diese Arbeit beschäftigt sich mit einem Seitenarm des Presserstollens im steirischen Erzberg, der Teil des Zentrums am Berg (ZaB) ist. Ziel ist die geotechnische Bewertung eines rund 55 m langen Stollens mit rund 3,5 m Durchmesser, der mit Stahlbögen und Holz ausgebaut ist. Aufgrund der unklaren Stabilitätsverhältnisse konnten bisher keine Messungen am bzw. hinter dem Verbau durchgeführt werden, weswegen sich der Schwerpunkt der Arbeit auf die Sohle konzentriert.

Die Untersuchungsmethoden lassen sich in drei Bereiche gliedern: Laboruntersuchungen mit Locker- und Festgesteinsproben, Geophysik und die Bewertung der Deformation der Stahlbögen. Im Labor konnten Sieblinien, Abrassivität, elektrischer Widerstand, p-Wellen Geschwindigkeit sowie Festigkeitsparameter (Triaxialtest, Point Load Test) bestimmt werden. In der Geophysik kamen Electrical Resistivity Tomography (ERT) und Refraktionsseismik zum Einsatz, um Störungzonen und die Tiefe der gestörten Zone zu ermitteln. Die Bewertung der Deformation erfolgte anhand genauer Beobachtung und Auswertung der an den Stahlbögen erkennbaren Verformung.

Die Ergebnisse der Laboruntersuchungen zeigen ein deutlich geschiefertes Gestein, das über eine geringe Festigkeit verfügt und abhängig von der Orientierung stark unterschiedliche Eigenschaften aufweist. Die geophysikalischen Untersuchungen zeigen zumindest zwei Störungzonen, die den Stollen queren und eine gestörte Zone mit rund vier Meter Tiefe, die zu beiden Enden des untersuchten Abschnitts weniger stark ausgeprägt ist. Aus der Bewertung der Deformation gehen zwei Störungen hervor, denen ein Clar-Wert zugeordnet werden kann. Außerdem ist sowohl eine geringere Spannung im Liegenden der Störungen zu sehen, als auch die Übernahme der Lasten nahe der Ortsbrust durch diese.

Insgesamt zeigt sich eine gute Korrelation der verwendeten Verfahren. Insbesondere die Beobachtung der Deformation liefert im Verhältnis zum benötigten Aufwand eine sehr gute Aussage über die angetroffenen Strukturen. Die Ergebnisse sind zudem abhängig von persönlicher Einschätzung und Erfahrung, was eine zweite Methode zur Verifizierung der Ergebnisse erfordert. In diesem Bereich könnten weitere Forschungsergebnisse und genauere Vorgehensweisen zur Beobachtung helfen, die Ergebnisse in ihrer Qualität zu verbessern.

Abstract

The construction of underground structures in existing tunnel systems poses a number of challenges for planners. The construction records are often inadequate and an assessment must be carried out based on the existing condition.

This thesis deals with a branch of the Presserstollen in the Styrian Erzberg, which is part of the Zentrum am Berg (ZaB). The objective is the geotechnical evaluation of an approximately 55 m long adit with a diameter of around 3.5 m, that is lined with steel arches and wood. The work focuses on the invert, because the unclear stability conditions prevented any measurements on or behind the lining.

The methods used can be divided into three categories: laboratory tests on loose and solid rock samples, geophysics in the invert and evaluation of the deformation of the steel arches. Grain size distribution curves, abrasivity, electrical resistivity, p-wave velocity and strength parameters (triaxial test, point load test) were measured in the laboratory. In geophysics, electrical resistivity tomography (ERT) and refraction seismics were used to identify fault zones and the depth of the damaged zone. The tunnel deformation was assessed by closely observing and evaluating the deformation visible in the steel arches.

The results of the laboratory testing show a clearly schistose rock, which has low strength and, depending on the orientation, shows strong anisotropy in behavior. The geophysical surveys show at least two fault zones that cross the tunnel and a damaged zone with a depth of around 4 m, which is less pronounced at both ends of the section. Two faults also appear in the evaluation of the deformation. These can also be assigned a Clar value. In addition, the lower stress in the footwall of the faults can be clearly seen, as can the transfer of the loads near the face.

Overall, there is a high correlation between the methods used. In particular, the observation of the deformation provides a good indication of the geological structures encountered in relation to the effort required. On the other hand, the results are very dependent on personal assessment and experience, which requires a second method to verify the results. In this area in particular, further research results and more precise observation procedures could help to improve the quality of the data.

TABLE OF CONTENTS

<u>ACKNOWLEDGEMENT</u>	2
<u>ZUSAMMENFASSUNG</u>	4
<u>ABSTRACT</u>	5
<u>TABLE OF CONTENTS</u>	6
<u>1. INTRODUCTION</u>	9
1.1. PROJECT INTRODUCTION	9
1.2. GEOLOGICAL BACKGROUND	9
1.3. PRESSERSTOLLEN	10
1.3.1. HISTORY.....	10
1.3.2. SITE DESCRIPTION	12
<u>2. METHODS</u>	15
2.1. INTRODUCTION	15
2.2. FIELD METHODS	15
2.2.1. SAMPLING	15
2.2.2. GEODETIC SURVEY.....	17
2.2.3. 2D SEISMIC.....	18
2.2.4. ELECTRIC RESISTIVITY TOMOGRAPHY (ERT).....	19
2.2.5. DEFORMATION OBSERVATION	22
2.3. LABORATORY METHODS	24
2.3.1. SAMPLE PROCESSING	24
2.3.2. SIEVING.....	29
2.3.3. HELIUM-PYCNOMETER	30
2.3.4. ULTRASONIC VELOCITY	31
2.3.5. CERCHAR ABRASIVITY INDEX (CAI).....	32
2.3.6. RESISTIVITY MEASUREMENT.....	34
2.3.7. POINT LOAD TEST	35
2.3.8. BRAZILIAN TEST.....	40
2.3.9. TRIAXIAL TEST	42

3. RESULTS	44
3.1. FIELD METHODS	44
3.1.1. 2D ERT	44
3.1.2. 3D ERT	45
3.1.3. 2D SEISMIC	47
3.1.4. GEODESY	50
3.1.5. DEFORMATION OBSERVATION	52
3.2. LABORATORY METHODS	53
3.2.2. SIEVING	53
3.2.3. MEASUREMENTS	58
3.2.4. HELIUM-PYCNOMETER	60
3.2.5. ULTRASONIC MEASUREMENTS	60
3.2.6. CERCHAR ABRASIVITY INDEX (CAI)	62
3.2.7. CONDUCTIVITY MEASUREMENT	64
3.2.8. BRAZILIAN TEST	64
3.2.9. TRIAXIAL TEST	65
3.2.10. POINT-LOAD TEST	70
4. DISCUSSION	72
4.1. GEOPHYSICAL INTERPRETATION	72
4.1.1. ERT	72
4.1.2. SEISMIC	73
4.2. DEFORMATION INTERPRETATION	74
4.3. SAMPLE INTERPRETATION	76
4.3.1. WATER CONTENT	76
4.3.2. SIEVING	77
4.3.3. POROSITY	78
4.3.4. ULTRASONIC VELOCITY	78
4.3.5. CAI	78
4.3.6. BRAZILIAN TEST	79
4.3.7. TRIAXIAL TEST	79
4.3.8. POINT LOAD TEST	80
4.4. COMPARISON WITH SCHÜNEMANN (2023)	80
4.5. CORRELATION AND OUTLOOK	82
5. CONCLUSION	84

6. LITERATURE	85
7. APPENDIX.....	86
7.1. APPENDIX A: SAMPLES	87
7.2. APPENDIX B: ERT EVALUATION.....	105
7.3. APPENDIX C: STEEL ARCHES	112
7.4. APPENDIX D: DEFORMATION RAW DATA.....	122
7.5. APPENDIX E: 3D ERT TOMOGRAPHY.....	126
7.6. APPENDIX F: CAI RAW DATA	129
7.7. APPENDIX G: SIEVING RAW DATA.....	138

1. Introduction

1.1. Project introduction

In times of global warming all areas of science are required to research solutions to counteract this development. The field of sustainable energy generation has made great progress since the beginning of the millennium but has not been able to achieve a breakthrough in the issue of energy storage.

Major problems are rarely solved by a single solution. Rather, it is the collective effort of science and society that leads to long-term answers. This work aims to join these efforts.

Storing energy using compressed air is not a revolutionary idea, but the approach of doing so in underground cavities can certainly be seen as such. This has significant advantages when it comes to space requirements, safety and the associated public acceptance. In addition, there are already many underground cavities from mining, but also decommissioned infrastructure projects, which are waiting for further use.

The area investigated in this work is located in the heart of the Styrian Erzberg, in an underground mining area that has been unused for around 70 years and therefore represents a very practical example, particularly for the European region. The aim of this work is to determine the geotechnical parameters for the planning and construction of a compressed air storage in a section of the Presserstollen. Geophysical surveys, laboratory tests and the observation of the visible deformation are used for this purpose.

1.2. Geological background

From a geological point of view, the Erzberg is located in the Tyrolean-Noric nappe of the graywacke zone. This zone consists mainly of Palaeozoic phyllitic slabs, porphyroids, marbles and quartzites. It belongs to the Eastern Alpine nappe system. The rocks originate from Silurian to Devonian (Palaeozoic) and are overlain by Mesozoic/Triassic limestones. In the open pit mining acidic metavolcanites (porphyroids (Caradoc)) are exposed.

Below lies the psammitic-metapellitic sequence of the Gerichtsgraben-Formation (Melcher et al., 2022). The porphyroid is followed by the ironore-bearing rocks of the Sauberger limestones,

which are split by the so called *Zwischenschiefer*. Overthrusting during the Variscan orogeny along the *Zwischenschiefer* led to the formation of a hanging and a footwall slab (Figure 1).

Upper Carboniferous to Lower Triassic metasediments (*Werfener Schichten* and *Präbichl Formation*) follow in the hanging wall (Melcher et al., 2022). In the *Präbichl Formation*, these consist of breccias and conglomerates, some of which are mineralized, followed by the purple *Werfen shales* (Melcher et al., 2022).

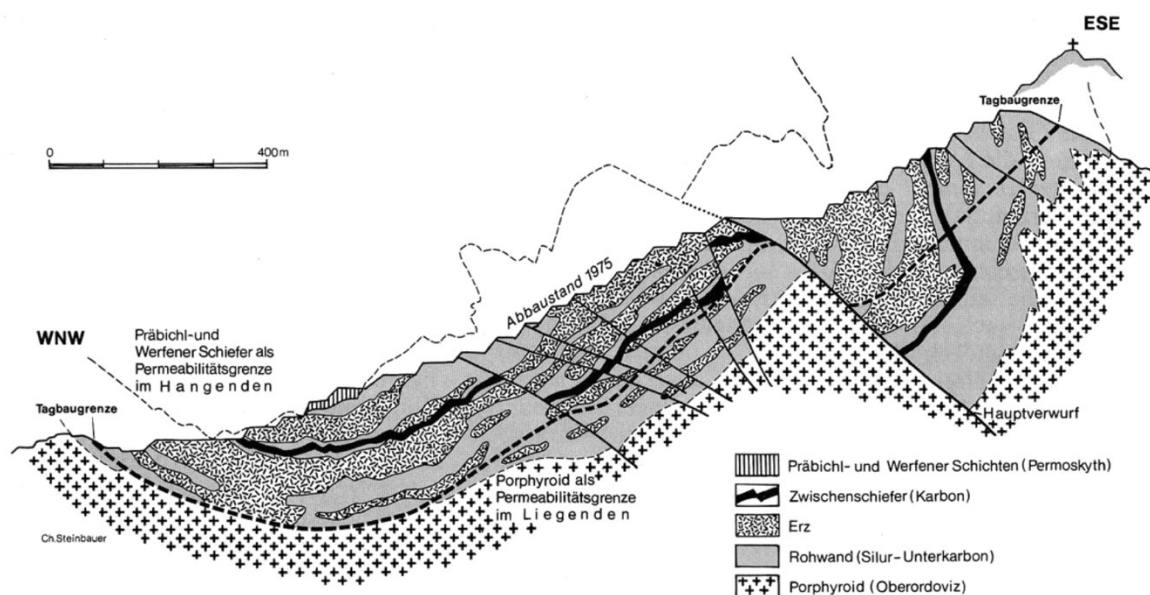


Figure 1: Vertical section through the Erzberg as it was mined by 1975. The main fault along the *Zwischenschiefer* is clearly visible (Holzer and Stumpfl, 1980).

1.3. Presserstollen

1.3.1. History

In 1917 a large compressor plant was put into operation on the southern side of the Dreikönig level. This and the plants on the levels Wismath, Johann and Oswaldi created a compressed air system on the mountain with which the hammer drills could be operated. Out of the buildings constructed only the compressor building has survived to this day. The following section of the 1918 plan illustrates the existing structures. It also indicates the absence of tunnels during that period (Figure 2) (Salzer, 2023).

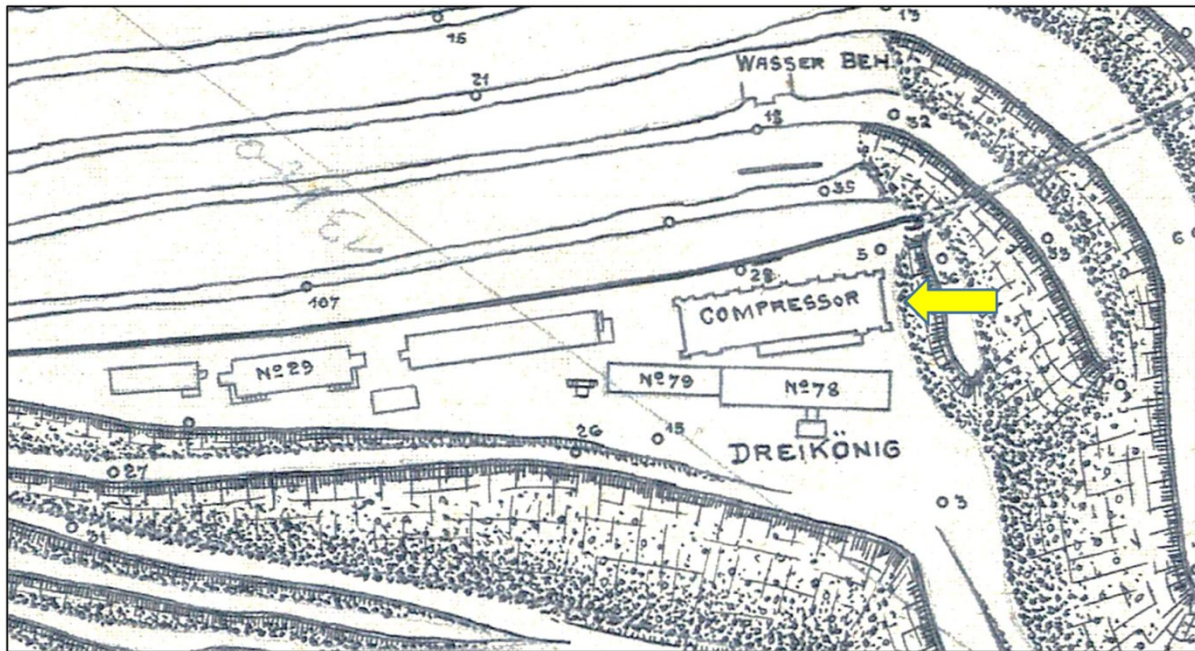


Figure 2: Section of the Dreikönig-level map from 1918 (Salzer, 2023).

The construction of a north-south connecting line (“Nord – Süd Förderstrecke”) began in 1923. This route was intended to connect the tunnels in the north on the Dreikönig level with the Erzberg loading area, eliminating the necessity to drive across the open pit.

This route was built from both sides, but construction was stopped on August 15th, 1924. The approximately 200 m long tunnel with a crosscut remained unused, and because it emerged out the Erzberg near the compressor building, it was given the name "Presserstollen".

Nothing changed till 1941, when construction began on what became known as the "Nord - Süd Förderstrecke", starting at the Renataflügel in the middle of the mountain, expanding from the existing mine structure. In 1942 the connection was established with the Kerpelyflügel and in 1943 with the Presserstollen, which had to be expanded for the larger Krupp minecarts with a capacity of 6.5 m³ at the same time.

In 1943 a skip shaft was planned next to the new mine VII on the Pauli level to transport the ore to the Dreikönig level and further to the Erzberg loading area. Contrary to the custom of using a drop shaft downwards, a skip shaft was planned here to take the already classed ores gently to the Dreikönig level. Based on an auxiliary route under construction, a haulage route to this shaft was started in 1944, but construction was halted on April 5th, 1945 due to the end of WWII.

Among the projects that were pushed ahead after the war was the completion of the "Nord - Süd Förderstrecke". Work was also carried out on the access line to the skip shaft at the Dreikönig level, and after the shaft construction was abandoned the only work on the completion of the section was carried out by students. The tunnel was completed in September 1953. The construction had the sole purpose of training the factory students under real conditions and was therefore never put into operation (Salzer, 2023).

It should be noted that the data used in this chapter was provided by the VA Erzberg (voestalpine) archives, but only very few notes were made, especially in the 1940s and 1950s. Therefore not all the information can be regarded as reliable.

1.3.2. Site description

The area examined in this study is a side arm of the Presserstollen with a dead end (Figure 3, Figure 4). The focus of the work lies within the last 55 m in particular, also known as the steel arch section.

While the Presserstollen crosses the Erzberg from south to north, a tunnel branches off to the east roughly in the middle. With a radius of approx. 50 m, a 90-degree bend leads to a straight section that is 120 m long, has a diameter of around five meter and is oriented towards the SSE. It rises by 0.3 - 0.5 % and ends with an open face.

From the main tunnel to the steel arch section, which is the focus of this work, there is an approximately eight meter long section with steel arch support. The rest is lined with solid masonry in a horseshoe shaped tunnel. Immediately prior to the steel arch section, there is a junction to a collapsed shaft and an associated enlarged cross-section. In the areas that are covered with masonry there is no clearly visible damage. Rails with wooden sleepers have been placed on the invert, most of them have been removed. The resulting deep bumps are still present in the invert, together with remaining debris.

The steel arch section consists of over 100 steel arches with wooden lining, that are deformed and partially broken. The invert is rather bumpy, but the traces of any rails that may have been laid are only visible in indications. The rock material appears loose and grayish. About 30 m into the steel arch area there is yellow fill material on the left side, which has been deposited over several meters. After about 50 m the cross-section narrows to about four meters and there is standing water present in the last few meters before the invert.



Figure 3: Image showing the starting point of the steel arch section up to the tunnel face. The 101 steel arches give the tunnel its name. In the foreground are the measurement boxes of the 3D ERT visible. A measuring tape can be seen along the profile and the geophones on the left side of it.

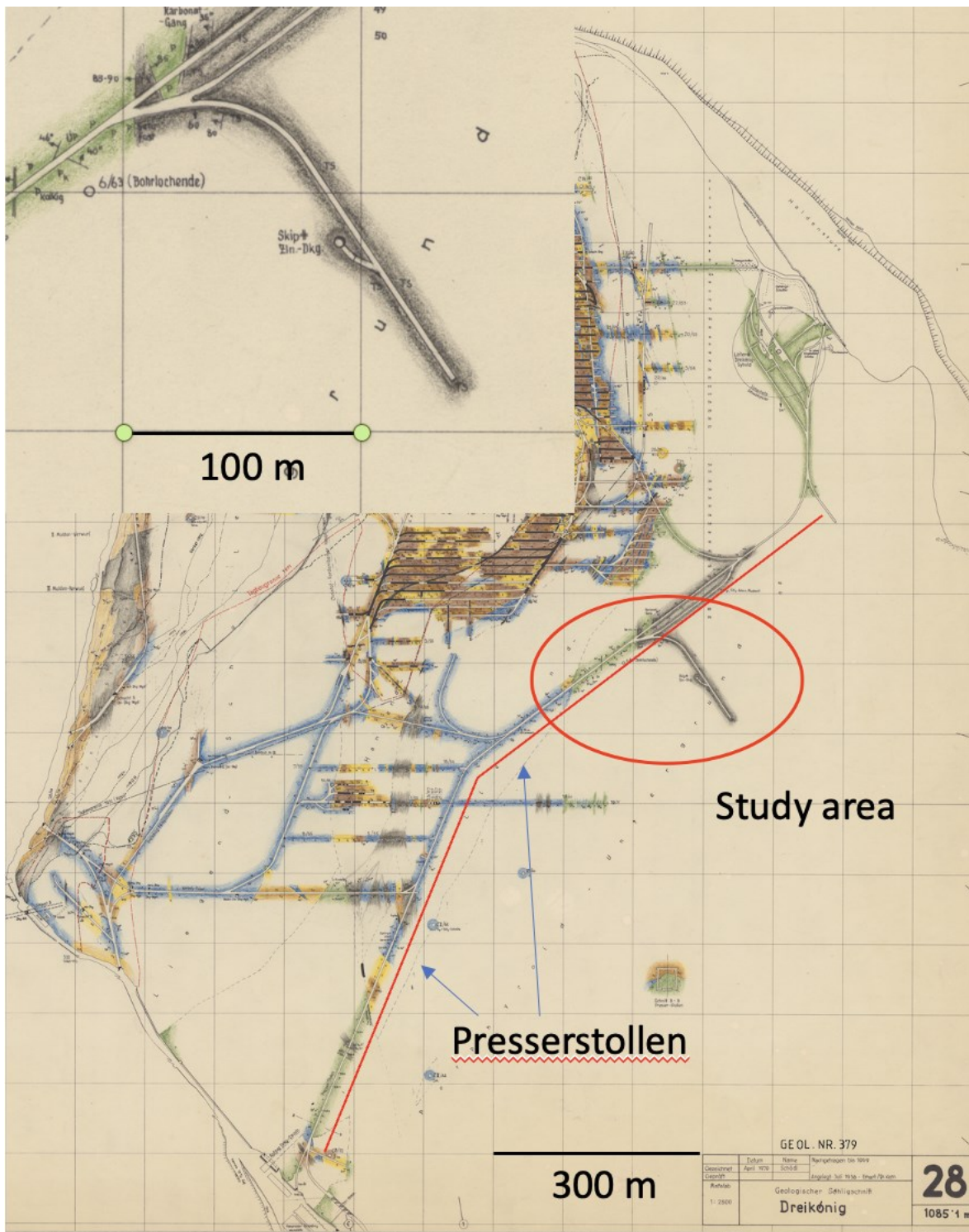


Figure 4: Map of the Dreikönig level from 1975. The Presserstollen can be traced from south to north. The study area is indicated by a red oval. It is shown in more detail on the top left. After Erhart et al., 1970.

2. Methods

2.1. Introduction

Various methods were used to answer the research questions. They are explained in detail in the following chapter and are divided into the methods that were used directly in the field and the methods that were carried out later in the laboratory.

Sampling, seismic tomography, ERT, geodetic surveying and the evaluation of deformation were carried out in the field.

The loose material samples were dried, weighed and sieved in the laboratory. Drill cores were extracted from the hard rock samples, then polished and measured. The seismic velocity, conductivity, porosity and abrasivity were then determined before the samples were destroyed by a triaxial test, a point-load test or a Brazilian test.

2.2. Field methods

2.2.1. Sampling

When taking samples, a grid of samples should be created to take statistically representative samples for the entire area of interest. However, this was not possible due to the difficult conditions in the tunnel. Only the invert, which has been exposed to weathering for at least 60 years, could be sampled. The other areas of the tunnel could not be sampled due to the unsafe lining, that should have been removed in the process.

It was necessary to collect drill cores for the planned experiments. However, this was very difficult due to the loose and broken material in the invert. The use of a drilling rig was not possible due to the inability to anchor into the material, so the samples had to be taken as blocks (0), out of which cores were drilled in the laboratory.

Samples were taken at five different locations along the investigated profile (Table 1). Six samples were taken at the surface and three at a depth of around 30 cm, which corresponds to the tunnel water level.

In total eight samples of loose material and six solid blocks were collected.

Table 1: Sample location, name and corresponding position relative to the tunnel face.

sample location	sample name	distance from the tunnel face [m]
p1	1o	5.7
p2	2b, 2o, 2t	16.5
p3	3t	26.1
p4	4o, 4t	32.0
p5	5o, 5t (solid)	42.9



Figure 5: The hole in the foreground is sample location 5 (p5) where the solid samples were collected. The yellow measuring tape can be seen on the right-hand side of the image. The yellow devices set up along the profile are geophones. The metal spikes together with a measuring box on top are set up for the 2D ERT measurement.

2.2.2. Geodetic survey

The geodetic survey enables the precise measurement of spatial points in a coordinate system. The method is used to precisely locate the geophones and thus correct the results of the seismic survey. The electrodes for ERT, the sampling locations and the measuring tape were also measured as part of this process.

The survey was carried out with a Trimble S5 total station (Figure 6). At the beginning of the profile the station was set up in front of the steel arch section on a tripod and calibrated by using two fixed bireflex targets. This enables to correlate the results from different measurement days with slightly different tripod positions. The results can also be integrated into a global system at a later date.

The measurement of the spatial points (geophones, electrodes, measuring tape, sample locations) was conducted with the help of a mobile control unit and a prism mounted at a height of 1.8 meters.



Figure 6: The equipment used during the survey: Bottom left: the "Trimble S5" surveying device in its case. Top left: the prism used for the survey, mounted on a pole at a height of 1.8 meters. Top right: the "Trimble S5" station set up with the surveying device on a tripod. Bottom right: the portable device for sending commands to the station and storing the data.

2.2.3. 2D seismic

The objective of this method is to determine velocities within ground layers by capturing the seismic signal (first break) received by geophones arranged in an array or line. These seismic signals are induced to the subsurface by a source. This study uses a sledgehammer for this purpose.

The velocity of the spreading wave varies depending on ground conditions. Geophones are used to record the seismic vibrations. They consist of a magnet that is suspended within an electric coil. Seismic vibrations cause the geophone to oscillate vertically, resulting in movement of the magnet within the coil. A signal is generated and subsequently recorded. The voltage can be positive or negative depending on the velocity and direction of the magnet.

2.2.3.1. Seismic setup

The geophones were set up in the middle of the tunnel (Figure 5). SummitX software was used to process the data from the data collector. The 123 geophones (Figure 7, left) were positioned on a straight line with a spacing of 50 cm each and connected to a data cable by an analog to digital converter (Figure 8). The initial geophone was designated as 1001 and positioned furthest from the face. The geophones have been inserted into the ground using a metal stick to create a predrilled hole. Good contact with the ground is crucial for obtaining accurate measurements and producing optimal results. A sledgehammer with a piezoelectric trigger was used as source of the seismic signal. It was connected to the seismic line. To ensure a good contact with the ground, a metal plate was used as a surface on which the hammer was struck (Figure 7, right; Figure 7, left).



Figure 7: Left: Geophone. Right: Hammer and metal plate used for the seismic data collection.



Figure 8: Left: The seismic experiment being carried out. Top right: The data collector. Bottom left: The cable drums with the data cable used.

2.2.3.2. Seismic processing

The raw data was linked with the results of the survey to obtain exact spatial data. Further analysis was carried out using the software RadExPro from Schlumberger. After checking the data quality, faulty lines were excluded, and high peaks were smoothed to enable the software to generate a tomogram. The final parameters used are defined in the results (Figure 43).

2.2.4. Electric resistivity tomography (ERT)

ERT is based on the measurement of electrical conductivity of the rock mass. As most rocks are only insignificantly conductive, mainly the water in the pore space and along fractures influences the results. Lithological differences as well as deformed or loosened areas can be identified by this method.

A resistivity measurement requires the use of four electrodes, with two electrodes (A and B) used to induce an electric current and two electrodes (M and N) used to measure the voltage. Increasing the distance between electrodes A and B will allow to measure deeper layers. Three different arrangements for the electrodes were used in this study (Figure 9): Wenner- α , pole-pole and pole-dipole.

Wenner- α is the default arrangement. In this setup all electrodes are placed equidistantly, and the voltage is induced at the outer electrodes and measured at the inner electrodes. The results are very reliable and usually very smooth in tomography.

The pole-pole measurement involves the use of two distant electrodes. There is one electrode for current, which is commonly designated as B, and one electrode for voltage, which is commonly designated as N. The two remote electrodes are positioned at greater distances from the array. This allows for a greater depth of penetration. The positioning of the remote electrodes is determined by the distance between the electrodes in the array and roughly 10 to 15 times larger.

The "pole" in pole-dipole refers to a single transmitting electrode, while the "dipole" consists of a pair of electrodes with opposite charges. The electrodes of a dipole are positioned in such close proximity that the resulting electric field seems as if it originates from a single electrode, rather than two distinct electric poles.

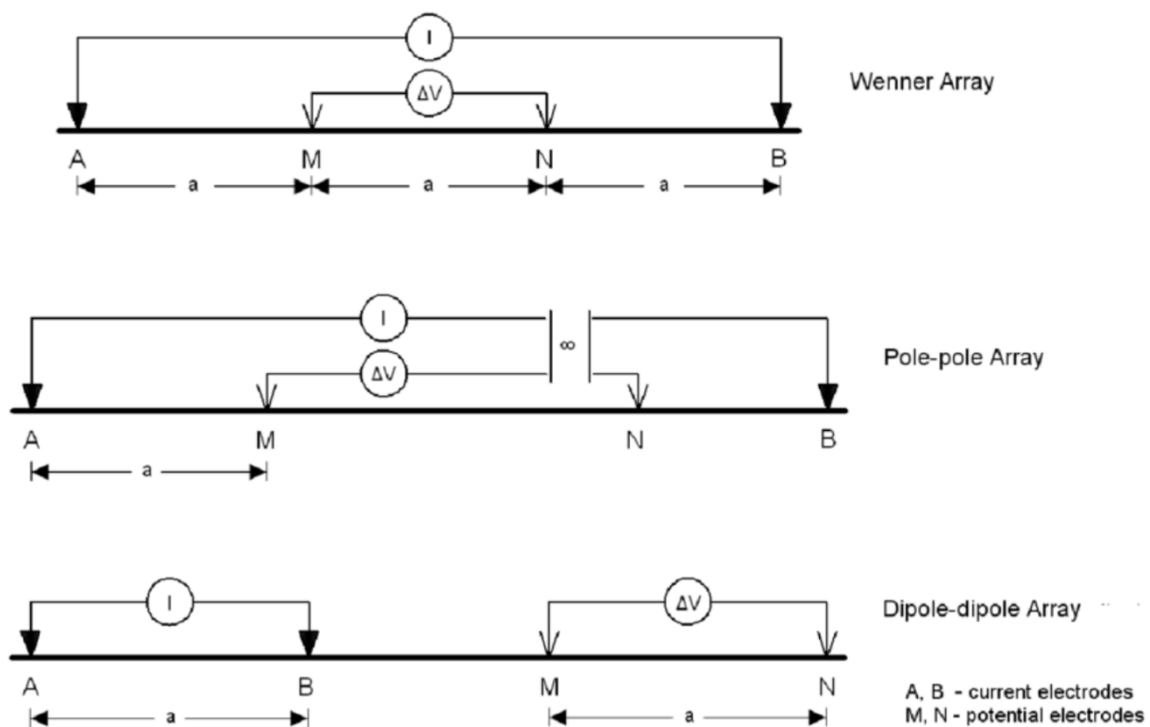


Figure 9: Wenner- α , pole-pole and dipole-dipole setup with the inducing electrodes A, B and the measuring electrodes M, N. The distances are given by "a", whereby it should be noted that these are only relative distances within a setup. Šumanovac and Alavanja (2007).

2.2.4.1. 3D setup

The array in this study had a size of 2.5 x 2.0 meters and consisted of eleven electrodes in the x-direction and nine electrodes in the y-direction (Figure 11, right). The x-axis of the coordinate system aligns with the direction of the tunnel, while the y-axis was perpendicular to it, extending from the right wall to the left wall of the tunnel. The distance between the electrodes was 0.25 meters in both the x-axis and y-axis. The electrodes were connected using a total of 5 cables, each containing 20 boxes for a total of 20 electrodes. Each box was assigned a unique IP address. The boxes were linked to an electrode, beginning with the first electrode positioned at point (0/0) (Figure 10).

A signal amplifier was used since the cable was too long and the quality of the signal would attenuate. The resistivity measurements were conducted using a 4-point light 10W device by Lippmann, which was connected to the computer (Figure 11, left). Additionally, the setup was connected to the ground using an extra electrode prior to conducting the test.

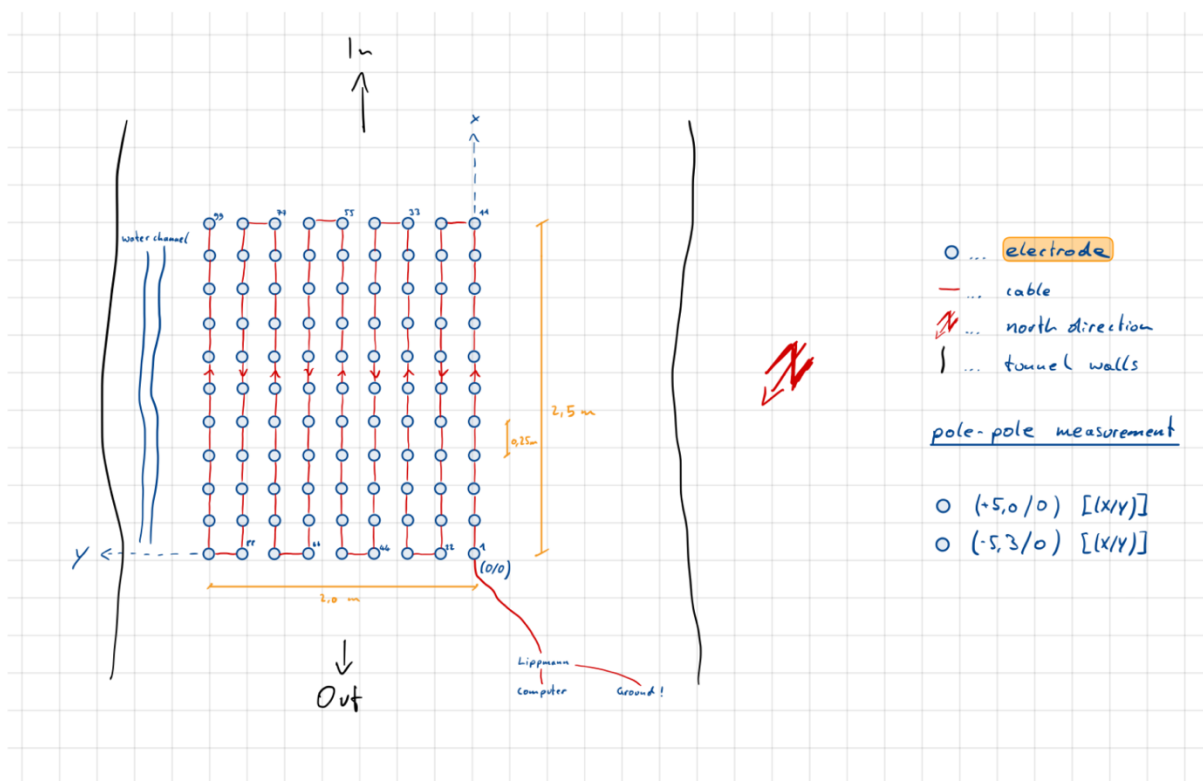


Figure 10: Sketch of the ERT 3D array including the 99 electrodes and their connections. The direction "In" refers to the direction of the steel arch section and the tunnel face. Zabl (2023).



Figure 11: Left: Setup for collecting ERT data: Laptop for receiving, analyzing and storing the data. Orange "4point" device for transmitting the electrical signals and measuring them. Right: 3D - ERT array. Steel sticks, hammered into the ground with a measuring box on top, are set up in a grid.

2.2.4.2. 2D setup

The setup of the 2D ERT began directly at the face. Electrodes were put into the ground, each separated 60 cm from this first electrode. A total of 99 electrodes extended out of the steel arch area into the masonry area. The connections were made in the same way as in the 3D ERT. The remote electrode was placed 62 m away from the setup.

2.2.5. Deformation observation

Finding deformation indicators can be a difficult task because for many structures, natural or anthropogenic, only the "as-is" state can be observed. Information about the original state and the development of the deformation is usually missing. When building a tunnel, a state-of-the-art monitoring system should have been installed to make the deformations traceable. Therefore, two basic assumptions were made for this work, which can be regarded as highly probable, but could nevertheless be incorrect.

Firstly, it was assumed that the lining, in particular the steel arches, were symmetrical and undamaged at the time of installation. Secondly, it was assumed that the deformations have subsided or reduced to a negligible level. To assess the deformation, the visible deformation on the crown and both sides was classified from 1 to 5, with 1 indicating no damage or deformation and 5 indicating partial failure of the support. For better traceability of the results and possible comparison with future studies, pictures of the arches were taken and numbered (Figure 12).

Steel arch classification:

- 1: The arch is in very good condition and shows no sign of deformation. Age-related corrosion of the steel is not considered.
- 2: Slight deformation of the arch.
- 3: Clearly visible deformation of the arch.
- 4: The arch is severely deformed.
- 5: The arch is broken and/or shows cracks.



Figure 12: Numbered arches 70-80 in the study area.

2.3. Laboratory Methods

2.3.1. Sample processing

2.3.1.1. Loose samples

2.3.1.1.1. Description

Table 2: Description of the collected loose samples.

sample	distance from face [m]	depth	grain size	color	wettness
1o	5.7	surface	coarse	gray	slightly wet
2o	16.5	surface	fine	gray	slightly wet
2b	16.5	surface	coarse	ochre	slightly wet
2t	16.5	30 cm deep	fine	gray	water-saturated
3t	26.1	30 cm deep	fine	grayish with brown	water-saturated
4o	32.0	surface	coarse	ochre with gray	slightly wet
4t	32.0	30 cm deep	coarse	gray	water-saturated
5o	42.9	surface	very coarse	ochre with gray	slightly wet

2.3.1.1.2. Preparation for sieving

The loose material samples were put into containers of known weight in the laboratory and weighed in wet state. After that they were dried in an oven at 105 degrees Celsius to constant mass. The samples were then weighed in a dry state.

2.3.1.2. Solid samples

2.3.1.2.1. Description

Every solid sample was taken from sample point 5, where a 40 cm deep hole was dug using a pick axe. The large and visually most stable seven samples were taken (Figure 13).

They are grayish, finely crystalline and have some quartz veins crossing them. A clear schistosity can be seen.



Figure 13: The six solid samples that were stable enough to drill cores from.

2.3.1.2.2. Preparation of solid samples

The drill cores were obtained with a HILTI DD-759HY drill rig (Figure 14, left). A drill bit with an inner diameter of 29 mm was used for five samples and a drill bit with an inner diameter of 50 mm was used for the other two samples. The samples were clamped between wooden plates in a screw clamp and braced to prevent movement. When aligning the samples, care was taken to drill the holes at a right angle to the clearly visible schistosity. The cores were extracted by manually lowering the drill bit with water for cooling purposes. A total of 20 cores with a small diameter and three with a large diameter were obtained (Figure 15, Figure 16). Because there was already some loss of material during the drilling of the samples, a very gentle method of further processing was chosen. To polish the top and bottom of the samples a manual grinding wheel was used (Figure 14, right), allowing it to be operated at low pressure. This prevented further loss of sample material, although it was not possible to achieve perfect plane parallelism of the ends.



Figure 14: Left: HILTI DD-759HY drilling rig together with a drill bit with an inner diameter of 29 mm. The sample is held in place with a screw clamp and wedged with wood. Right: Spinning, abrasive plate used to polish the samples.



Figure 15: The drill cores obtained from samples PS I, PS II and PS III.

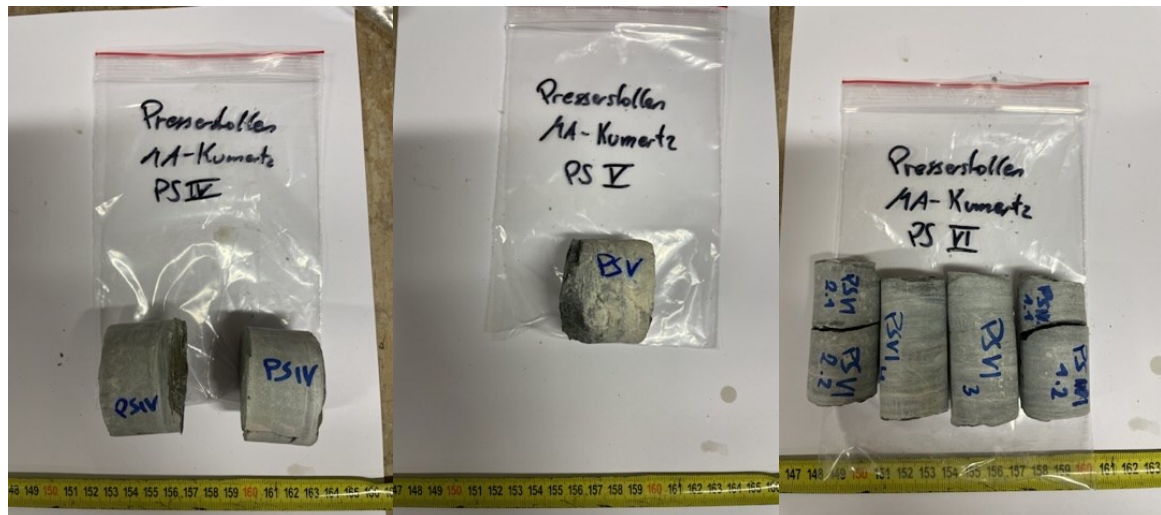


Figure 16: The drill cores obtained from samples PS IV, PS V and PS VI.

2.3.1.2.3. Measuring

Once the samples had been polished and their dimensions had not changed, they were measured and weighed. The height and diameter were measured using a digital caliper slide (Figure 17, left). Both parameters were each measured three times and the results were averaged to obtain reliable data. Weighing was carried out using a Mettler PJ3000 precision scale (Figure 17, right).



Figure 17: Left: Digital caliper slide to measure the drill core's dimensions. Right: Mettler PJ3000 scale for weighing the samples.

2.3.1.2.4. Saturation

In order to determine the porosity and conductivity of the samples, it is necessary to saturate them with water. For this purpose, they were placed in a desiccator (Figure 18, right), which was sealed airtight. A vacuum pump was then used to create as good a vacuum as possible. After around 20 minutes water was added via a water supply at the top without adding air, so the pore air can escape from the sample and the entire open pore space can be filled with water. Once the samples were put under water a vacuum was created again. The samples were left in this state for one week before further tests were executed. The water used was tap water, as the measurement corresponds to the conductivity in the area under investigation at ZaB.



Figure 18: The devices used to saturate the samples in water: On the left, a conductivity meter from HANNA. In the center, a steel dish with the samples in a desiccator. On the right, the addition of water to the desiccator being under vacuum.

2.3.1.2.5. Porosity (Archimedes)

The saturated samples were then weighed wet and with buoyancy under water (Figure 19). Now it was possible to calculate the porosity of the samples using the following formula:

$$\phi = \frac{m_{sat,up} - m_d}{m_{sat,up} - m_{sat}} * 100 [\%]$$

ϕ ... Porosity [%]

m_d ... mass dry [g]

m_{sat} ... mass saturated [g]

$m_{sat, up}$... mass saturated with uplift [g]

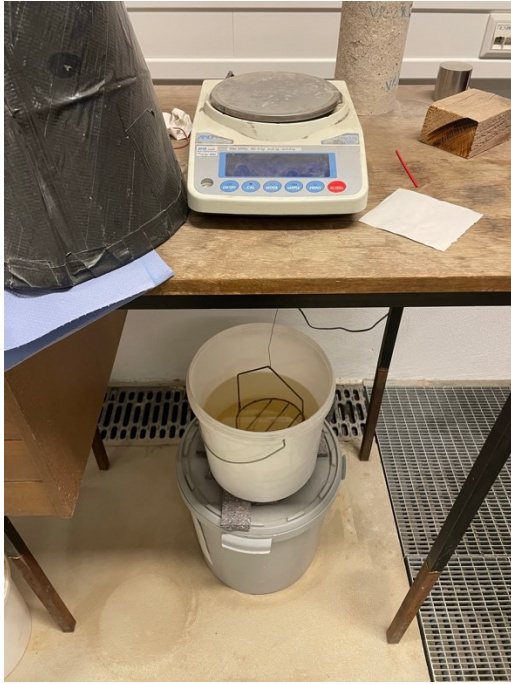


Figure 19: Experimental setup to weigh the samples under water. The scale on top is connected by wire to the basket under the table, which is filled with water ($\delta = 1\text{g/cm}^3$).

2.3.2. Sieving

Sieving loose material is a very good way of obtaining information. In this work however, the task is not to determine the load-bearing capacity or susceptibility to subsidence, which would be a common question above ground, but rather the question of how weathered the material is and how easily it could be removed. To answer these questions, a sieve tower was set up with the following sieves: 500 μm , 1 mm, 2 mm, 4 mm, 8 mm, 16 mm, 31.5 mm.

The sample material was dry before sieving. The individual samples were divided to improve the accuracy of the sieving and to avoid overloading individual sieves. Between the samples, the entire sieve tower was cleaned, in particular to remove the stuck grains. The individual fractions were then weighed, packed and marked.

The sieves were placed on a Fritsch brand electric vibrating plate (Figure 20, left), which was run with an amplitude of 0.5 mm. The sample material was fed in before the device was started. During operation the grains were evenly distributed on the sieve with a brush to achieve better fractionation. This process was carried out for all sieves, starting with the top one, for achieving the best results possible. The grain sizes were then weighed and analyzed in tabular form.



Figure 20: The equipment used to sieve the samples. On the left, the sieve tower on the electric vibrating table with the sieve sequence from bottom to top: < 500 μm , 500 μm , 1 mm, 2 mm, 4 mm, 8 mm, 16 mm, 31.5 mm. The brushes for cleaning the sieves between the individual samples can be seen on the right-hand side.

For the calculation of the Coefficient of Uniformity (U) and the Coefficient of Curvature (C_C), the values for D_{10} , D_{30} and D_{60} were determined. The results of the sieving were interpolated if necessary. The coefficients were calculated using the following formulas:

$$U = \frac{D_{60}}{D_{10}}$$

$$C_C = \frac{D_{30}^2}{D_{10} * D_{60}}$$

U ... Coefficient of Uniformity

C_C ... Coefficient of Curvature

D_{10} ... Grain size with 10 % of the sample passing the sieve

D_{30} ... Grain size with 30 % of the sample passing the sieve

D_{60} ... Grain size with 60 % of the sample passing the sieve

2.3.3. Helium-Pycnometer

The helium pycnometer can be used to determine the volume of the grains and the grain density in a dry state. As with porosity measurement according to Archimedes' principle, it should be remembered that only the connected pore space is measured.

The measuring principle is based on gas displacement. The measured sample was placed in the measuring chamber of the Ultrapyc 5000 (Figure 21) and sealed. A vacuum was then created, and helium was added at a constant temperature of 20 degree Celsius. The device can calculate the volume from the amount of helium added and the resulting pressure. The previously determined weight was used to calculate the density.



Figure 21: The Ultrapyc 5000 helium pycnometer from Anton Paar used for the measurement.

2.3.4. Ultrasonic velocity

Measurement of the ultrasonic velocity of the p-wave velocity of the samples is particularly interesting in connection with the seismic investigation conducted in the field. In order to collect as much information as possible the samples were measured both dry and saturated.

The signal for the measurement was generated with an ultrasonic generator and had a frequency of 250 kHz. It was received by a Cleverscope oscilloscope (Figure 22).

Before starting the measurement the device was tested with a granite drill core with a known p-wave velocity. The samples were then covered with ultrasonic gel and placed in the device. For the evaluation, the time to the first received signal (= travel time) was measured. The following formula was used to calculate the p-wave velocity:

$$v = \frac{h}{t} \text{ [m/s]}$$

v ... velocity [m/s]

h ... sample height [m]

t ... travel time

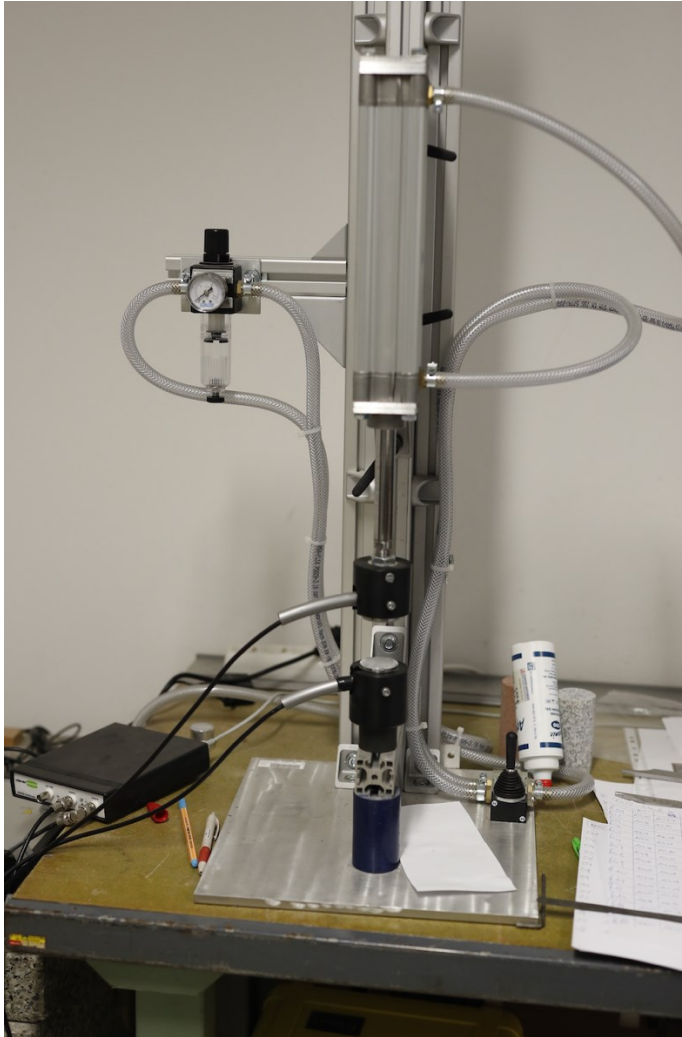


Figure 22: The setup for measuring the p -wave velocity. Signal generation and reception take place in the black box on the left of the picture. The height of the upper piston can be adjusted with compressed air to take into account the different heights of the samples. The upper piston also generates the signal that passes through the sample to the lower piston, where it is received. For better transmission, the sample is smeared with the ultrasound gel visible on the right of the picture. Also on the right-hand side is a granite drill core, which is used to calibrate the device.

2.3.5. Cerchar Abrasivity Index (CAI)

The CAI is used to determine the abrasivity of rocks. This is particularly important in underground excavation, as it provides a reference value for the wear of the excavation tools used.

For this test pieces of the samples PS III and PS VI were cut off with a saw. Since the international standard assumes a rough surface, the value determined in the test must be corrected:

$$CAI_{rough} = CAI_{sawcut} * 1,14$$

2.3.5.1. CAI setup

The test setup according to ISRM 2014 consists of a device in which the sample is clamped and can be moved with a hand crank (Figure 23, left). The thread of the hand crank has a gradient of 1 mm per revolution. A steel tip with an angle of 90 degrees is placed on the sample. A pin guide keeps it in place. It is loaded with a 7 kg weight. The sample is then moved under the steel pin 10 turns of the hand crank, which results in a 10 mm long scratch. This movement should be performed slowly and consistently.

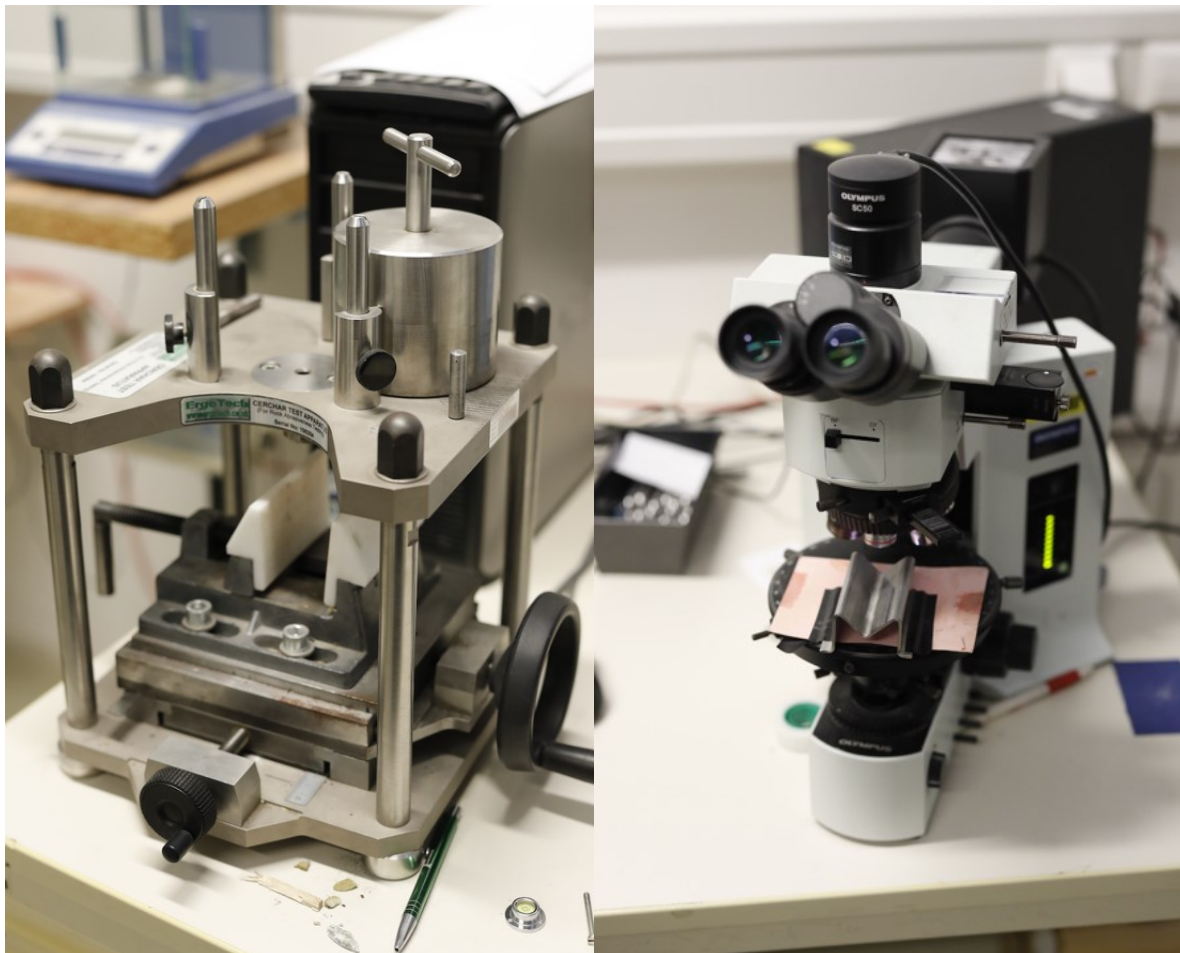


Figure 23: The Cerchar test apparatus can be seen on the left-hand side of the picture. Important elements are the small hole into which the steel pins are lowered for testing and the 7 kg weight with handle, which loads the pin and thus also the sample. The mechanism for clamping and the hand crank for testing can be seen below. The digital microscope "Olympus SC 50", which is used to evaluate the steel tips, can be seen on the right-hand side of the picture. A 5x magnification and manual focusing are used.

2.3.5.2. CAI Processing

The steel tips were analyzed using an Olympus SC 50 digital microscope (Figure 23, right). The aim is to determine how much of the steel tip has been abraded (Figure 24). During the measurement, particular attention must be paid to uniform wear. Tips abraded on one side are not permitted as a result. The tips are measured from four directions in order to achieve a good result.

The CAI is calculated as follows:

$$CAI = d * 10$$

CAI ... Cerchar Abrasion Index

d ... pin wear [mm]

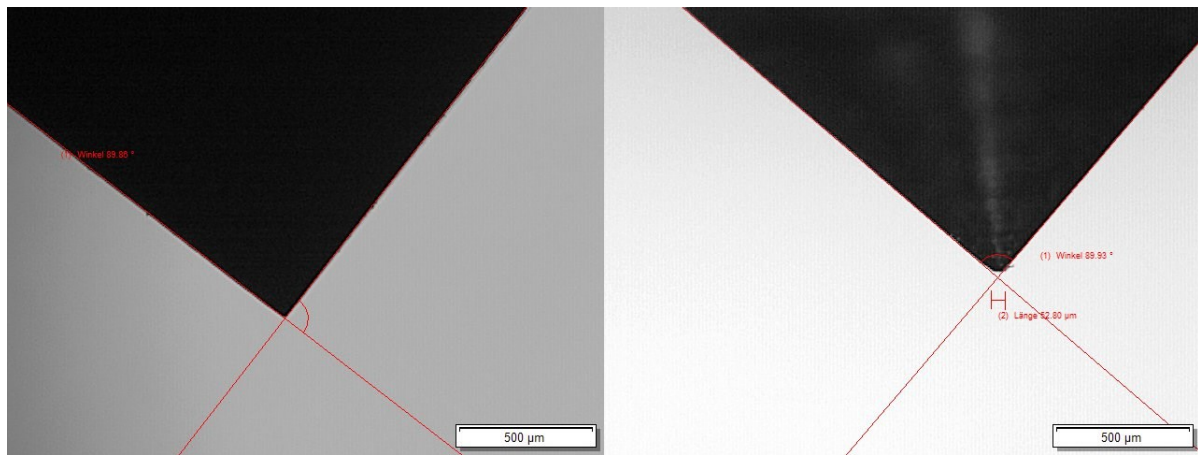


Figure 24: Steel tips under the microscope. On the left a fresh tip and on the right a tip after the experiment with an abraded tip.

2.3.6. Resistivity measurement

The measurement of electrical resistance primarily provides information about the pore spaces of the material under investigation. It can be assumed that the dry material has no conductivity in the measurable range. However, the results of this investigation are very important regarding the ERT carried out in the field. The samples were therefore saturated and the measurements were then carried out in the geophysics laboratory in Leoben.

For this purpose the sample was dried swiftly on the outside and its mantle surface was immediately wrapped in insulating adhesive tape to prevent further drying out during the measurement. It was then clamped between two slightly wet sponges in the test setup (Figure 25). The voltage drop through the sample was measured using a multimeter, thus making it possible to calculate the specific resistance. The test was carried out twice for all samples. An average value was then calculated. The following formulas were used for the calculation:

$$c_{geo} = \frac{\left(\frac{d}{2}\right)^2 * \pi}{l}$$

c_{geo} ... Correction-factor geometry

d ... diameter [m]

l ... length [m]

$$\Omega_{spec} = U * c_{geo} [Vm]$$

Ω_{spec} ... specific resistance [Vm]

U ... voltage [V]

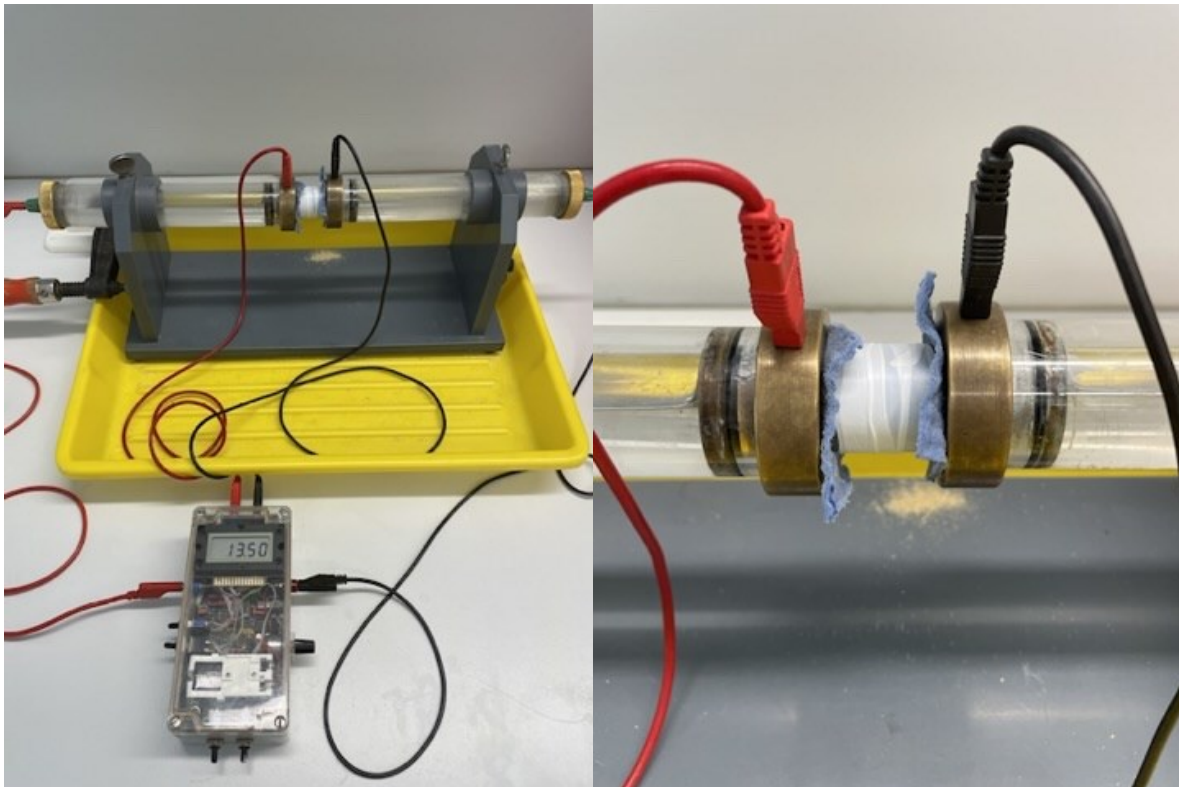


Figure 25: The left-hand side shows the overall structure of the conductivity measurement. In the foreground the measuring device and in the background the mounted sample can be seen. On the right is a close-up with the sample wrapped in insulating adhesive tape.

2.3.7. Point load test

The point load test is a very simple method that can also be used in the field to determine the strength of rocks. The samples used for this do not require any special preparation, although the use of cylinders or cubes is advantageous for better comparability.

A total of 18 point load tests were carried out. Of these, six were a simple test and twelve were part of the special point load test. Thuro (2010) set the following requirements for the cylindrical samples used:

For lying cylinders (Figure 26, a):

$$25 \text{ mm} < d < 100 \text{ mm}$$

$$h > 25 \text{ mm}$$

$$h > \frac{d}{2}$$

$$\frac{d}{h} < 1$$

For standing cylinders (Figure 26, b):

$$25 \text{ mm} < d < 100 \text{ mm}$$

$$d > 25 \text{ mm}$$

$$0,5 < \frac{h}{d} < 1$$

All samples met these criteria.

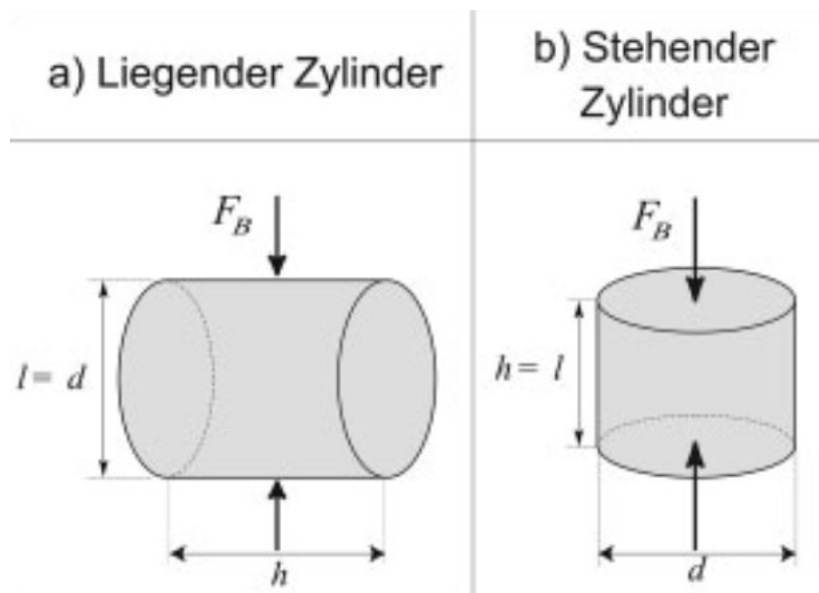


Figure 26: Dimensions according to Thuro (2010) for standing and lying samples.

2.3.7.1. Test

The point load test requires two steel tips with a radius of 5 mm, which lie on an axis and stress the sample, which is clamped between them until it breaks. A device measuring the maximum force is required to read out the result.

A device from WILLE Geotechnik was used for the experiments in this work (Figure 28). It consists of a manual pressure pump that can apply up to 100 kN of force, a pressure gauge and steel tips. Pressure is applied through the lower tip, while the upper tip acts as a fixed counterweight.

In the test, the pressure gauge, which records the maximum pressure, is first reset, then the sample is clamped in a central position with slight pressure. The pressure is then slowly increased until failure. The fracture behavior was observed to determine whether the result was valid. Thuro's (2010) recommendations were used for this (Figure 27).

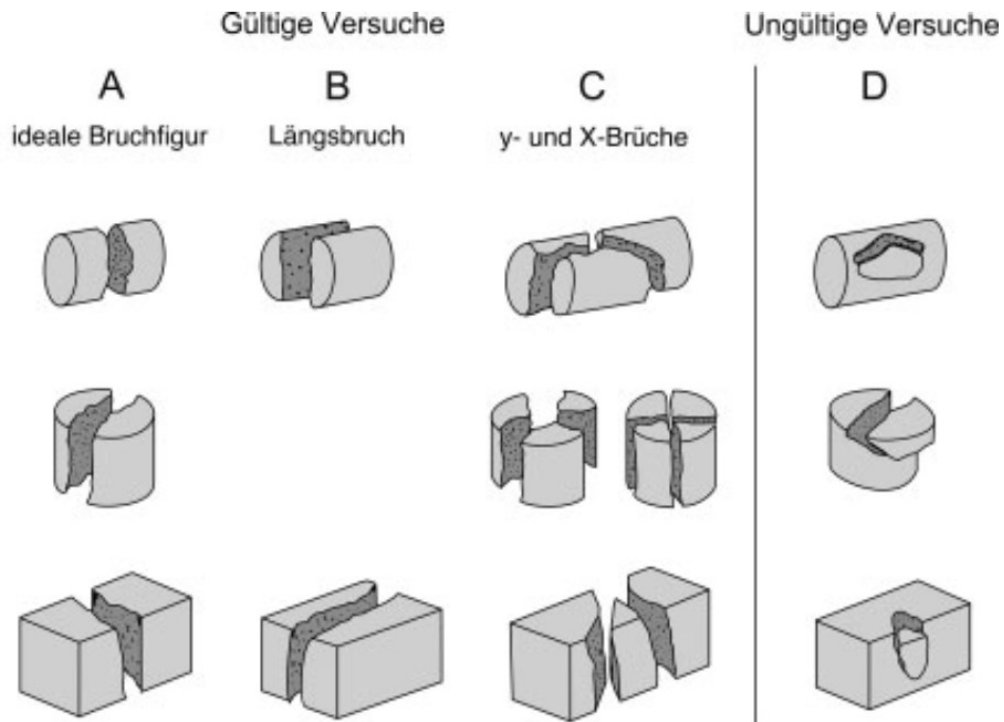


Figure 27: Graphical representation of valid and invalid fracture behavior according to the recommendations of Thuro (2010).

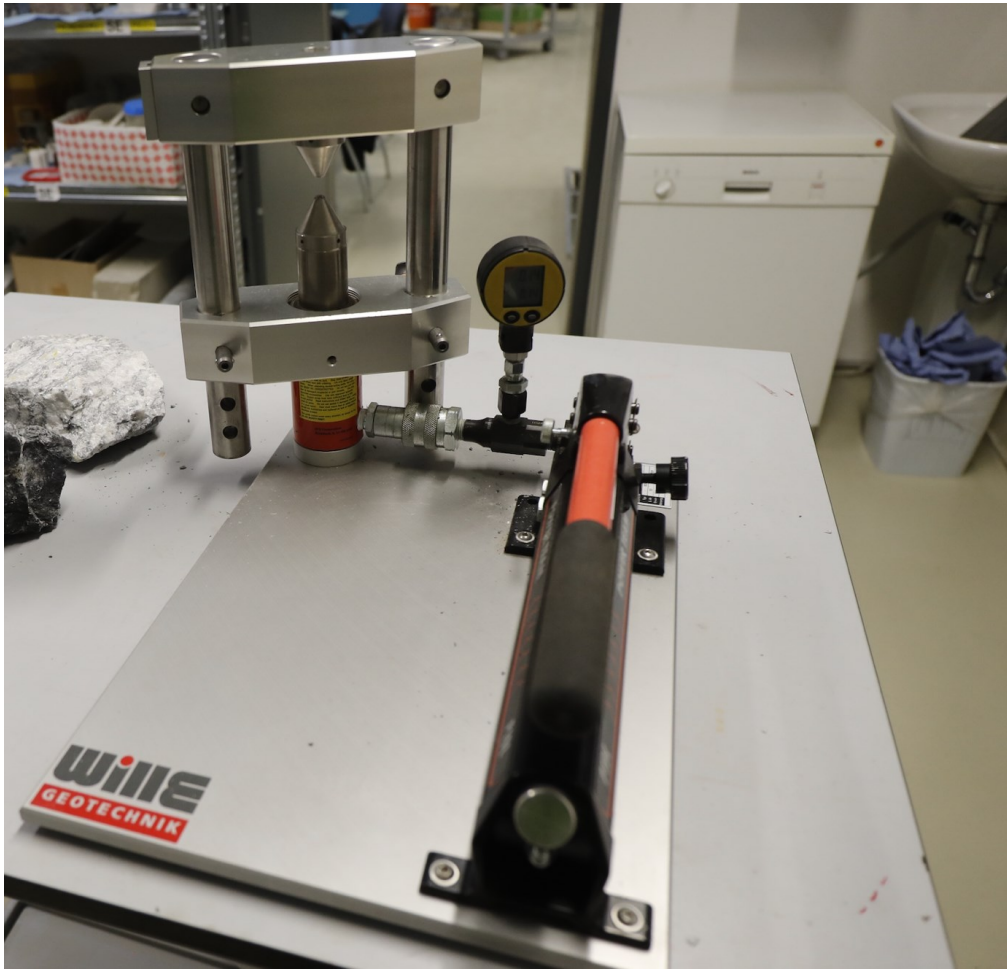


Figure 28: Setup for the point load test. A WILLE Geotechnik device with the manual pump on the right, the pressure gauge and the adjacent cell with the two tips, in between which the sample is inserted.

The results of the maximum force (breaking force) were then used to calculate the point load strength. For this, it is also necessary to calculate the sample surface area. The following formulas were used:

$$A_l = \frac{\pi}{4} * d^2 [mm^2]$$

$$A_s = h * d [mm^2]$$

$$I_s = \frac{F_b}{A} [MPa]$$

$$I_{s(50)} = \left(\frac{A}{2500} \right)^{0,225} * I_s [MPa]$$

A_l ... surface area for lying cylinders [mm^2]

d ... sample diameter [mm]

A_s ... surface area for standing cylinders [mm^2]

h ... sample height [mm]

I_s ... point load strength [MPa]

F_b ... breaking force [N]

$A \dots A_s$ or A_l

$I_{s(50)}$... point load strength with size adjustment [MPa]

2.3.7.2. *Axial point load*

In the simple axial point load test the samples were clamped upright in the test device and stressed to failure (Figure 29).

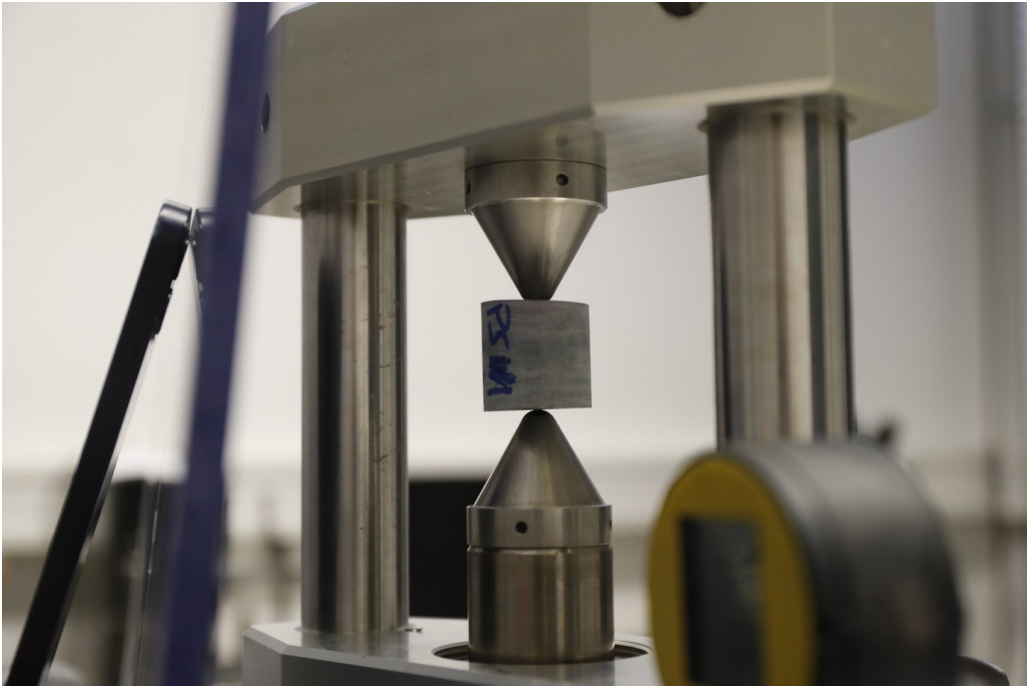


Figure 29: Clamped sample for an axial point load test.

2.3.7.3. *Diametral point load*

In the special diametral point load test the samples were first clamped horizontally and stressed to failure (Figure 30). The two fragments were then clamped upright and broken. It should be noted that the fracture surface was not processed before the test.

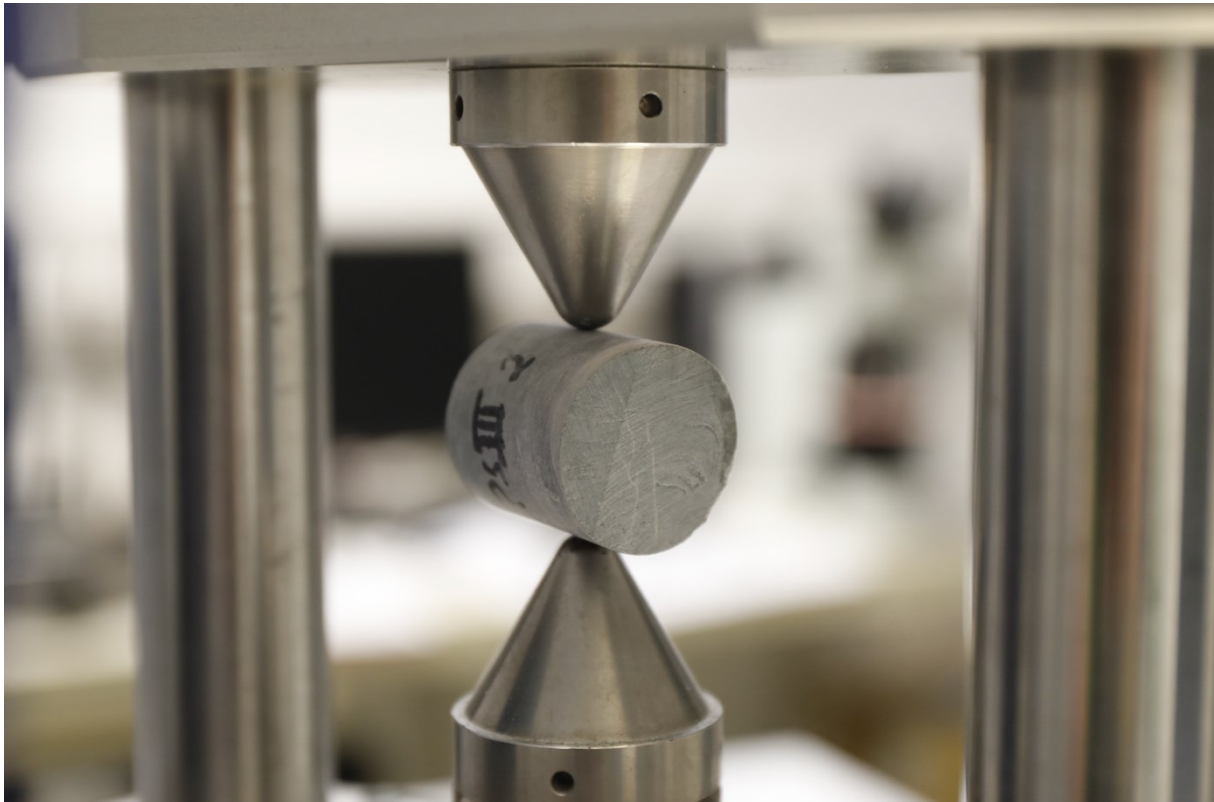


Figure 30: Clamped sample for a diametral point load test.

2.3.8. Brazilian test

The Brazilian test is used to estimate the tensile stress that a rock can withstand. It is much easier to perform than a direct tensile test and is therefore widely used in the field of geotechnics.

A device from WILLE Geotechnik was used for the Brazilian tests in this project. It consists of a manual pressure pump that can apply force of up to 100 kN, a pressure gauge and the sample compartment (Figure 32). A cylindrical sample is clamped in and squeezed at opposite sides of its mantle (Figure 31, left and right). The resulting tensile stress causes the sample to fail (Figure 31, center). The tensile strength can be calculated from the maximum force applied using the following formula.

$$\sigma_{t,sp} = \frac{2 * F_B}{\pi * d * l} [MPa]$$

$\sigma_{t,sp}$... indirect tensile strength

F_B ... breaking Force [kN]

d ... sample diameter [mm]

l ... sample length [mm]

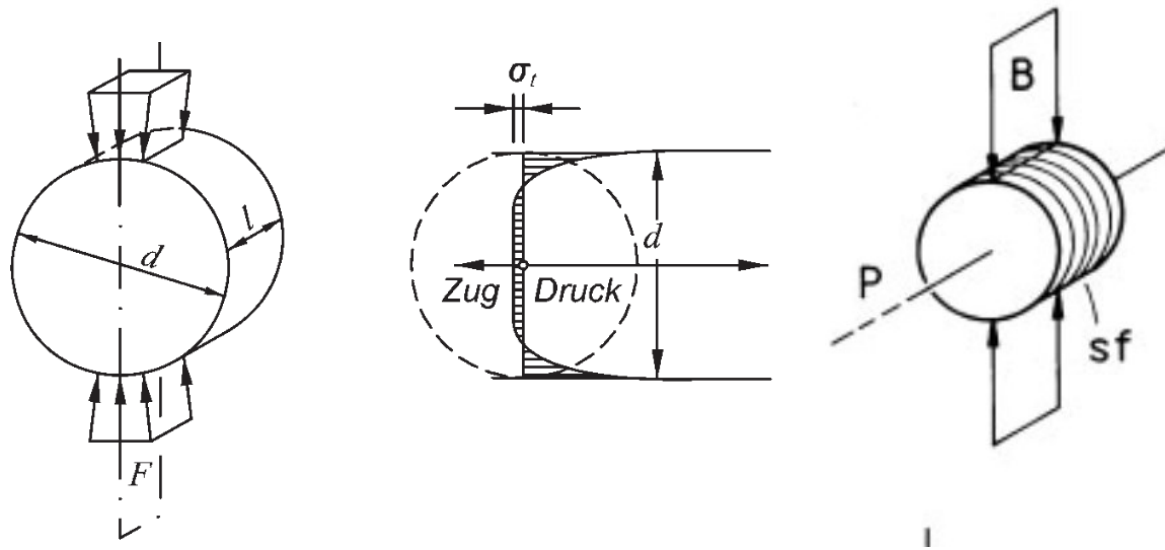


Figure 31: Left: Schematic representation of the Brazilian test with a cylindrical sample stressed at the top and bottom. Center: The stress distribution occurring in the sample during the test. Right: The orientation of the sample and its schistosity as it was placed in the apparatus. Lepique (2008).

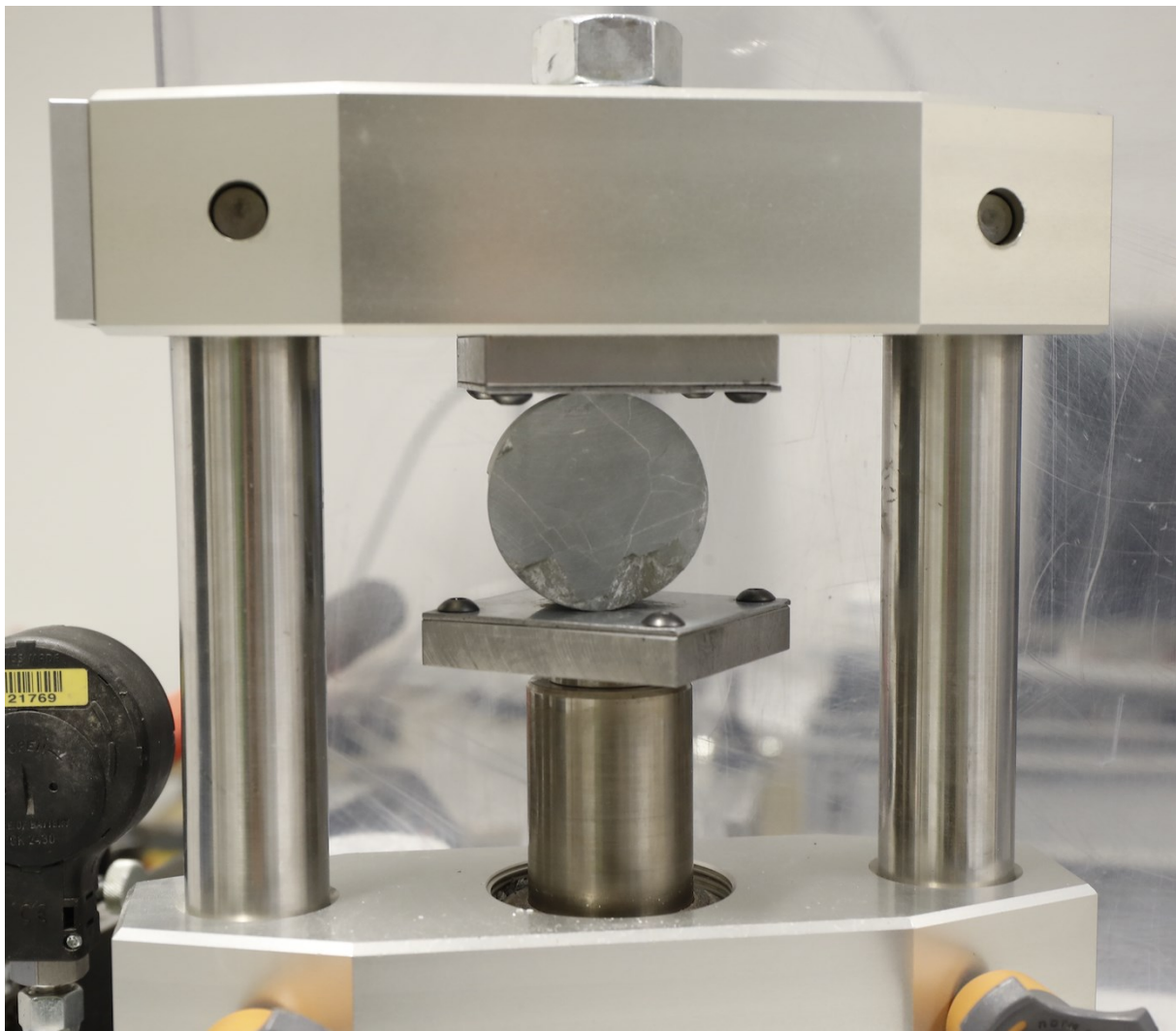


Figure 32: Sample setup for the Brazilian test.

2.3.9. Triaxial test

The triaxial test is used to determine the failure load of rocks that are confined as they occur within a rock mass (in situ) (Figure 33, left) (Rissler, 2023). In contrast to the Uniaxial Compression Strength (UCS), the sample is confined from all sides. In the test setup, a confining pressure is applied to the mantle of the cylindrical sample while it is loaded along the cylinder axis to failure (Figure 33, right).

2.3.9.1. Triaxial test setup

For the test the samples were placed in a cell that can build up a confining pressure via a manual pump. The vertical pressure was generated by an MTS servo-hydraulic rock testing press, which recorded both pressure and vertical deformation, while the circumferential pressure was recorded manually from the manometer (Figure 34).

The confining pressure was increased to 5 MPa, 10 MPa or 15 MPa at the same time as the vertical pressure. From this point onwards, the further pressure development was recorded, but no further confining pressure was actively generated. The values were recorded up to the maximum range of the press, which is 10 mm.

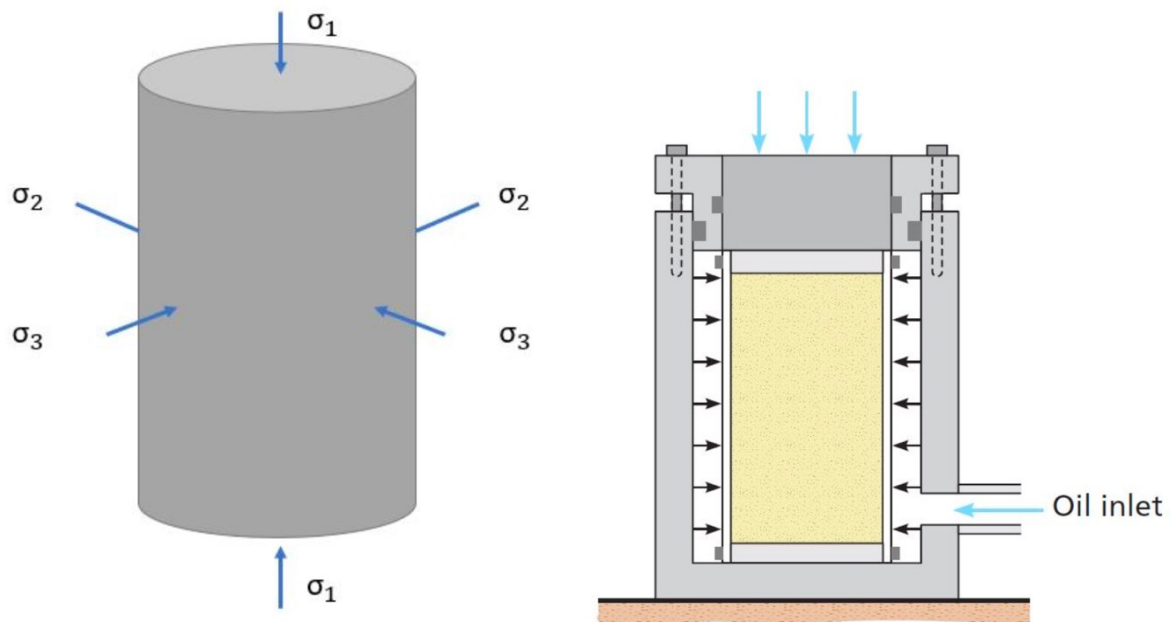


Figure 33: Left: The main stresses σ_1 , σ_2 and σ_3 in the rock mass and the sample cylinder. In the test setup σ_2 and σ_3 are equal. Right: The forces acting in the experiment illustrated by arrows. The main stress (σ_1) is vertical and the confining stress (σ_3) is horizontal. After Gonzalez De Vallejo and Ferrer (2011).

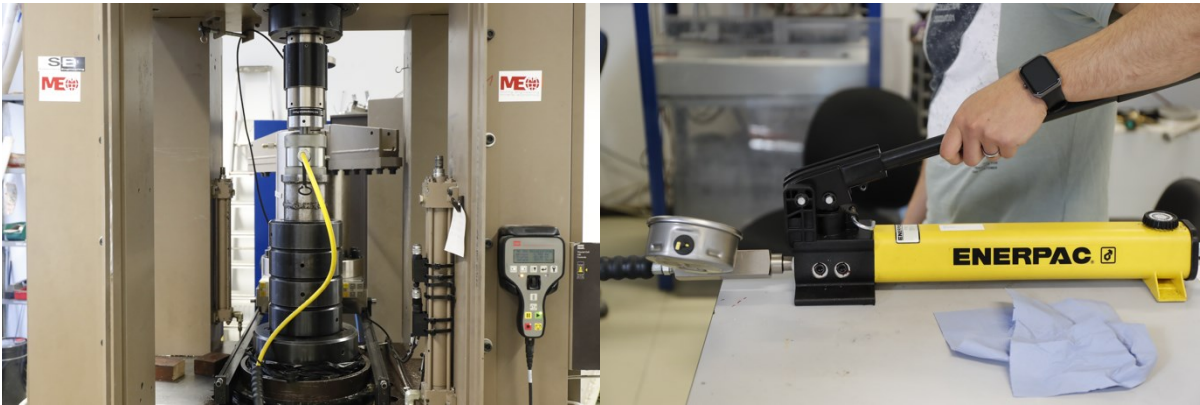


Figure 34: Left: Triaxial press used with oil pressure supply line for the confining pressure. Right: The pump used for the generation of the confining pressure.

3. Results

3.1. Field methods

3.1.1. 2D ERT

30 tests were carried out as part of the ERT measurements. Unfortunately, due to technical errors, some results had to be partially or completely discarded as their quality was insufficient for further analysis. The exact list can be found in the appendix.

The results of the tomography are shown below (Figure 35, Figure 36, Figure 37).

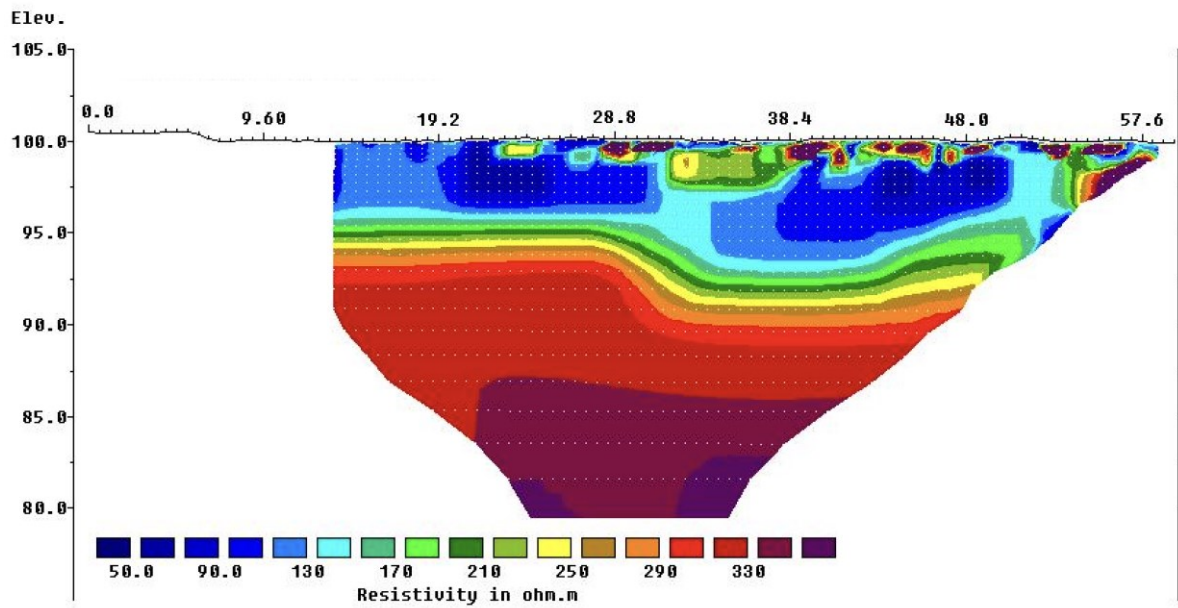


Figure 35: Graphical result of the inversion of the pole-dipole ERT measurement. The color scale represents the resistance in Ωm . The x-axis shows the profile line and the numbers represent the distance to the tunnel face. The elevation in meters is shown on the y-axis.

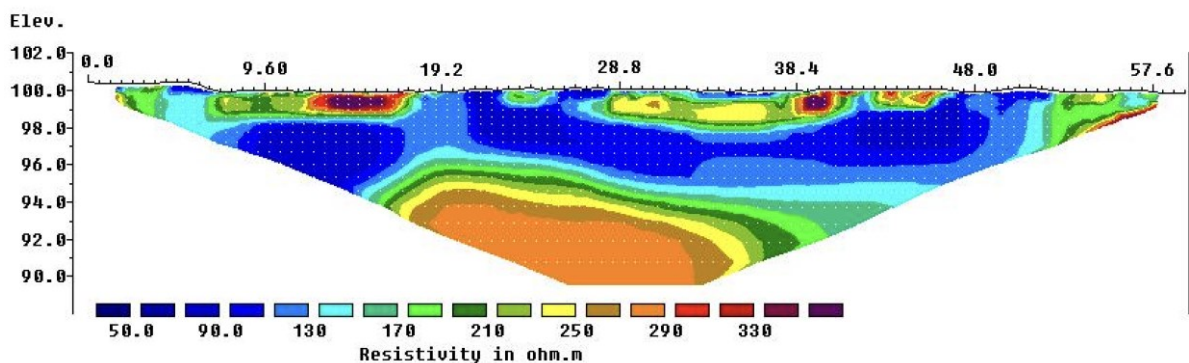


Figure 36: Graphical result of the inversion of the Wenner- α ERT measurement. The color scale represents the resistance in Ωm . The x-axis shows the profile line and the numbers represent the distance to the tunnel face. The elevation in meters is shown on the y-axis.

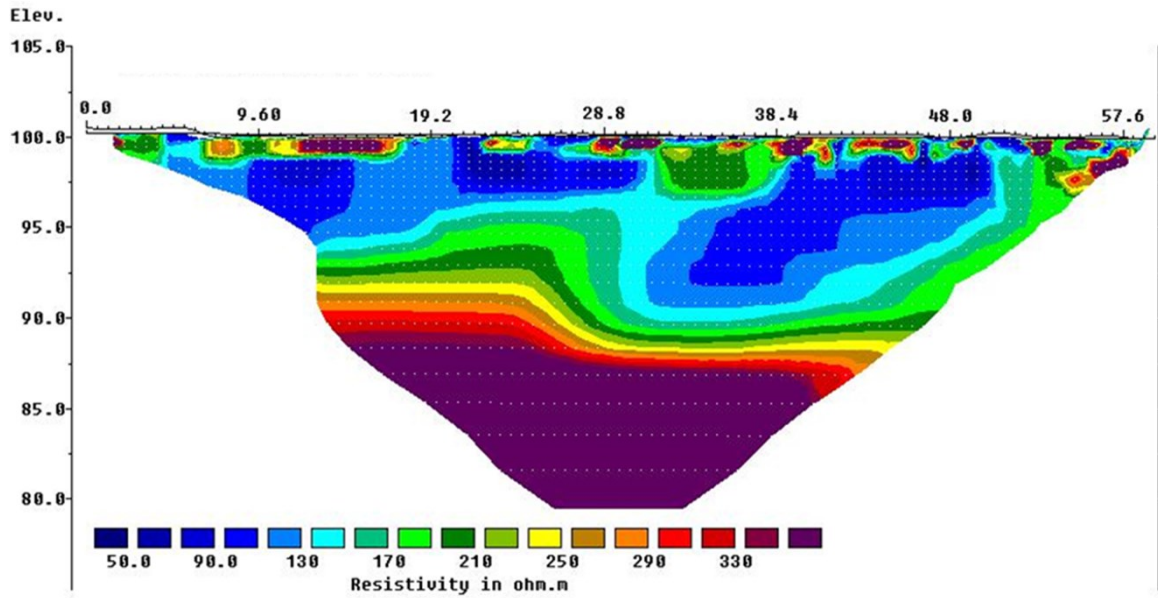


Figure 37: Graphical result of the combined inversion of pole-dipole and Wenner- α ERT measurements. The color scale represents the resistance in Ωm . The x-axis shows the profile line and the numbers represent the distance to the tunnel face. The elevation in meters is shown on the y-axis.

3.1.2. 3D ERT

3.1.2.1. Wenner- α

The results of the Wenner- α ERT array setup were analyzed using Res3DInv to create a tomogram. For further evaluation in this thesis, a cross-section was generated in the X-Z (Figure 38) and X-Y axes (Figure 39). The other cross-sections can be found in the appendix.

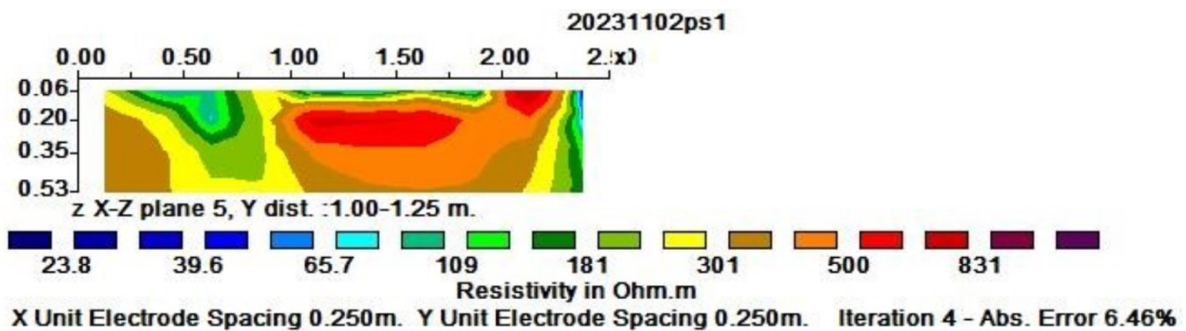


Figure 38: Cross-section through the middle of the 3D tomogram of the ERT array measurement with Wenner- α setup in X-Z plane. The axis marking is given in meters. The resistances are given in Ωm , with red colors indicating high resistances and green/blue colors indicating low resistances.

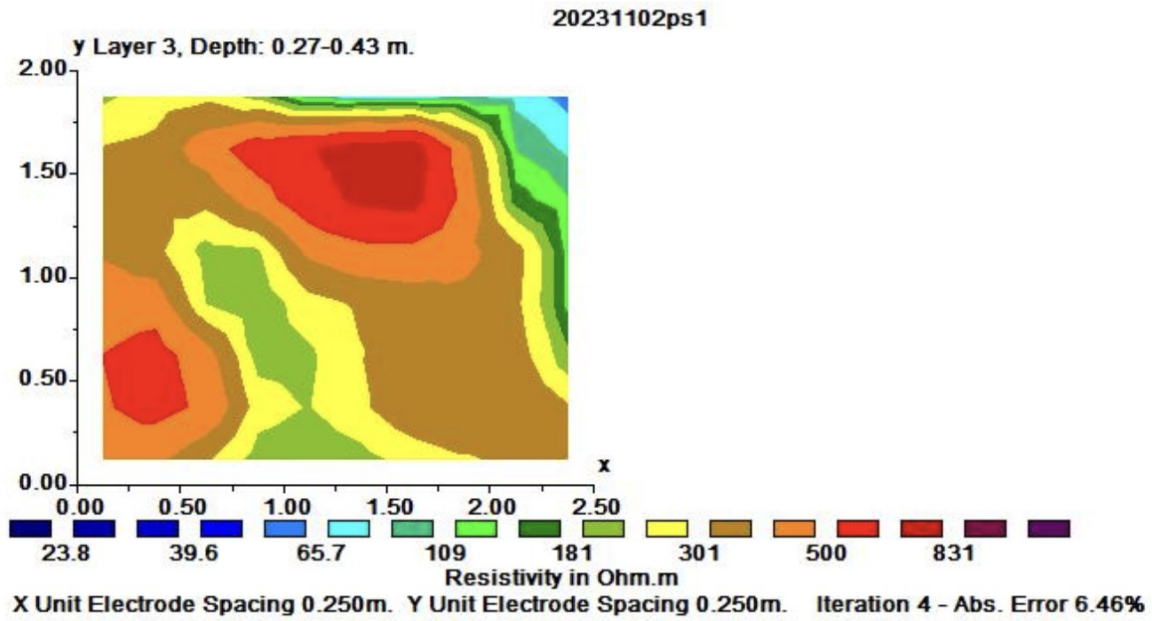


Figure 39: Cross-section through the 3D tomogram of the ERT array measurement with Wenner- α setup in X-Y plane at a depth of approximately 35 cm. The axis marking is given in meters. The resistances are given in Ωm , with red colors indicating high resistances and green/blue colors indicating low resistances.

3.1.2.2. Pole – Pole

The results of the Pole – Pole ERT array were analyzed using Res3DInv to create a tomogram. The graphical results are shown below (Figure 40, Figure 41).

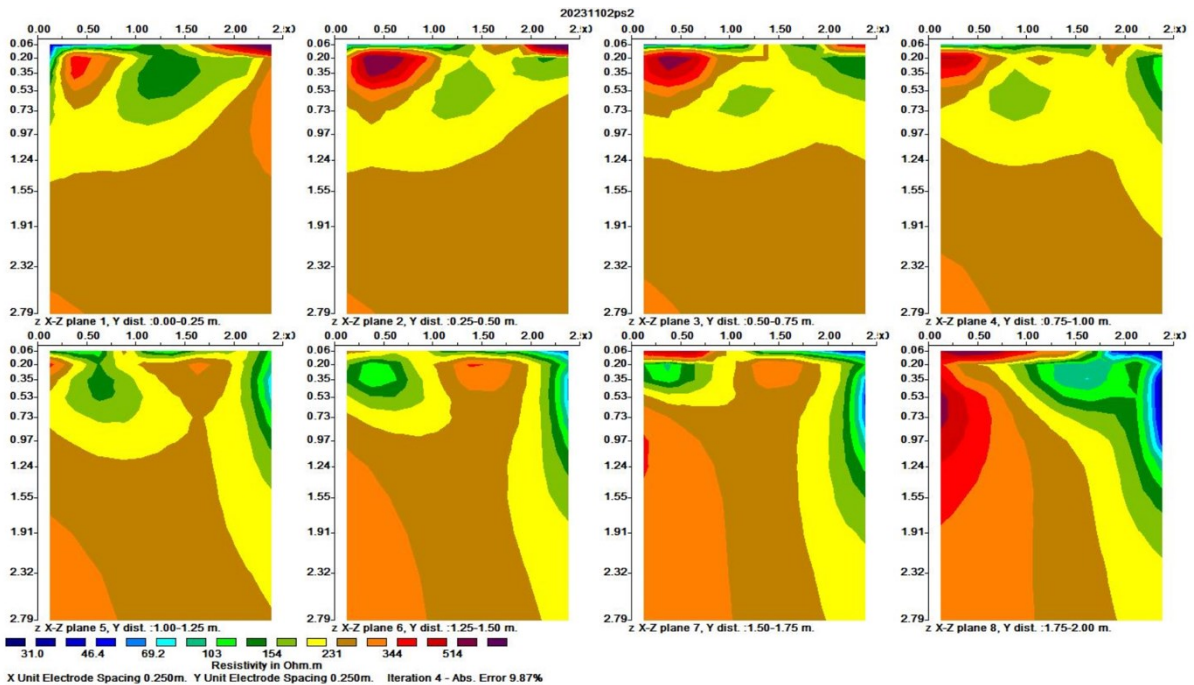


Figure 40: Cross-sections through the 3D tomogram of the ERT array measurement with Pole – Pole setup in X-Z plane for different Y values starting from the top left with 0.00 – 0.25 m to the bottom right with 1.75 – 2.00 m. The axis markings are given in meters. The resistances are given in Ωm , with red colors indicating high resistances and green/blue colors indicating low resistances.

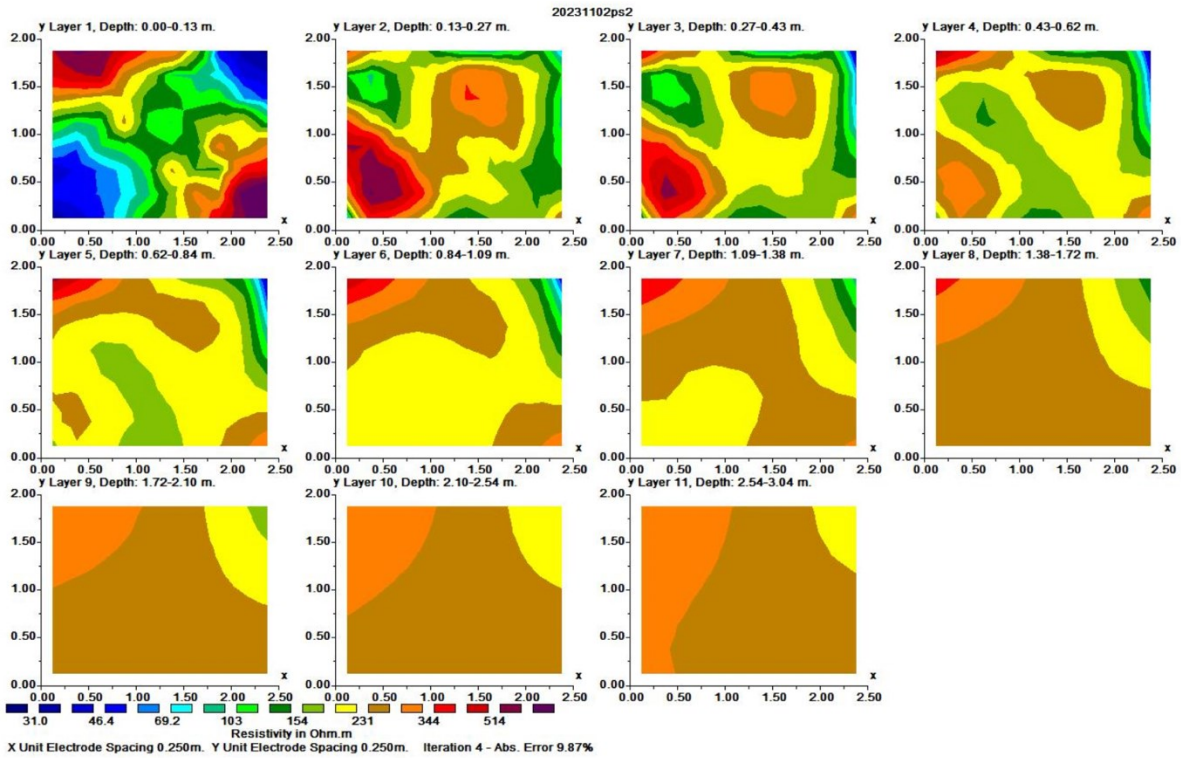


Figure 41: Cross-sections through the 3D tomogram of the ERT array measurement with Pole – Pole setup in X-Y plane for different depths starting from the top left with 0.00 – 0.13 m to the bottom right with 2.54 – 3.04 m. The axis markings are given in meters. The resistances are given in Ωm , with red colors indicating high resistances and green/blue colors indicating low resistances.

3.1.3. 2D Seismic

The results of the seismic investigations are presented below. The data quality was checked with a way-time diagram (Figure 42) and shows good quality along the profile, but also shows problems at the first-break point, which were subsequently corrected with the help of RadExPro.

Overall, the lines were smoothed. The lines 3, 8, 10, 11, 15, 16, 17, 19, 23, 24, 25, 26, 27, 28, 29, 30, 32, 33, 34, 35, 38, 39, 40, 41, 43, 45, 47, 50, 52, 54, 56, 57, 59, 61, 63, 65, 66, 67, 68, 69, 70 and 71 were deleted (Figure 43).

The raw seismic data was used to create a model with 80x40 blocks according to the Wiechert Herglotz method (Figure 44). A constant velocity of 4200 m/s and a maximum velocity of 6000 m/s were assumed as parameters. This model was refined over 160 iterations and finally had an RMS of 0.49 (Figure 47), although this value was almost reached after around 25 iterations (Figure 46, Figure 45). The graphical results can be found in the following.



Figure 42: All seismic data points with the offset on the x-axis and the time on the y-axis to evaluate the data quality.

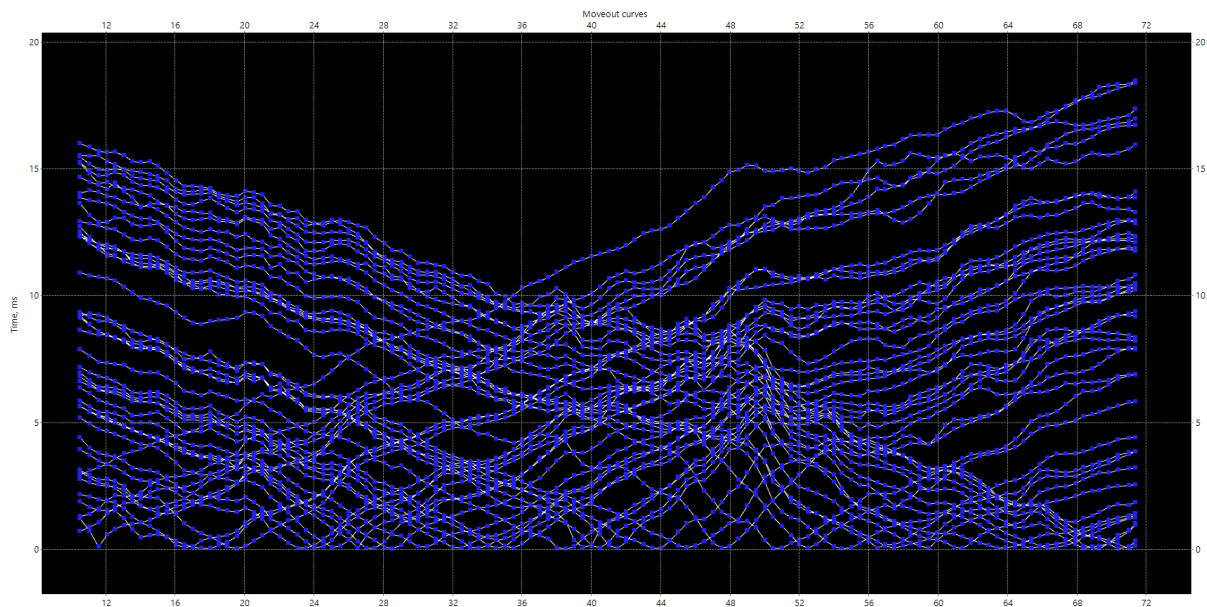


Figure 43: The data selected and processed for seismic tomography. The results of shot points 3,8,10,11,15,16,17,19,23,24,25,26,27,28,29,30,32,33,34,35,38,39,40,41,43,45,47,50,52,54,56,57,59,61,63,65,66,67,68,69,70, 71 are shown with the time on the y-axis and the distance on the x-axis in meters. The tunnel face is on the right side.

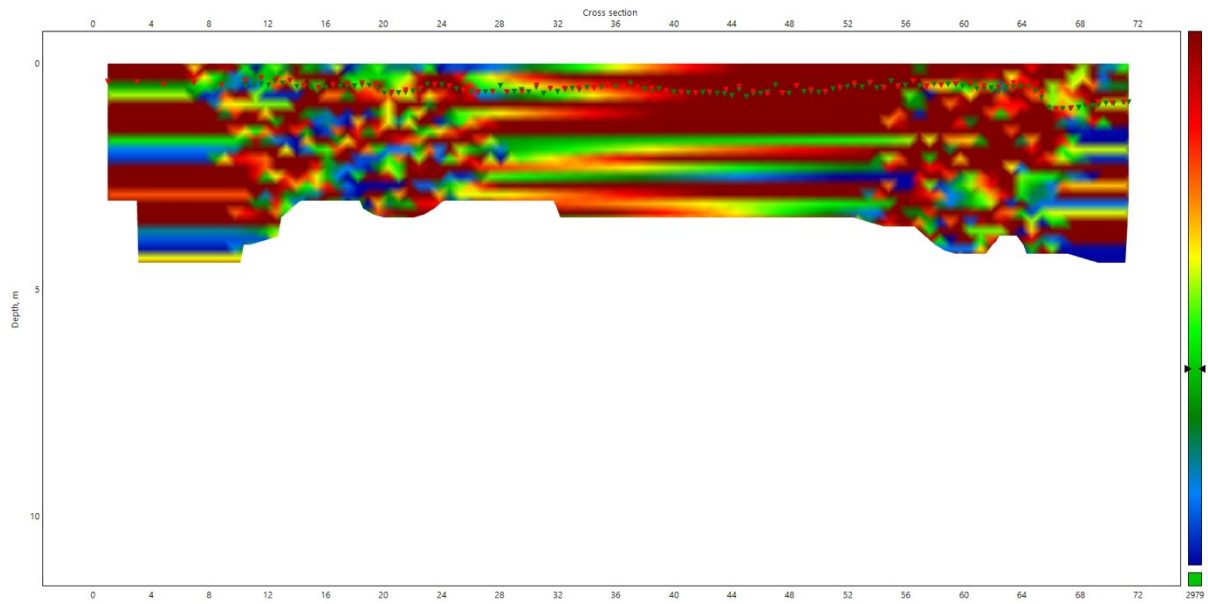


Figure 44: The initial model of tomography according to the Wiechert Herglotz method with 80 columns and 40 rows. As an assumption, a constant speed of 4200 m/s was used to start with and a maximum speed of 6000 m/s was assumed. The red triangles represent the position of the shot points and the green triangles those of the geophones. Depth is shown on the y-axis and the horizontal distance on the x-axis in meters. The tunnel face is on the right side.

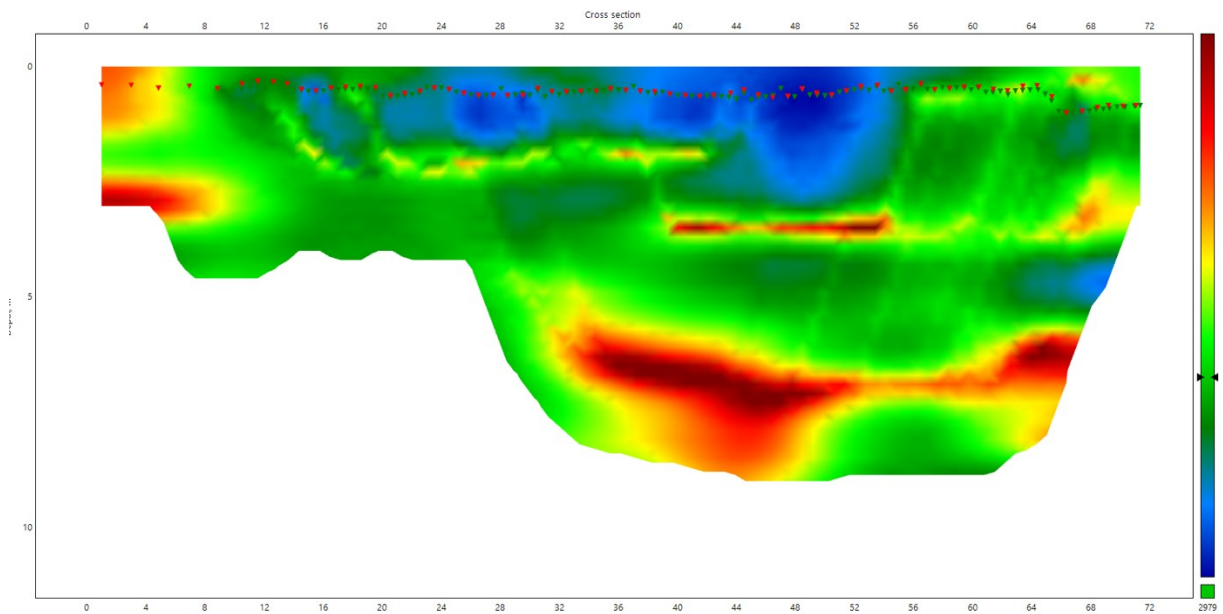


Figure 45: The seismic tomography after 25 iterations. The red triangles represent the position of the shot points and the green triangles those of the geophones. Depth is shown on the y-axis and the horizontal distance on the x-axis in meters. The tunnel face is on the right side.

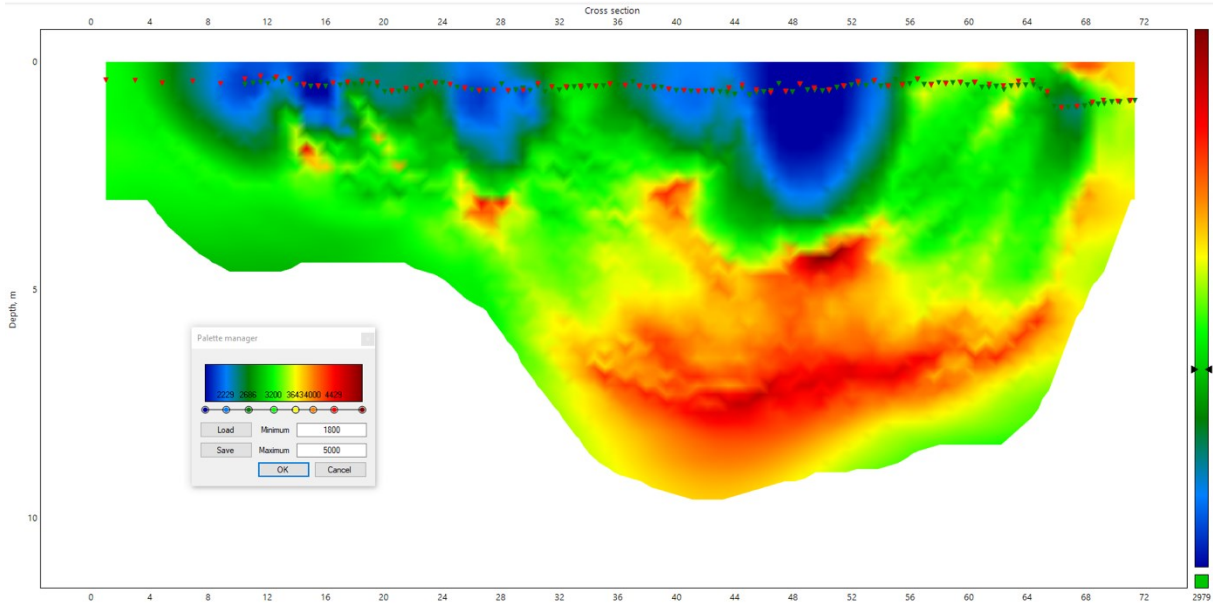


Figure 46: The final tomogram of the seismic experiment after 160 iterations with color gradation of the velocities from 1800 m/s to 5000 m/s. The red triangles represent the position of the shot points and the green triangles those of the geophones. Depth is shown on the y-axis and the horizontal distance on the x-axis in meters. The tunnel face is on the right side.

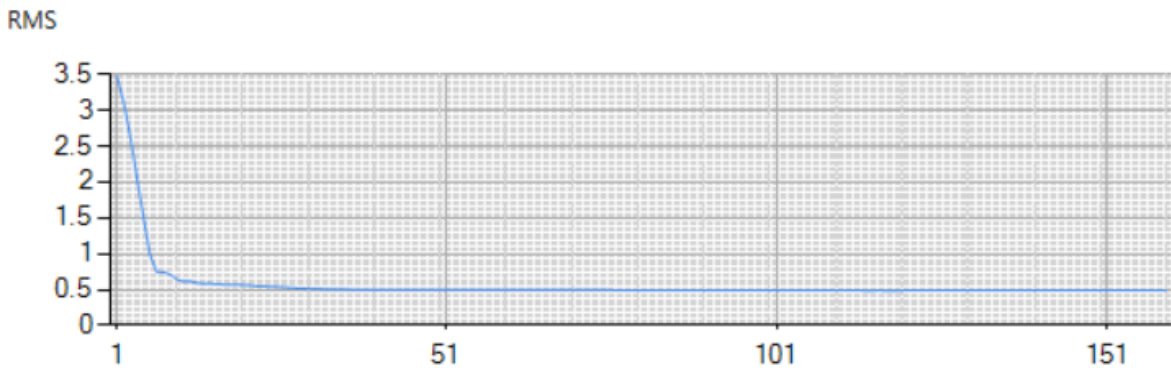


Figure 47: RMS value of the tomography performed with the RMS value on the y-axis and the number of iterations on the x-axis.

3.1.4. Geodesy

This section presents the data from the survey (Figure 48, Figure 49). The figures show the data in a reference system for this work without connection to a general reference system. The x-y axis is shown at the top and the x-z axis at the bottom of the figures. The tunnel face is located on the right-hand side of each figure. The lengths are given in meters.

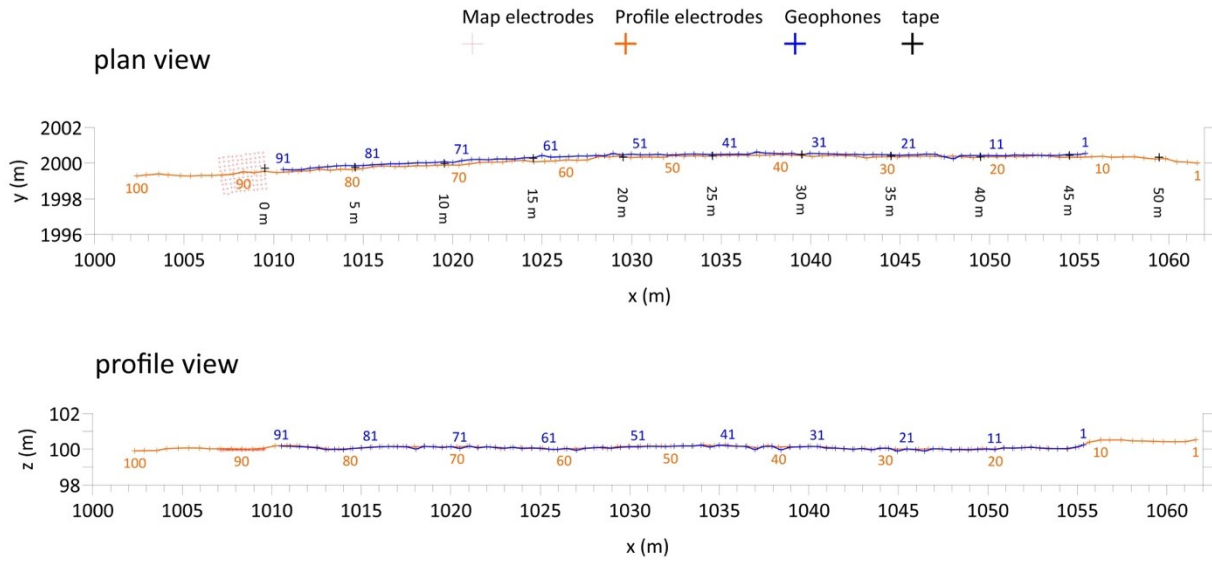


Figure 48: Graphical representation of the survey data with x-y axis at the top and x-z axis at the bottom. The profile starts outside the steel arch section and extends to the tunnel face. The array of the 3D ERT can be seen in the upper part. The position of the electrodes for the 2D ERT, the meters of the scale tape, which was used during the entire project, can also be seen. Also included are the positions of the first seismic survey, which were later extended to a longer line. x, y and z-axis are labeled in meters. The numbers for electrodes and geophones stand for their respective numbers during the survey.

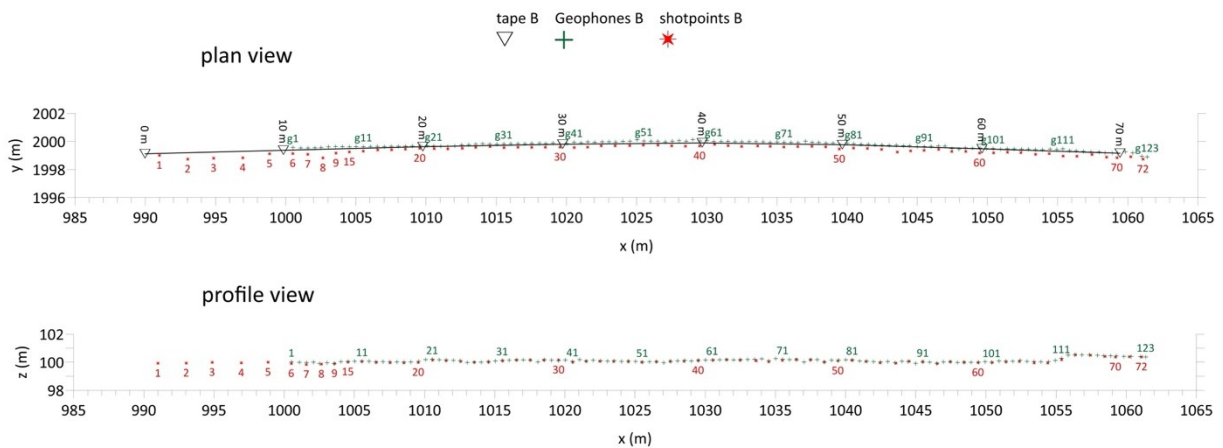


Figure 49: Graphical representation of the survey data with x-y axis at the top and x-z axis at the bottom. The profile starts outside the steel arch section and extends to the tunnel face. Included are the measuring tape "tape B" (black) which was extended for the seismic survey, the positions of the geophones (green) and the shot points (red) from which the impulse for the seismic survey was sent in the ground. x, y and z-axis are labeled in meters.

3.1.5. Deformation observation

When assessing the deformation, all arches in the steel arch area were photographed and numbered. If not otherwise used in the thesis, the images can be found in the appendix. The evaluation was carried out twice in order to minimize possible differences from subjective perception. The results are in tabular form in the appendix and are presented graphically with a rolling average of 5 arches below (Figure 50).

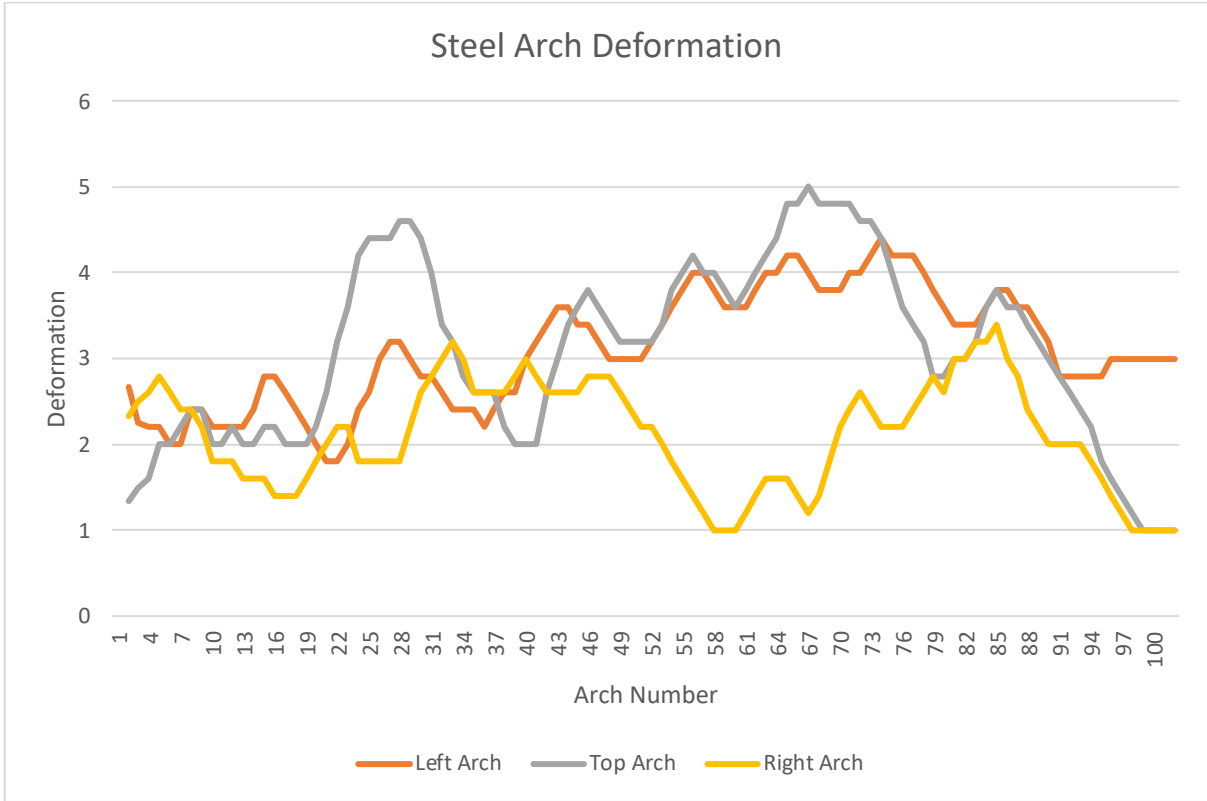


Figure 50: Graphical representation of the determined deformation results for both walls and the crown. The graphs show a rolling average of 5 arches so that trends are easier to recognize.

3.2. Laboratory methods

3.2.1. Water content

Table 3: Tabular presentation of the results relevant to the water content.

sample	2b	3t	4t	4o
container mass [g]	262	355,8	262,3	264,3
wet mass + container mass [g]	3904,0	2886,0	3169,0	3123,0
wet mass [g]	3642,0	2530,2	2906,7	2858,7
dry mass + container mass [g]	3826	2657,0	2871,0	2993,0
dry mass [g]	3564	2301,2	2608,7	2728,7
water content [%]	2,14	9,05	10,25	4,55
sample	2t	1o	2o	5o
container mass [g]	465,5	267,7	671,4	338,3
wet mass + container mass [g]	2949,3	2388,3	3377,0	3079,1
wet mass [g]	2483,8	2120,6	2705,6	2740,8
dry mass + container mass [g]	2674	2232,0	3198,0	2940,0
dry mass [g]	2208,5	1964,3	2526,6	2601,7
water content [%]	11,08	7,37	6,62	5,08

3.2.2. Sieving

Due to unexplained deviations in the measurement results, the scales used were compared with each other using a calibration weight and a deviation of -6 g at 3 kg was found. While the sieved fractions were weighed with the finer scale, the weighing of the total sample was done with a different scale due to the weight restriction of the finer scale. The difference has been taken into account in the following results.

The results are then presented in the form of a sieve curve with a picture of the sieved fractions (Figure 51, Figure 52, Figure 53, Figure 54, Figure 55, Figure 56, Figure 57, Figure 58). The calculated coefficients are presented in tabular form (Table 4).

3.2.2.1. Sieving 1o

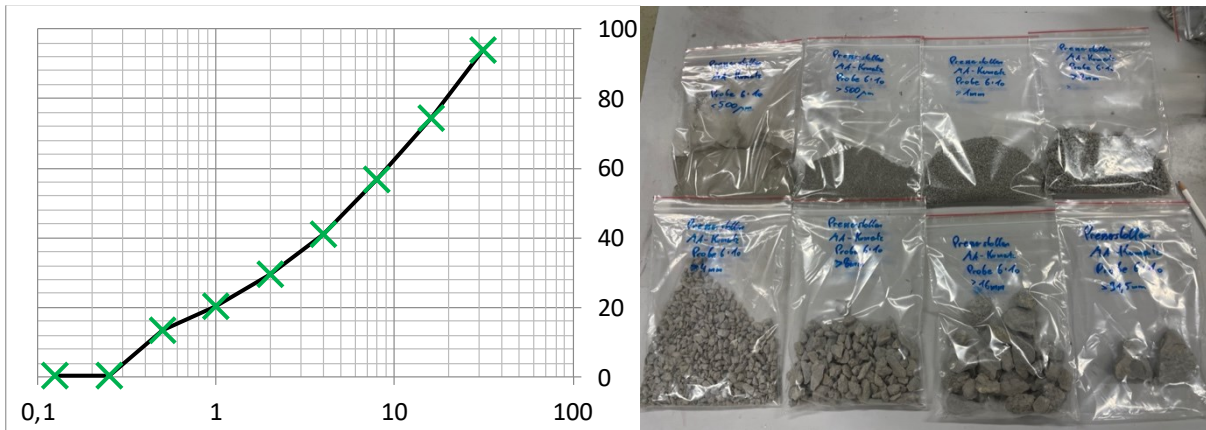


Figure 51: Left: The grain size distribution of the sample 1o in the form of a sieve curve showing the measuring points as green crosses with a linearly interpolated black line. The scaling shows the sieve pass in the vertical axis from 0 % to 100 %. The horizontal axis is logarithmically scaled and shows the grain size in mm. Right: An image of the individual sieved grain fractions of sample 1o.

3.2.2.2. Sieving 2o

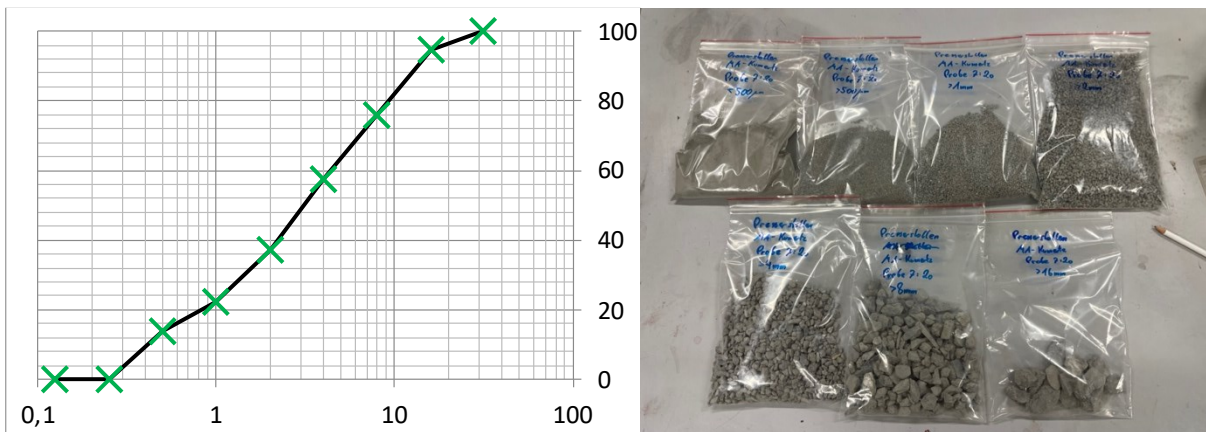


Figure 52: Left: The grain size distribution of the sample 2o in the form of a sieve curve showing the measuring points as green crosses with a linearly interpolated black line. The scaling shows the sieve pass in the vertical axis from 0 % to 100 %. The horizontal axis is logarithmically scaled and shows the grain size in mm. Right: An image of the individual sieved grain fractions of sample 2o.

3.2.2.3. Sieving 2b

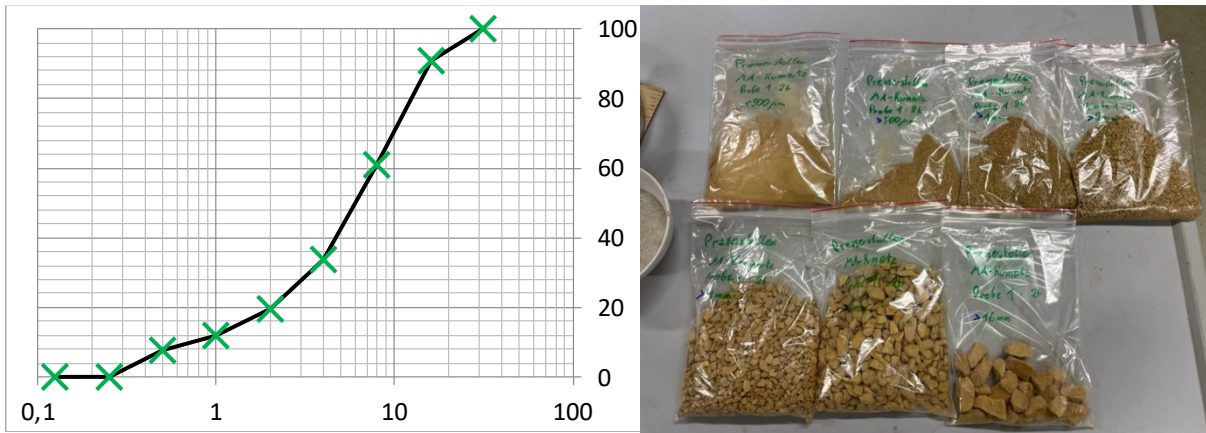


Figure 53: Left: The grain size distribution of the sample 2b in the form of a sieve curve showing the measuring points as green crosses with a linearly interpolated black line. The scaling shows the sieve pass in the vertical axis from 0 % to 100 %. The horizontal axis is logarithmically scaled and shows the grain size in mm. Right: An image of the individual sieved grain fractions of sample 2b.

3.2.2.4. Sieving 2t

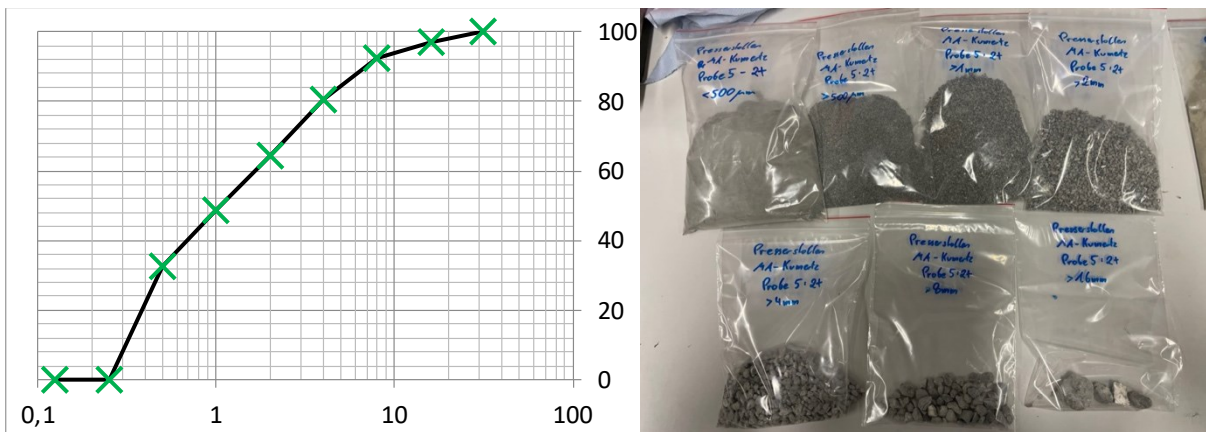


Figure 54: Left: The grain size distribution of the sample 2t in the form of a sieve curve showing the measuring points as green crosses with a linearly interpolated black line. The scaling shows the sieve pass in the vertical axis from 0 % to 100 %. The horizontal axis is logarithmically scaled and shows the grain size in mm. Right: An image of the individual sieved grain fractions of sample 2t.

3.2.2.5. Sieving 3t

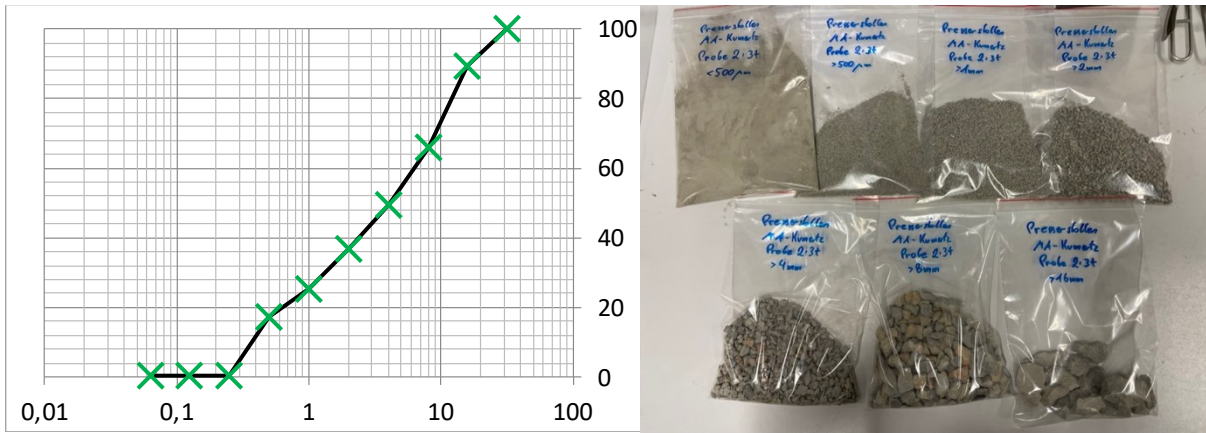


Figure 55: Left: The grain size distribution of the sample 3t in the form of a sieve curve showing the measuring points as green crosses with a linearly interpolated black line. The scaling shows the sieve pass in the vertical axis from 0 % to 100 %. The horizontal axis is logarithmically scaled and shows the grain size in mm. Right: An image of the individual sieved grain fractions of sample 3t.

3.2.2.6. Sieving 4o

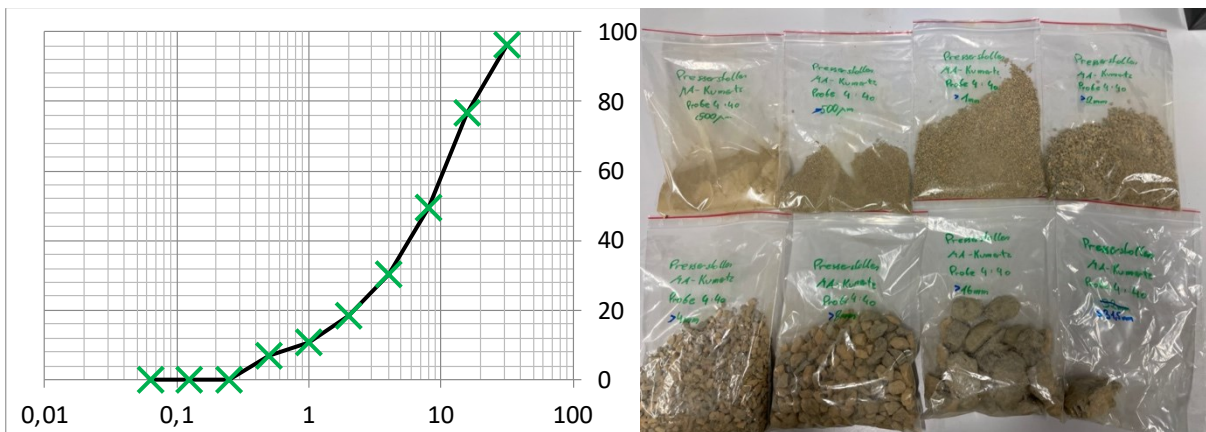


Figure 56: Left: The grain size distribution of the sample 4o in the form of a sieve curve showing the measuring points as green crosses with a linearly interpolated black line. The scaling shows the sieve pass in the vertical axis from 0 % to 100 %. The horizontal axis is logarithmically scaled and shows the grain size in mm. Right: An image of the individual sieved grain fractions of sample 4o.

3.2.2.7. Sieving 4t

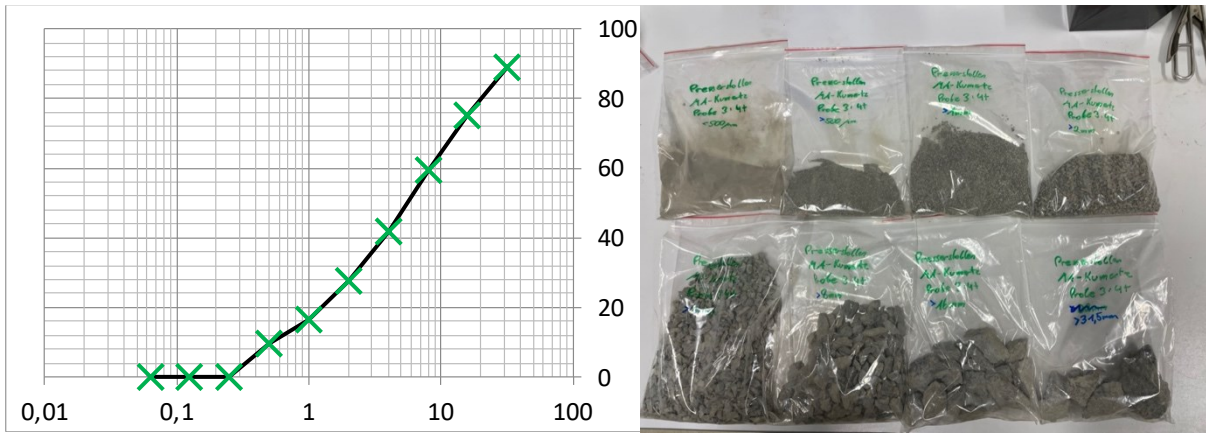


Figure 57: Left: The grain size distribution of the sample 4t in the form of a sieve curve showing the measuring points as green crosses with a linearly interpolated black line. The scaling shows the sieve pass in the vertical axis from 0 % to 100 %. The horizontal axis is logarithmically scaled and shows the grain size in mm. Right: An image of the individual sieved grain fractions of sample 4t.

3.2.2.8. Sieving 5o

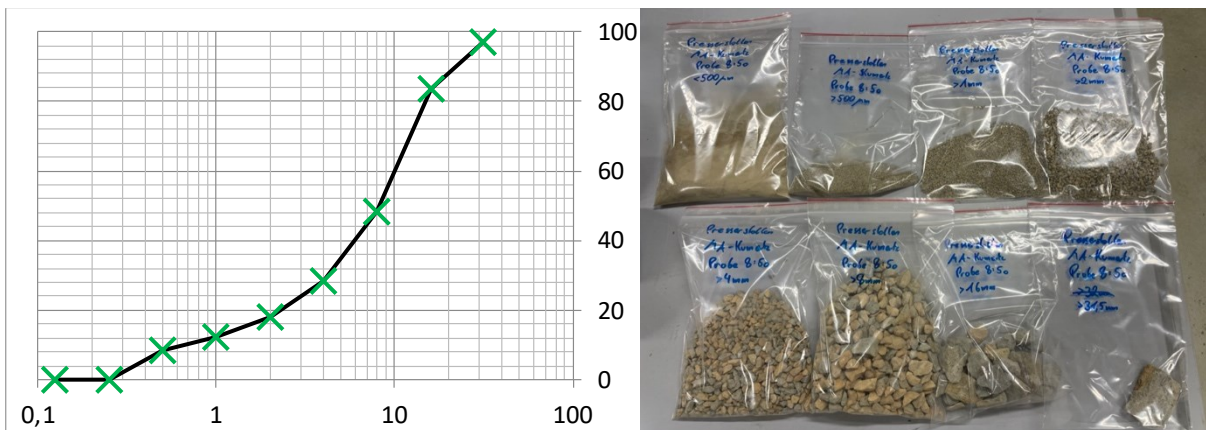


Figure 58: Left: The grain size distribution of the sample 5o in the form of a sieve curve showing the measuring points as green crosses with a linearly interpolated black line. The scaling shows the sieve pass in the vertical axis from 0 % to 100 %. The horizontal axis is logarithmically scaled and shows the grain size in mm. Right: An image of the individual sieved grain fractions of sample 5o.

Table 4: D_{10} , D_{30} and D_{60} for the sieved samples and the parameters C_c and U calculated from them.

	D_{10} [mm]	D_{30} [mm]	D_{60} [mm]	C_c	U
Probe 1 (2b)	0,72	3,3	7,5	2,0	10,4
Probe 2 (3t)	0,25	1,25	6,1	1,0	24,4
Probe 3 (4t)	0,51	2,1	7,9	1,1	15,5
Probe 4 (4o)	0,82	4	10,2	1,9	12,4
Probe 5 (2t)	0,15	0,46	1,5	0,9	10,0
Probe 6 (1o)	0,35	2,05	9	1,3	25,7
Probe 7 (2o)	0,33	1,3	4,3	1,2	13,0

Probe 8 (5o)	0,7	4,1	10	2,4	14,3
--------------	-----	-----	----	-----	------

3.2.3. Measurements

Table 5: Sample height measurements and resulting averages.

sample	height 1 [mm]	height 2 [mm]	height 3 [mm]	height average [mm]
PS I 1	40,52	40,64	40,8	40,65
PS I 2	38,23	38,12	38,52	38,29
PS I 3	40,25	40,19	40,26	40,23
PS II 1	24,69	24,98	25,14	24,94
PS II 1 (grün)	11,52	11,62	11,88	11,67
PS II 2	27,7	27,71	27,32	27,58
PS II 2 (grün)	12,26	11,49	11,35	11,70
PS II 3	20,2	20,18	20,02	20,13
PS II 3 (grün)	17,11	15,47	16,1	16,23
PS III 1	31,99	31,86	32,26	32,04
PS III 2	33,63	31,95	32,67	32,75
PS IV	27,08	27,17	27,9	27,38
PS V	32,25	32,22	32,14	32,20
PS VI 1.2	28,03	27,81	28,64	28,16
PS VI 2.1	25,92	26,1	26,03	26,02
PS VI 2.2	24,81	24,19	24,28	24,43
PS VI 3	45,32	45,46	45,32	45,37
PS VI 4	51,92	50,92	51,35	51,40

Table 6: Sample diameter measurements and resulting averages.

sample	diameter 1 [mm]	diameter 2 [mm]	diameter 3 [mm]	diameter average [mm]
PS I 1	28,81	28,78	28,57	28,72
PS I 2	28,72	28,83	28,58	28,71
PS I 3	28,45	28,49	28,50	28,48
PS II 1	28,63	28,66	28,50	28,60
PS II 1 (grün)	28,6	28,63	28,66	28,63

PS II 2	28,58	28,53	28,53	28,55
PS II 2 (grün)	28,66	28,57	28,54	28,59
PS II 3	28,45	28,45	28,66	28,52
PS II 3 (grün)	28,64	28,52	28,52	28,56
PS III 1	28,51	28,54	28,66	28,57
PS III 2	28,54	28,63	28,43	28,53
PS IV	48,64	48,6	48,89	48,71
PS V	48,85	48,75	48,51	48,70
PS VI 1.2	28,52	28,6	28,54	28,55
PS VI 2.1	28,55	28,55	28,83	28,64
PS VI 2.2	28,59	28,6	28,73	28,64
PS VI 3	28,41	28,35	28,49	28,42
PS VI 4	28,43	28,52	28,47	28,47

Table 7: Sample weight dry, saturated, with buoyancy and the calculated porosity.

sample	dry mass 2nd [g]	saturated mass [g]	with buoyancy (g)	porosity [%]
PS I 1	71,07	71,41	45,7	1,32
PS I 2	66,48	66,79	42,63	1,28
PS I 3	no test	no test	no test	no test
PS II 1	no test	no test	no test	no test
PS II 1 (grün)	20,44	20,56	13,11	1,61
PS II 2	48,83	49,16	31,41	1,86
PS II 2 (grün)	20,5	20,59	13,16	1,21
PS II 3	35,26	35,48	22,62	1,71
PS II 3 (grün)	28,62	28,79	18,42	1,64
PS III 1	56,47	56,85	36,36	1,85
PS III 2	56,71	56,99	36,39	1,36
PS IV	132,52	133,4	85,52	1,84
PS V	164,7	165,25	109,51	0,99
PS VI 1.2	48,5	48,82	31,21	1,82

PS VI 2.1	43,76	44,03	28,19	1,70
PS VI 2.2	43,15	43,36	27,71	1,34
PS VI 3	80,78	81,21	51,99	1,47
PS VI 4	91,17	91,68	58,76	1,55

3.2.4. Helium-Pycnometer

Table 8: Results from the Helium-Pycnometer including the calculated Volume and Porosity.

sample	density [g/cm ³] measured	volume [cm ³] measured	variance [%]	volume [cm ³] calculated	porosity [%]
PS I 1	2,80	25,42	0,07	26,34	3,47
PS I 2	2,78	23,92	0,04	24,79	3,49
PS I 3	2,79	25,66	0,08	25,63	-0,11
PS II 1	2,80	15,77	0,08	16,02	1,56
PS II 1 (grün)	2,79	7,34	0,10	7,51	2,30
PS II 2	2,79	17,49	0,09	17,65	0,91
PS II 2 (grün)	2,77	7,39	0,10	7,51	1,55
PS II 3	2,78	12,67	0,05	12,86	1,49
PS II 3 (grün)	2,80	10,22	0,05	10,40	1,69
PS III 1	2,80	20,21	0,10	20,54	1,59
PS III 2	2,79	20,37	0,10	20,94	2,75
PS IV	too large	no result	no result	51,03	no result
PS V	too large	no result	no result	59,99	no result
PS VI 1.2	2,79	17,59	0,08	18,03	2,43
PS VI 2.1	2,80	15,65	0,10	16,76	6,64
PS VI 2.2	2,79	15,46	0,04	15,74	1,78
PS VI 3	2,80	28,87	0,10	28,77	-0,36
PS VI 4	2,80	32,57	0,05	32,73	0,47

3.2.5. Ultrasonic measurements

Below are the results of the ultrasonic measurements with the evaluation and the resulting speed for the geometry of the samples. Unfortunately, several samples failed structurally during the test (Figure 59), so the samples that were later intended for the triaxial test were not used due to the risk of failure. It is unclear whether the samples failed in compression or tension.

Table 9: Results from the ultrasonic measurement with dry samples.

sample	height average [mm]	p-wave traveltime [μs]	p-velocity [m/s]
PS I 1	40,65	10,63	3824,40
PS I 2	38,29	9,63	3976,12
PS I 3	40,23	10,80	3725,31
PS II 1	24,94	10,00	2493,67
PS II 1 (grün)	11,67	3,04	3839,91
PS II 2	27,58	6,69	4122,07
PS II 2 (grün)	11,70	2,92	4006,85
PS II 3	20,13	5,49	3667,27
PS II 3 (grün)	16,23	5,05	3213,20
PS III 1	32,04	7,73	4144,46
PS III 2	32,75	8,62	3799,30
PS IV	27,38	15,12	1811,07
PS V	32,20	6,93	4644,26
PS VI 1.2	28,16	8,99	3132,37
PS VI 2.1	26,02	6,35	4097,11
PS VI 2.2	24,43	6,05	4037,47
PS VI 3	45,37	no test	no test
PS VI 4	51,40	no test	no test

Table 10: Results from the ultrasonic measurement with water saturated samples.

sample	p-wave traveltime [μs]	p-velocity [m/s]
PS I 1	9,56	4252,44
PS I 2	9,6	3988,54
PS I 3	no test	no test
PS II 1	no test	no test
PS II 1 (grün)	3,28	3558,94
PS II 2	7,12	3873,12
PS II 2 (grün)	2,98	3926,17
PS II 3	4,9	4108,84

PS II 3 (grün)	5,35	3033,02
PS III 1	8,29	3864,49
PS III 2	8,01	4088,63
PS IV	7,7	3556,27
PS V	6,62	4864,55
PS VI 1.2	7,15	3938,46
PS VI 2.1	6,61	3935,95
PS VI 2.2	6,31	3871,10
PS VI 3	no test	no test
PS VI 4	no test	no test

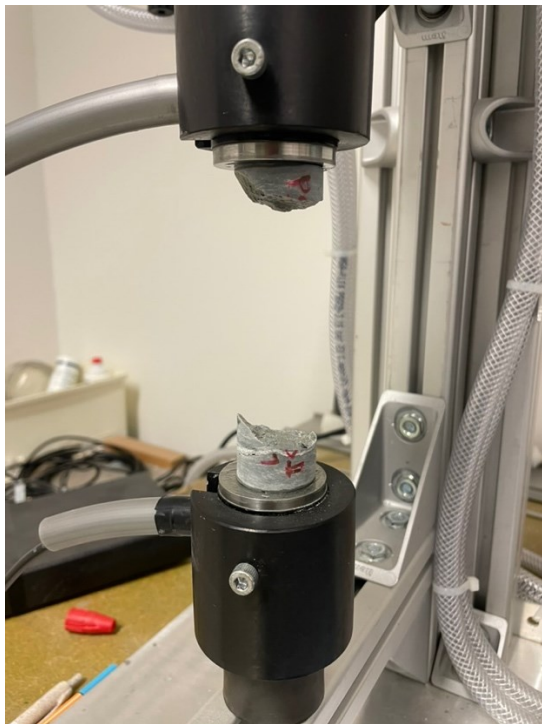


Figure 59: During the test, sample II 1 broke apart, making further investigations of the sample impossible.

3.2.6. Cerchar Abrasivity Index (CAI)

The CAI was determined with three tests and a total of 64 results. The tests on PS VI were performed on the same handpiece on different sides (Figure 60, Figure 61). The evaluated results are presented in this section. Besides the tables (Table 11, Table 12, Table 13), a picture of the test and its orientation to the schistosity is given (Figure 62). The raw data can be found in the appendix.

3.2.6.1. PS VI with schistosity

Table 11: The scratches in this test on sample PS VI were made in the direction of the schistosity. A total of six scratches were made and measured under the digital microscope. The results are presented in this table.

measurements	24
minimum [μm]	10,56
maximum [μm]	52,80
average [μm]	28,45
standard deviation [μm]	13,41

CAI = 0,32

3.2.6.2. PS VI against schistosity

Table 12: The scratches in this test on sample PS VI were made against the schistosity. A total of five scratches were made and measured under the digital microscope. The results are presented in this table.

measurements	20
minimum [μm]	10,56
maximum [μm]	334,40
average [μm]	104,19
standard deviation [μm]	90,91

CAI = 1,19

3.2.6.3. PS III against schistosity

Table 13: The scratches in this test on sample PS III were made against the schistosity. A total of five scratches were made and measured under the digital microscope. The results are presented in this table.

measurements	20
minimum [μm]	17,60
maximum [μm]	49,28
average [μm]	32,56
standard deviation [μm]	6,65

CAI = 0,37

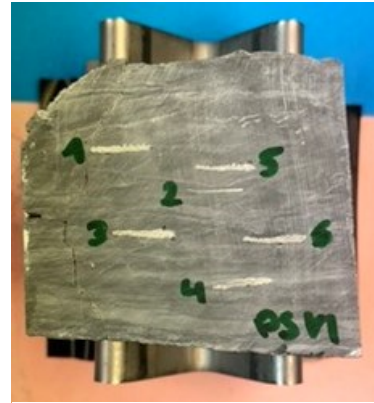


Figure 60: Picture of the sample PSVI after the CAI test. The scored areas are 10 mm long. The individual lines are numbered.

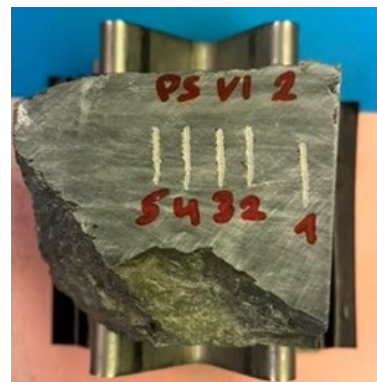


Figure 61: Picture of the sample PSVI after the CAI test. The scored areas are 10 mm long. The individual lines are numbered.



Figure 62: Picture of the sample PSIII after the CAI test. The scored areas are 10 mm long. The individual lines are numbered.

3.2.7. Conductivity measurement

The result of the resistance measurement is shown below. The water used had a conductivity of 432 $\mu\text{S}/\text{cm}$, which corresponds to a resistance of 23 Ω/m . The measurement was carried out twice and the results averaged. They are shown below (Table 14).

Table 14: This table shows the results of the conductivity measurement.

sample	voltage average [Ve-5]	geometry-factor	specific resistance average [Ω/m]
PS I 1	183,50	0,02	2924,14
PS I 2	244,50	0,02	4133,80
PS I 3	no test	no test	no test
PS II 1	no test	no test	no test
PS II 1 (grün)	49,50	0,06	2729,88
PS II 2	99,00	0,02	2297,70
PS II 2 (grün)	64,50	0,05	3539,09
PS II 3	82,00	0,03	2601,88
PS II 3 (grün)	76,00	0,04	3000,48
PS III 1	109,00	0,02	2181,17
PS III 2	198,50	0,02	3875,65
PS IV	44,00	0,07	2994,28
PS V	64,00	0,06	3702,43
PS VI 1.2	125,50	0,02	2853,74
PS VI 2.1	113,50	0,02	2811,13
PS VI 2.2	121,00	0,03	3191,22
PS VI 3	308,00	0,01	4305,76
PS VI 4	278,50	0,01	3450,30

3.2.8. Brazilian test

The results of the Brazilian Test are shown below. The device is designed for a maximum force of 100 kN, which was exceeded for two samples. A value of 100 kN was assumed for the table, but no failure occurred. As no device was available for the small sample diameters of 28 mm, this was supplemented by a flat piece of granite to enable the test to be carried out (Figure 63).

Table 15: This table shows the results of the Brazilian test.

sample	F_{\max} [kN]	Brazilian tensile strength [MPa]
PS II 3 (grün)	7,36	10,11
PS II 2 (grün)	3,54	6,74
PS II 1 (grün)	47,68	90,82
PS IV	100	47,73
PS V	100	40,59

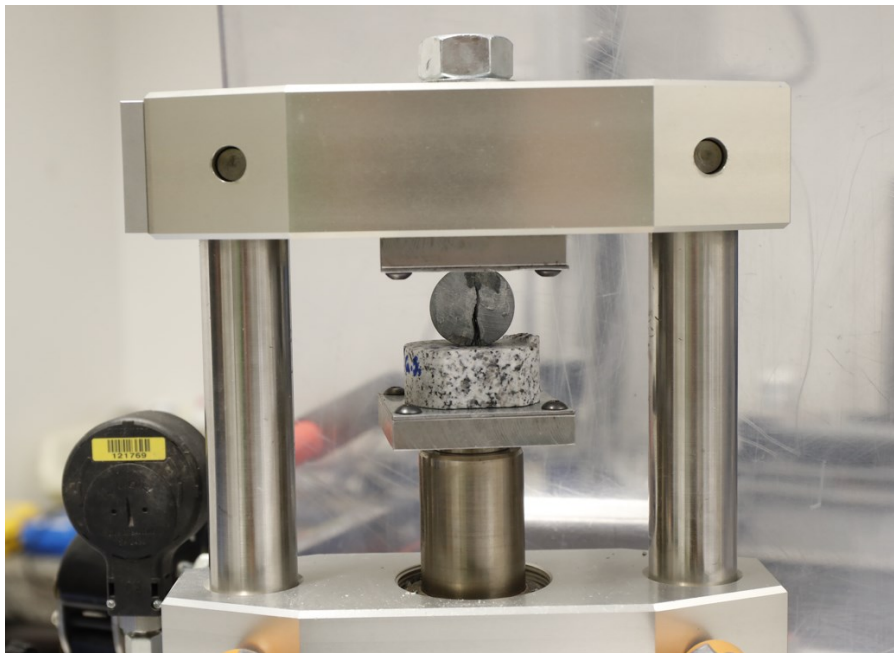


Figure 63: Sample PS II 3 (grün) in the test setup after fracturing.

3.2.9. Triaxial test

This section presents the results of the triaxial tests (Figure 64, Figure 65, Figure 66) and the resulting strength parameters. The PSI_3 sample was stressed evenly from all sides up to 5 MPa. Sample PSVI_4 was stressed evenly up to 10 MPa and sample PSVI_3 up to 15 MPa. Subsequently, only σ_1 was increased. The increase in σ_3 is due to the test setup. The images of the destroyed samples can be found in the appendix.

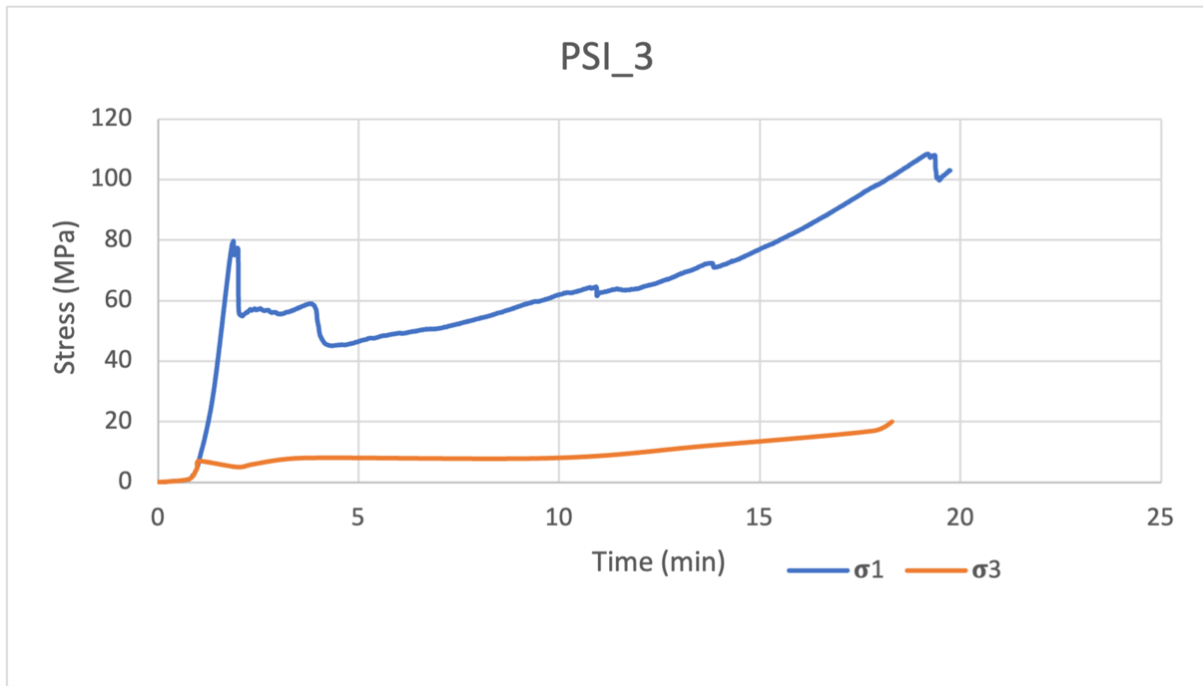


Figure 64: The results of the triaxial test of the sample PSI_3. The time is plotted on the x-axis and the stress on the y-axis. The lines are given for σ_1 and σ_3 . The test was carried out up to the maximum press stroke of 10 mm.

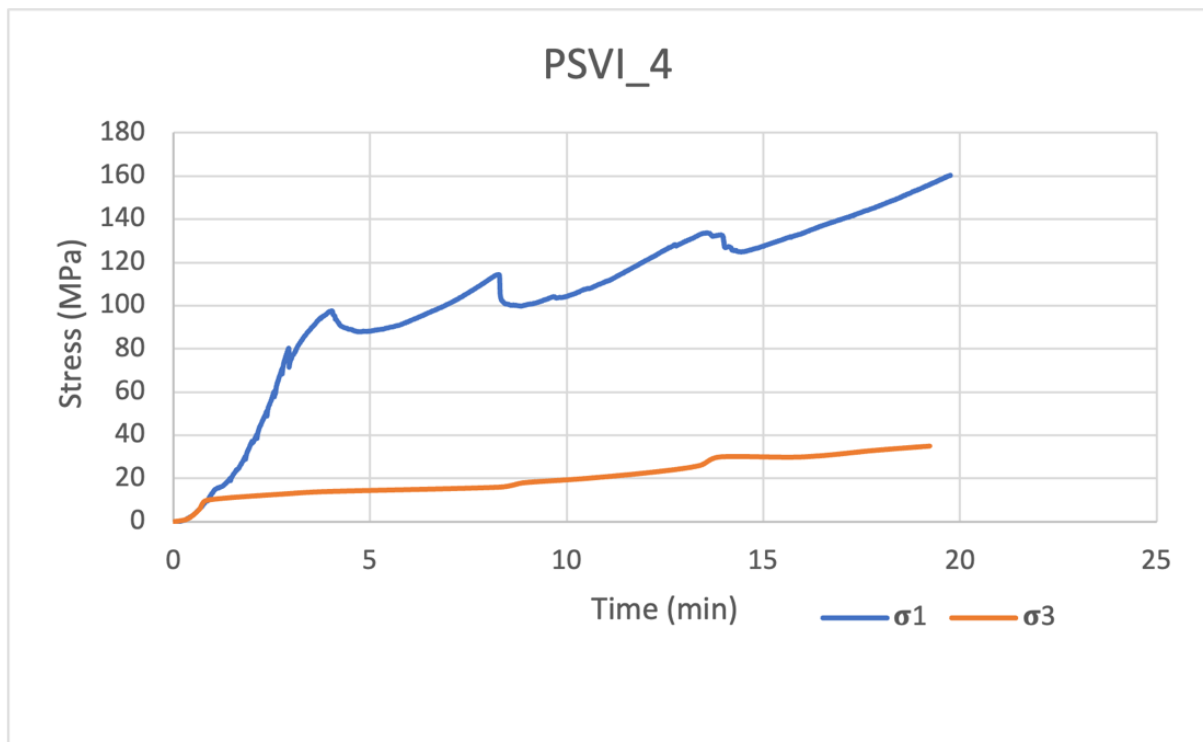


Figure 65: The results of the triaxial test of the sample PSVI_4. The time is plotted on the x-axis and the stress on the y-axis. The lines are given for σ_1 and σ_3 . The test was carried out up to the maximum press stroke of 10 mm.

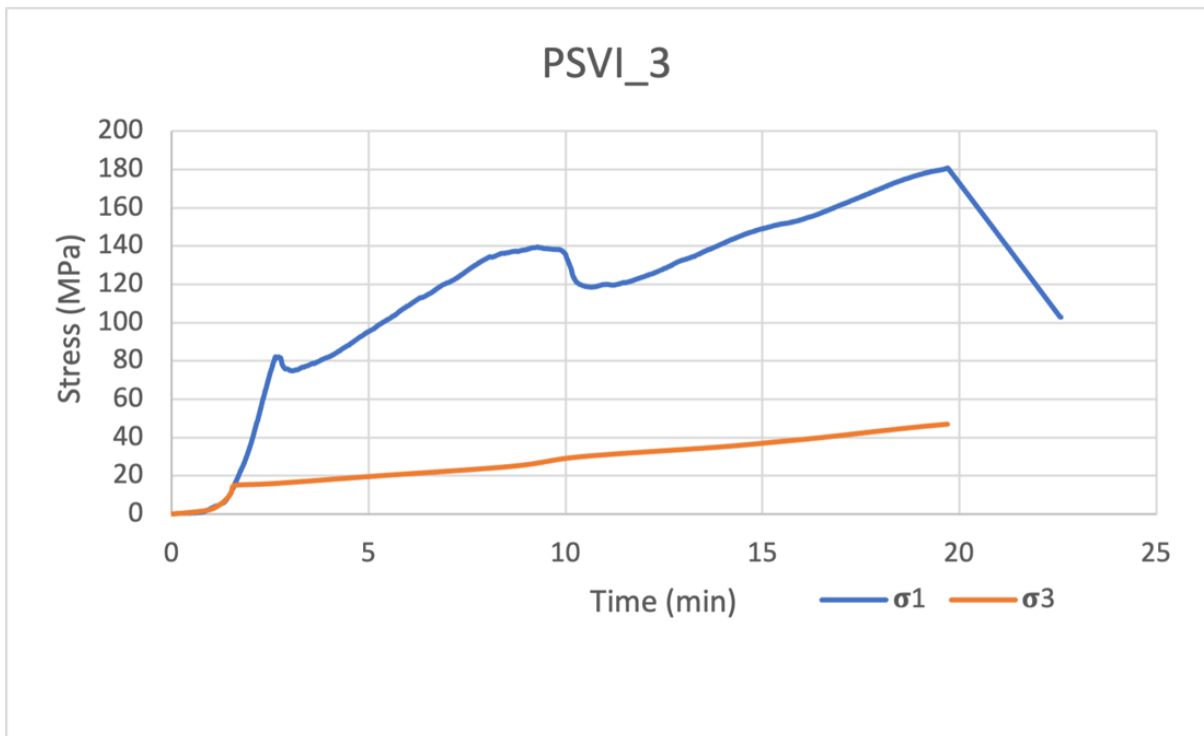


Figure 66: The results of the triaxial test of the sample PSVI_3. The time is plotted on the x-axis and the stress on the y-axis. The lines are given for σ_1 and σ_3 . The test was carried out up to the maximum press stroke of 10 mm.

3.2.9.1. Rock strength

Three significant failures of the samples were used to calculate the rock strength. Failures at higher confining pressure were selected for the calculation of the residual strength. The values used are given in tabular form (Table 16, Table 18). The results are shown graphically and in tabular form (Table 17, Table 19, Figure 67, Figure 68, Figure 69, Figure 70).

Table 16: The values used to calculate the rock strength.

σ_3' [MPa]	σ_1' [MPa]
6	80
12	100
16	115

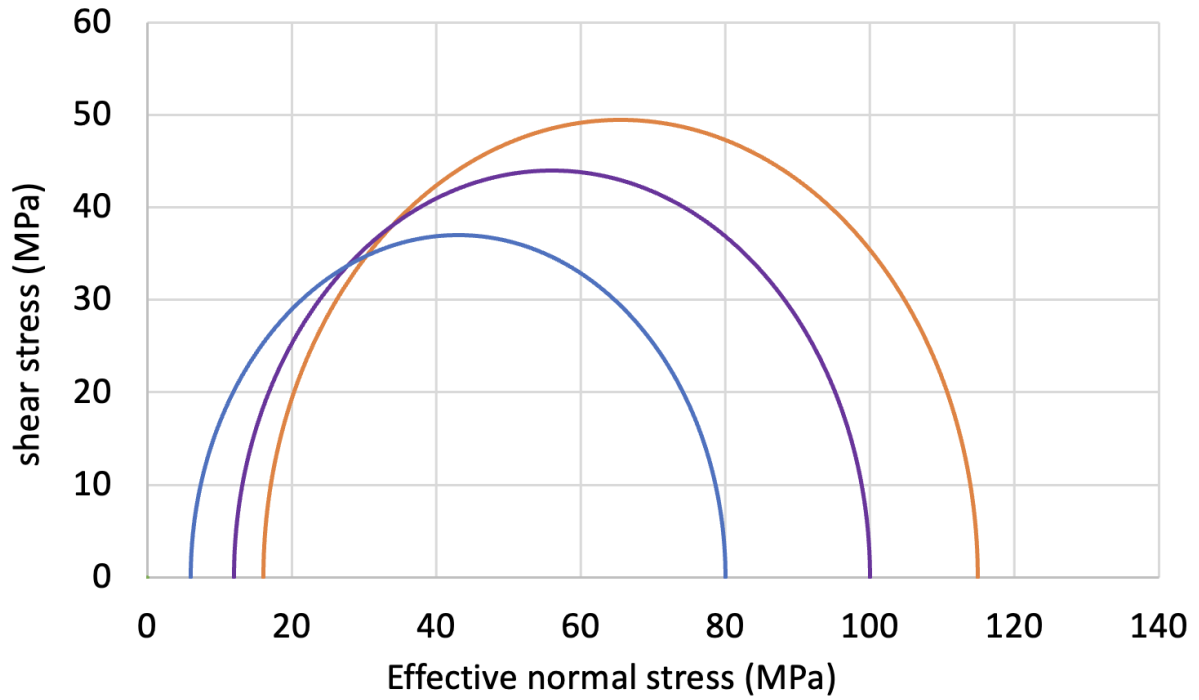


Figure 67: Graphical representation of the stress ratios according to Mohr-Coulomb.

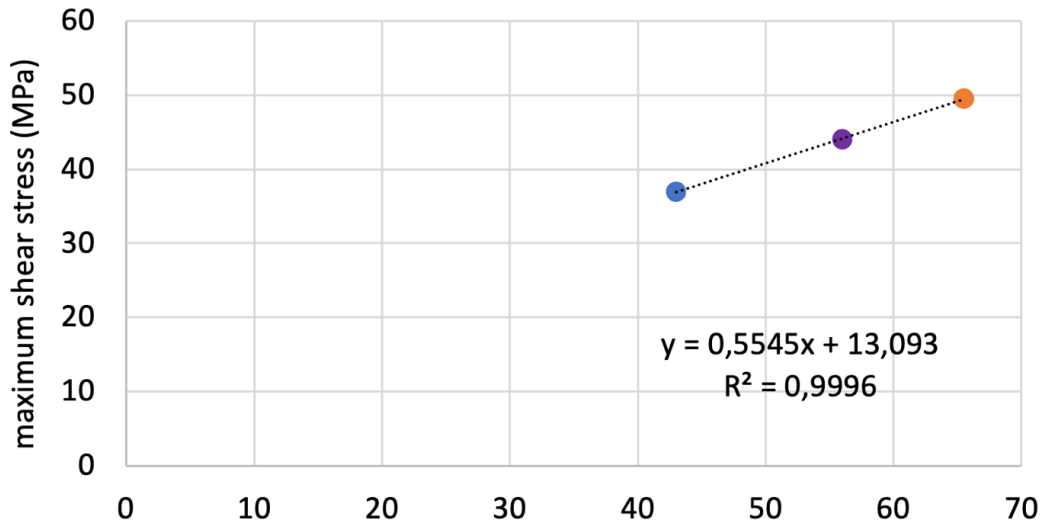


Figure 68: Calculated fracture line and statistical parameters of the rock strength.

Table 17: Results of the rock mass strength in tabular form

		standard error
cohesion (MPa)	15,7	0,77
friction angle (°)	33,7	0,78
σ_{ci} (MPa)	53,1	
m_i	8,1	

3.2.9.2. Residual rock strength

Table 18: The values used to calculate the residual rock strength.

σ_3' [MPa]	σ_1' [MPa]
8	61
12	72
17	98
38	152
26	132

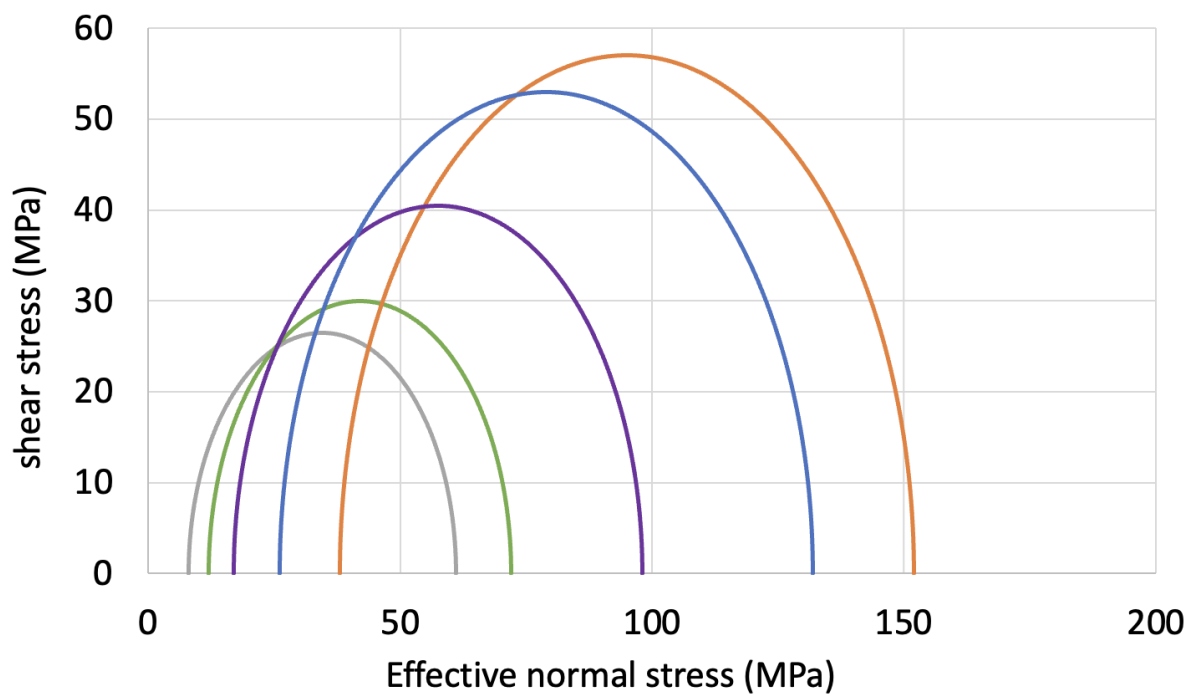


Figure 69: Graphical representation of the stress ratios according to Mohr-Coulomb for the residual rock strength.

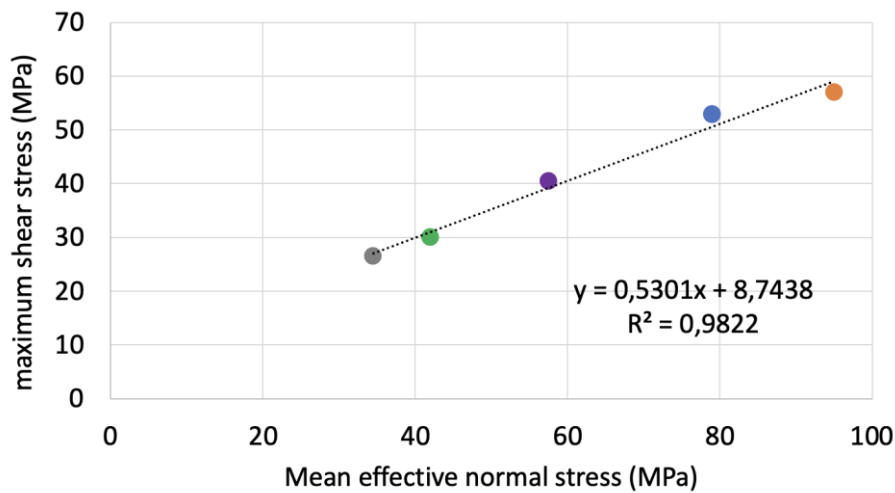


Figure 70: Calculated fracture line and statistical parameters of the residual rock strength.

Table 19: Results of the residual rock mass strength in tabular form.

		standard error
cohesion (MPa)	10,3	3,21
friction angle (°)	32,0	2,83
σ_{ci} (MPa)	5,1	
m_i	71,9	

3.2.10. Point-Load test

The results of the point load test are separated according to their orientation. An average result was determined for the valid fracture patterns (Table 20, Table 21, Table 22). Furthermore, an orientation factor that reflects the difference between the tests was calculated.

3.2.10.1. Axial Point-Load Test

Table 20: This table shows the results of the axial point load test.

sample	F_{max} [kN]	A [mm ²]	I_s [Mpa]	$I_{s(50)}$ [Mpa]	valid failure [yes/no]	h/d	valid h/d [yes/no]
PS VI 2.2	4,03	699,58	5,76	4,33	no	0,85	yes
PS VI 2.1	2,88	745,20	3,86	2,94	no	0,91	yes
PS VI 1.2	2,01	804,06	2,50	1,94	no	0,99	yes
PS II 3	1,78	574,20	3,10	2,23	yes	0,71	yes
PS II 2	2,79	787,22	3,54	2,73	yes	0,97	yes
PS II 1	2,88	713,11	4,04	3,05	yes	0,87	yes

Valid $I_{s(50)}$ average: 2,67 MPa

Table 21: This table shows the results of the axial point load test conducted with the halves from the diametral point load test.

sample	F_{max} [kN]	A [mm ²]	I_s [Mpa]	$I_{s(50)}$ [Mpa]	valid failure [yes/no]	h/d	valid h/d [yes/no]
PS III 1 (half 1)	2,47	463,41	5,33	3,65	yes	0,57	yes
PS III 2 (half 1)	2,67	351,53	7,60	4,88	yes	0,43	yes
PS I 1 (half 1)	2,19	587,32	3,73	2,69	yes	0,71	yes
PS I 2 (half 1)	3,19	664,35	4,80	3,56	yes	0,81	yes
PS III 1 (half 2)	2,47	452,55	5,46	3,72	yes	0,55	yes

PS III 2 (half 2)	5,38	559,25	9,62	6,87	yes	0,69	yes
PS I 1 (half 2)	0,72	581,01	1,24	0,89	no	0,70	yes
PS I 2 (half 2)	2,59	437,54	5,92	4,00	yes	0,53	yes

Valid $I_{s(50)}$ average half 1: 3,70 MPa

Valid $I_{s(50)}$ average half 2: 4,86 MPa

Total axial valid $I_{s(50)}$ average (10 results): 3,74 MPa

3.2.10.2. Diametral Point-Load test

Table 22: This table shows the results of the diametral point load test.

sample	F_{max} [kN]	A [mm ²]	I_s [Mpa]	$I_{s(50)}$ [Mpa]	valid failure [yes/no]	d/h	valid d/h [yes/no]
PS III 1	0,66	641,08	1,03	0,76	yes	0,89	Yes
PS III 2	1,75	639,43	2,74	2,01	yes	0,87	Yes
PS I 1	1,12	647,83	1,73	1,28	yes	0,71	Yes
PS I 2	1,52	647,38	2,35	1,73	yes	0,75	Yes

Valid $I_{s(50)}$ average: 1,45 MPa

An orientation factor of 2,58 results from the comparison of the values with and perpendicular to the schistosity.

4. Discussion

4.1. Geophysical interpretation

4.1.1. ERT

4.1.1.1. 2D ERT

As determined in the conductivity measurements, the dry rock has no measurable conductivity. Conductivity is caused by the presence of water in pore spaces and fractures in the rock. Consequently, zones of low resistance are very permeable to water and indicate high porosity or faults, while high resistance indicates solid, less fractured rock. The pole-dipole measurement is characterized by its greater penetration depth and the sharper representation of structures. Unfortunately, the last section of this measurement had to be discarded due to technical errors.

It can be clearly seen that the area under the invert has low electrical resistance. This low resistance extends over the entire profile and is not visible before the start of the steel arch section. This can be explained by the different type of lining in this area. The masonry hardly lets pass any water, and the much stiffer lining prevents cracking in the invert, which leads to increased water movement.

In the steel arch section, a significantly lower resistance can be seen in the first few meters beneath the invert. In the first half in particular, this extends to a depth of around six meters, while in the second half it is around four meters deep. In between, around sixteen meters into the steel arch section, there is a zone of higher resistance with a length of eight meters. There are several sections of high resistance at the invert, especially in the first thirty meters of the steel arch section. This can be explained by local dry spots, as ground water is only present from a depth of around thirty cm.

The evaluation of the results from the Wenner- α setup shows very similar results to the pole-dipole inversion. The same structures are recognizable, but slightly less sharp. The data in front of the face show a rather deep area with little resistance and at the same time an area with high resistance around meter 38. On closer inspection this ranges from meter 34 to 45 and is comparable with the values between meter 10 to 22. It is possible that this indicates the same structure, an area with comparably less pore space.

When combining both methods the same structures can be found with slightly different intensities. Really remarkable are the clearly visible structures with low resistance, which dip at around 25 to 40 degrees in the direction of the face. They are interrupted by a similar oriented area of higher conductivity. There is no reason to assume that the damaged zone with the same rock mass gives such clearly different results. Rather, a lithologically weakened, highly permeable zone can be assumed. The most obvious assumption would be the presence of two faults that cross the tunnel and are interrupted by an unfaulted zone. This would better explain the areas of higher resistance on the surface than the hanging wall of the faults, which experiences more pressure or compression and therefore has less pore space. From that point the transition to the areas with low resistance is very rapid, whereas it is more gradual in the lying wall of the fault. This could give an indication of the prevailing stress conditions.

4.1.1.2. 3D ERT

The sections through the 3D ERT tomography show comparatively high resistances directly below the surface. This is due to the fact that the area under investigation is located prior to the steel arch area and has presumably undergone less deformation. In addition less water reaches the invert, which results in less weathering. The X-Z cross-section shows a steeply standing zone with reduced resistance. This can also be seen on the X-Y cross section where it crosses the array. It could be a small fault or large cleavage that carries more water than the surrounding rock. The structure has a Clar value of (200/75), assuming a planar extent. However, it could also be a very localized phenomenon caused for example by the different compaction of the soil during construction.

4.1.2. Seismic

The seismic tomogram shows velocities of around 1800 m/s to over 5000 m/s. As expected, the velocity increases at greater depths, where the rock is more compact. Compared to the laboratory results of around 4000 m/s, there is also a significant drop, which is to be expected due to the loosening of the rock in the ground. The areas with low velocity are of particular interest. There, the individual rock fragments have particularly poor contact with each other. This suggests severe weathering and/or a structure with these characteristics, such as a fault. But because the beginning of the profile does not contain many data points, the result should be viewed with a certain degree of caution. Nevertheless there is an area of very low velocity, that indicates a loosening. This could be a fault, but the junction with the small tunnel to the

shaft is located here and therefore the cross-section is significantly larger. This could have led to loosening in the invert.

Around eight meters into the steel arch section there is another zone of low velocity. This could also indicate a fault. From about 20 to 34 meters into the steel arch section a massive anomaly occurs. This is represented by a zone of massive loosening that can basically only be caused by a large fault. As the results directly below the low velocity are very high, it can be assumed that the fault dips in the direction of the tunnel face at around 45 degrees, assuming that it strikes at right angle to the tunnel.

The last 15 meters ahead of the tunnel face are characterized by a comparatively compact subsurface. The supporting effect of the tunnel face could come into play here, although it should be noted that there are significantly fewer data points at the end of the profile.

Overall, a general dip of the layers towards the face can be recognized, but it is not pronounced enough to have a high confidence.

4.2. Deformation interpretation

The deformation of the steel arches and their evaluation is one of the key issues in this work. As already mentioned in the methods it is assumed that the arches were in perfect and symmetrical shape when they were constructed. Even if the deformation of the rock will never completely disappear, it is reasonable to assume that they have already reached their final state for the evaluation.

The diagram (Figure 50) clearly shows that the deformation on the left wall and at the top is generally more severe than on the right wall. A similar development can also be observed between the crown and the left wall. This is also due to the fact that the main deformation occurs in the area of the shoulder, which affects both sections in the assessment.

The areas around arches 28 and 68 are particularly noticeable, where the arches in the crown area have been severely deformed and are largely broken. From a geological point of view, a fault zone could be suspected here, which is noticeable in the rock by a significantly reduced shear strength.

A weaker and cyclic increase in deformation can also be observed on the left wall. This is not as pronounced as with the area of the faults and could indicate a regular bedding of the rock,

which has a thickness of around five meters. However, the possibility of additional lining or repairs, which are no longer visible, should not be neglected here.

Towards the end of the tunnel there is a clear drop in deformation. This can be explained by the fact that the face takes on the load and therefore the lining is less stressed. This effect usually extends to about two to three tunnel diameters into the cavity, which is around arch number 85. This is also reinforced by the smaller cross-section in the last few meters of the tunnel. The fact that the deformation is still present on the left wall indicates stress from this direction, which does not exist to the same extent at the crown and on the right wall.

A detailed look at the fault areas reveals that the maximum deformation begins at the left knee and is visible in the crown area a few arches later. About ten arches later the deformation is visible on the right wall.

Arches 60 and 61 show slight deformation at the left knee (Figure 71). A small bulge can be seen, which however can not become more pronounced, because the arches are embedded in the ground. At arches 61 and 62, this deformation is clearly visible at the springline.

Finally, arch 63 is the first one to break in the crown area. However, this is not due to stress in the crown, but due to high tension in the shoulder area. Here the arch is pressed into the cavity and is clearly deformed. The fact that it is bolted to the lower element also contributes to this. Due to the deformation, the I-beam is compressed in the lower half and stretched in the upper part, which exceeded the tensile strength of the arch and led to a break at the point of highest bending moment in the crown. In arches 66 and 67 it can be seen that the load occurs less in the area of the left shoulder, but the arch is loaded mostly from above. In arches 70 and 71, the deformation in the right shoulder becomes clearly visible. In arches 75 and 76, it finally reaches the right knee area. Based on the assumption that the areas of strong deformation are caused by a fault, the Clar value of the fault can be determined from the observations.

The strike results trigonometrically from a tunnel width of 3.5 m and a length of 15 arches, which is 7.5 m in 65 degrees to the tunnel axis. The dip is calculated in the same way and is 65 degrees but has a higher error due to the poorer observability at the crown. As the Clar value of the gallery is 150 degrees, the absolute orientation for the fault is (175/65).

The decrease in deformation in front of the potential fault areas is also very noticeable. Around arches 16 and 58 in particular, almost no deformation can be observed. This is located a few meters before a massive increase in deformation in the wall and crown. This aspect also fits into the picture of the calculated fault. In this weak zone, a large part of the deformation is absorbed and in the hanging part it does not or only barely occurs. The fault lies like a protective screen over the area.



Figure 71: Detailed picture of the arches 60 to 70.

4.3. Sample interpretation

4.3.1. Water content

The average water content of the deep samples is 10.1 percent, while that of the shallow samples is around half (5.15 percent). The deep samples were all saturated with water, which is clearly reflected in the results.

The surface samples show a clear trend of decreasing water content with distance from the face. These results correspond to the situation on site, which is characterized by standing water at the face. Sample 2b is an exception here, as it is part of the material deposited at the side and is slightly elevated, which is reflected in a significantly lower water content.

4.3.2. Sieving

The comparison of the sieve lines reveals interesting aspects. A clear trend of the samples distant to the face can also be seen here. It is particularly noticeable that the sample with the lowest fine grain content is sample 5o (Figure 72). Only at this sample point it was possible to take solid samples at a greater depth. Aside from this sample point, the deeper sample was generally also the finer sample.

This result suggests that the rock further down in the tunnel has been exposed to more weathering, mechanical disturbance from construction equipment or possibly more tectonic stress, which led to finer fractures. This might accelerate weathering, especially in the water-saturated zone.

The result of sample 2t should be treated with a certain degree of caution. This sample was very fine and cemented during drying, which made it necessary to mechanically loosen the aggregates that formed. It can therefore be assumed that the sample was very fine, but not quite as fine as the results suggest.

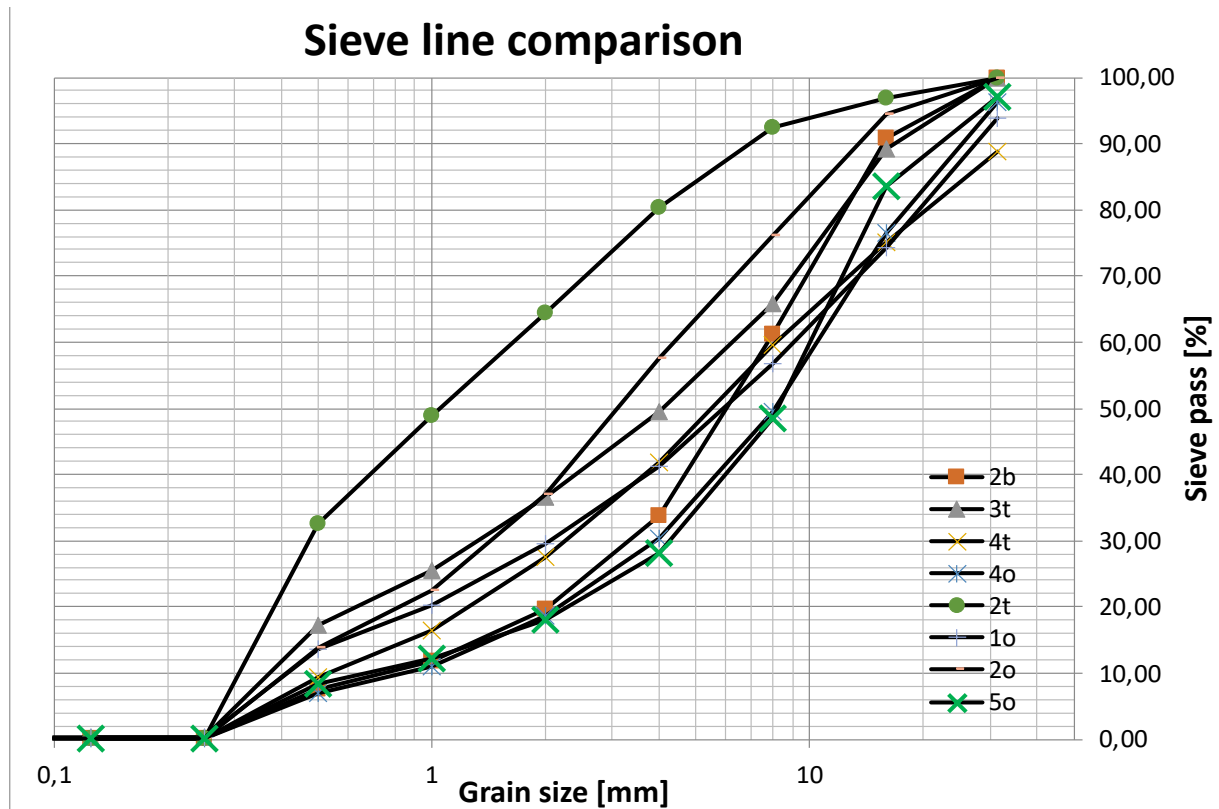


Figure 72: Combination of all eight grading curves. On the x-axis the grain size in mm is shown and on the y-axis the sieve pass in percent. The various curves are identified by symbols, which can be seen in the legend.

4.3.3. Porosity

The results of the helium pycnometer proved to be unreliable and not suitable for the samples used in this study.

On the one hand many of the samples did not have a perfect cylindrical shape, and on the other hand the pore spaces are very small. This led to results ranging from -0.36 % to 6.64 % when calculating the porosities. Ideally cylindrical samples therefore produce a negative result, while flawed samples produce a significant overestimation. This method is therefore not suitable for determining porosity in the circumstances of this project. The results will be dismissed.

The results of buoyancy weighing, and the associated porosity determination were much more consistent. The results lay between 0.99 percent and 1.86 percent with an average value of 1.53 percent. This method is well suited to the samples of this project. With the results, a very low pore volume could already be assumed macroscopically. The results support this assumption. Nevertheless, the values are higher than expected for a solid rock, which indicates microfractures due to a high stress level. This result is, however, consistent with the fact that the tunnel is almost 70 years old and has no lining at the invert. A certain uplift and associated loosening are to be expected.

4.3.4. Ultrasonic velocity

The results of the P-wave velocity give an average of 3737 m/s for the dry samples and 3919 m/s for the saturated samples. If particularly low results below 3600 m/s and the PS V sample are deleted, the difference is only 4 m/s (3951 m/s dry; 3947 m/s saturated), which is statistically irrelevant. The low measurement results were due to the non-planar surfaces of the samples. Therefore, the contact area was reduced, and no significant result could be recorded. Sample PS V consists largely of quartz and is not considered representative.

4.3.5. CAI

The results of the CAI show clear differences in terms of orientation. There was almost no abrasion in the lines with the schistosity. The result is extremely low with a CAI of 0.35. Even this value is likely to overestimate reality slightly, as the magnification used makes it very difficult to measure abrasion at this level of detail. There were also tips that did not show any clear abrasion, but a measurement is necessary for automatic evaluation. It can be assumed that

the actual value is around 0.25. Against the schistosity, the result was significantly higher at 1.19, but the material can still be described as quite soft and nonabrasive.

The large difference in direction can be explained by the presence of small quartz layers in the schistosity, which are highly abrasive. While the tip was able to create a ridge between these in the experiments parallel to the schistosity, it had to overcome them perpendicular to the schistosity. This was also felt subjectively during the experiment itself, as the tip seemed to get stuck again and required more force to move it further. After the tip was able to penetrate very deep quickly, it was then stuck in front of a solid obstacle. This also explains why many tips were not abraded evenly against the schistosity but were also bent.

4.3.6. Brazilian test

The results of the Brazilian test show large differences. With only five tests and values between 6.74 and 47.73 MPa for the tensile strength, no reliable prediction can be made for the strength of the rock.

Assuming that samples PS IV and PS V do not represent the rock mass, as they were the only 100 mm drill cores that could be recovered, and further assuming an error in the measurement of sample PS II 1 (grün), two samples remain within a realistic value range of 7 - 10 MPa for the intact rock. This range can be taken as a reference point with low confidence.

4.3.7. Triaxial test

All triaxial tests went well and without any problems in the test execution or the premature failure of the sample. Nevertheless, it must be mentioned that only three samples suitable for testing could be prepared for this test. For this reason alone, it can be assumed that the tested samples have higher strength than the typical rock, thus providing an upper boundary for the strength.

The tests show that the rock experiences a strong increase in strength when it is confined. The only sample that suffered a massive fracture was the least confined sample PSI_3. It fractured at around 80 MPa σ_1 and a little later a second time.

Sample PSVI_4 broke several times, but never completely and steadily gained strength with increasing confinement.

The same was seen with sample PSVI_3, which was tested up to a maximum σ_1 180 MPa. These tests show that the samples retain a significant residual strength.

In contrast, it became evident during the sampling and drilling of the cores that the strength is not very high due to the existing schistosity and the associated smooth flat surfaces, which create weak zones. At high confining pressure this effect no longer plays a significant role, because the microcracks along the schistosity are closed.

The rock strength results in a low peak cohesion of 15.7 MPa and a friction angle of 33.7 degrees. The uniaxial compression strength (UCS) is calculated as 53.1 MPa and the m_i at 8.1. These values are low for a crystalline rock mass but would fit well with a schist. However, it should be mentioned that the samples were taken from the damaged zone of the tunnel and therefore a lower strength than in the intact rock is to be expected.

The residual cohesion is 10.3 MPa at a friction angle of 32 degrees, which indicates that the rock still has a significant degree of strength after the first fracture. In particular, the m_i of 71.9 is extremely high and clearly indicates that the strength of the rock increases significantly with confinement.

4.3.8. Point load test

A total of 10 valid axial point load tests and four diametral point load tests were carried out. In the vast majority of these tests, the failures were not very explosive, but rather the samples just fell apart. This behavior shows that the samples cannot withstand high stresses, but rather fail at lower ones. As also observed in the triaxial tests, the samples retain a high degree of residual strength even after breaking.

With an IS_{50} of 3.74 MPa perpendicular to the schistosity, the material is not particularly strong. In the direction of the schistosity, the IS_{50} is only 1.45 MPa. This means that there is a factor of 2.58 between the directions, which is a very clear indication of strength anisotropy. Dividing the UCS by the IS_{50} gives the c-value, which is used to correlate the point load test to the UCS. In this work, it is 14.2, which is slightly lower than the average value in shales. However, as the samples for the point load test were not as stable as the samples used for the triaxial test, it can be assumed that the c-value is more likely to be in an average range of around 20 if the sample quality is similar.

4.4. Comparison with Schünemann (2023)

The work of Schünemann (2023) serves as an essential comparison for the results of this thesis. Most of her samples were not taken in the steel arch area, but in adjacent areas of the tunnel system. There however, it was possible to take much more substantial samples and produce more robust results. A comparison is particularly interesting with regards to the c-value between

the UCS and the point load test, as it is hardly possible to take consistently large samples in the steel arch area.

In detail, the results of Schünemann's Sample Campaign II are compared with those of this thesis. Sample 1 (Cave) is the closest sample to the steel arch area. Sample 5 serves as a further comparison for the rock strength.

It should be noted that Schünemann used drill cores with a diameter of 50 mm for her tests. It must therefore be assumed that the sample material was of better quality than that used in this work. This is also reflected in the comparison of the basic rock properties (Table 23). While the grain density is the same at 2.8 g/cm³, Schünemann's porosity is about 1.2 %, whereas it averages 1.55 % in this work. This also results in a lower bulk density and a lower p-wave velocity. Overall, the material appears to be very comparable. It should only be noted that the samples in this work seem to be of poorer quality, which means that they have undergone more weathering or damage.

Table 23: Basic rock properties of Schünemanns (2023) sample campaign II.

Sample	Bulk density [g/cm ³]	m_{dry} [g]	Grain density (Archimedes) [g/cm ³]	Porosity [%]	v_p [m/s]
1 (Cave)	2.77	486.49	2.81	1.27	4928
2	2.77	489.37	2.80	1.12	4803
3	2.74	497.63	2.77	0.96	4851
5	2.76	461.21	2.79	1.16	4611

With an I_{s50} of 3.87 to 3.74 MPa, the results of the point load test are very comparable, as Schünemann also collected her samples in the steel arch area. There are major differences in the determination of the UCS, with an average of x MPa for sample 1 and y MPa for sample 5. While there is very little data available for this in this work, Schünemann conducted significantly more tests and also carried out direct UCS experiments. Therefore, her results can be considered more reliable, although it should be noted that her samples withstood the extraction of a larger drill core diameter (50 mm), which in itself introduces a bias towards more competent rock. This results in a c-value of 12.4 - 28.8, which is on average higher compared to this work (14.2).

On the other hand, Schünemann also determined a UCS of 50 MPa from the triaxial tests of sample campaign II, which corresponds to the derived UCS of this work. It is therefore reasonable to assume that the c-value is not drastically different, but that the determination of the UCS using a triaxial test may underestimate the UCS for the material investigated. As already mentioned in the discussion of the triaxial test, the material reacts rather atypically and gains a great deal of strength with increasing confinement. The subjective selection of the "better" samples could also play a decisive role here. While the drill cores can only be obtained from the best sample material, the requirements for the point load test are quite low. Therefore, it can be difficult to compare equivalent sample material, especially in the presence of such weathered and damaged material.

4.5. Correlation and outlook

The correlation of the geophysical results shows a high degree of similarity between ERT and seismic tomography (Figure 73). The same structures are clearly visible in both tomograms. In particular, the areas in which the rock is looser and those in which it is more compact match superbly. Thus, up to four faults can be identified, that are divided into two larger areas. There is no conclusive for the exact structural geology, but from a geotechnical point of view, these are heavily damaged areas.

The laboratory results fit the field results, but they reflect the intact rock rather than the entire rock mass. The connection between the geophysical results and the observation of the deformation shows great similarities, but also differences. These can be explained on the one hand by the way the information is obtained, but also by the fact that the deformation is visible above the invert and the geophysics provide results below the invert. This makes an exact correlation of individual structures difficult. Nevertheless, it can be stated that in the areas where the deformation indicates faults, clearly loosened zones can also be seen in the tomograms, although with a slight offset.

2D ERT

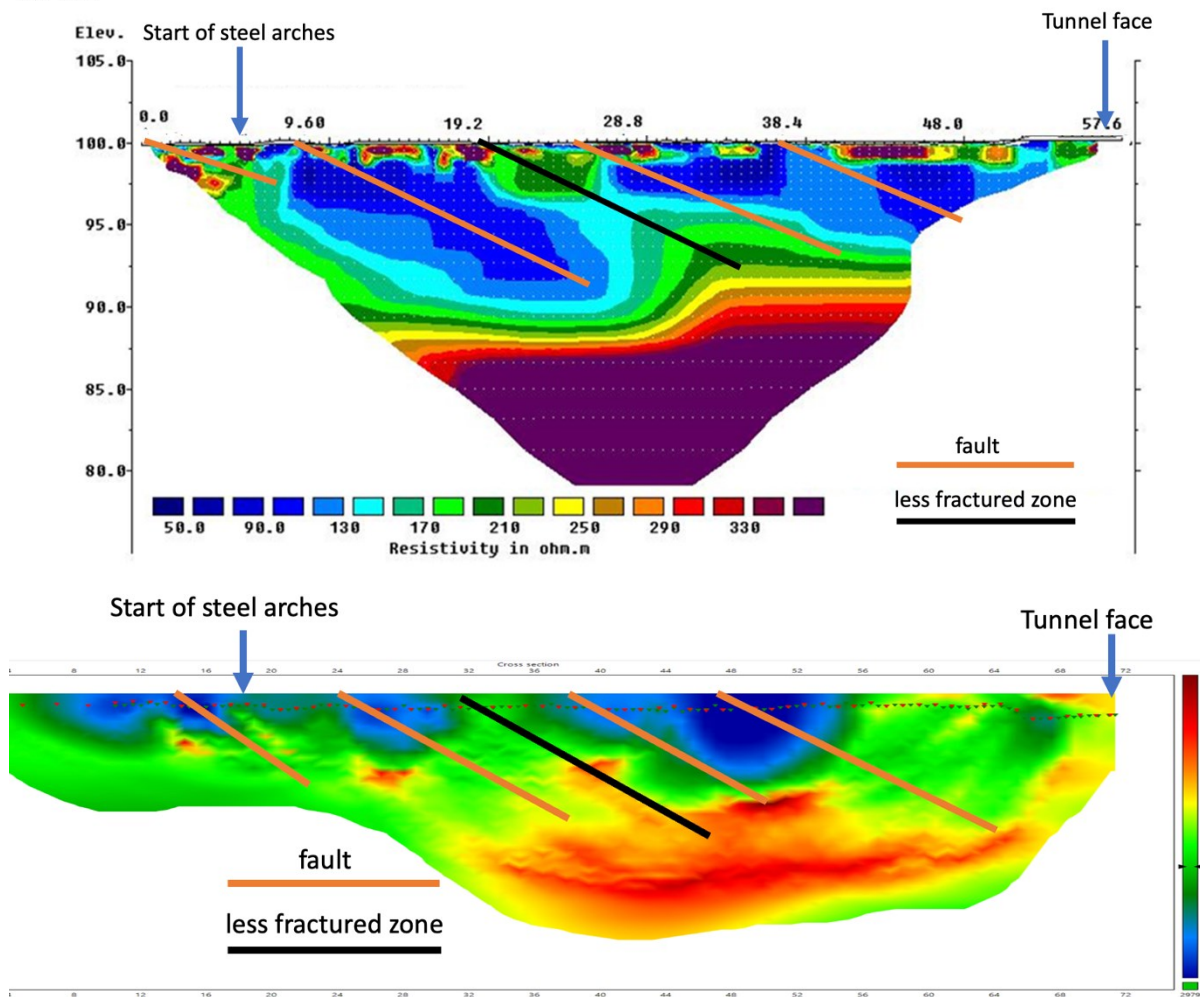


Figure 73: The figure shows the correlation of the 2D tomograms from seismic (lower part) and ERT (upper part). Faults are shown in orange. More compact zones are shown in black. The x-axis is given in meters.

A further and more detailed investigation of the fault zones could provide interesting insights into the correlation between geophysics, deformation, and the associated structures. A 3D ERT of the fault zone in the area of the steel arches 60-70 and a quantitative recording of the deformation using, for example, a LIDAR scan of the support elements could lead to more details.

The design and construction of a compressed air storage in such difficult conditions with faults and a quite deep damaged zone is certainly possible, but the results of this work show that the geotechnical parameters for such a project are not good. Unless the aim is to implement the idea in such challenging conditions, another location would certainly be preferable. Nevertheless, there is great potential for research and new scientific findings in this area.

5. Conclusion

At the start of the study, the focus was set on determining the geotechnical parameters in the steel arch section to answer which challenges the planning and construction of a compressed air storage has to overcome. In the course of the study, the correlation of the different methods became more and more important and thus an essential part of this work.

The visible rock mass is clearly weathered at the invert and occurs as loose material in almost the entire steel arch section. Solid pieces of rock can be found in isolated locations at a depth of 30 cm. The examined samples had a clear schistosity and a significant strength anisotropy. The results of the CAI and the point load test in particular illustrate this very clearly. The intact strength of the material in the invert was determined by point load and triaxial tests with a UCS of around 50 MPa. The triaxial test showed that the rock gains a great deal of strength under confinement.

The geophysics show a loosened zone in the invert with a depth of around four meters, and several faults that cross the area. Furthermore, there is also clear stratification in the larger units, although no clear Q value can be assigned to this as the investigation only involved a 2D section along the tunnel.

The observation of the deformation in the steel arch area shows that the stress is particularly on the left side of the tunnel, where the deformation is clearly pronounced. Two faults can be traced that cross the tunnel obliquely and dip quite steeply. Here, quantitative methods could bring more accurate results for the interpretation.

The combination of methods, especially geophysics and deformation, show a high degree of correlation and can help to better understand the geotechnical conditions in existing tunnel systems. This is particularly interesting in areas where it is not possible to obtain conventional drill cores for analysis.

In conclusion, it can be stated that the geotechnical conditions for the construction of a compressed air storage are rather poor. The main challenges are the distinct schistosity of the rock mass and the faults cross-cutting the steel arch section. In combination with the loosened zone and the weathering, this makes a construction difficult.

6. Literature

Erhart, Kern, Schödl (1970). "Geologischer Söhligschnitt 28, Dreikönig". In: VA-Erzberg archive.

Gonzalez De Vallejo, L. and M. Ferrer (2011). Geological engineering. CRC press. ISBN: 9780415413527.

Holzer, H., Stumpfl, E.F. (1980). "Mineral Deposits of the Eastern Alps". Excursion Guide. Abhandlungen der Geologischen Bundesanstalt in Wien Vol. 34. pp. 171 – 196.

Lepique, M. (2008). "Empfehlung Nr. 10 des Arbeitskreises 3.3 "Versuchstechnik Fels" der Deutschen Gesellschaft für Geotechnik e. V.: Indirekter Zugversuch an Gesteinsproben - Spaltzugversuch". In: pp. 115–122.

Melcher, F., H. Pluch, and R. Galler (2022). "Die Sideritlagerstätte des Steirischen Erzberges". In: Rantitsch, G. a. Raith, J.G. (Eds.): PANGEO Austria 2022 - Abstracts, 10-14 September 2022, Leoben. - Berichte der Geologischen Bundesanstalt 143. pp. 211–224.

Rissler, P. (2023). Empfehlung Nr. 2 des Arbeitskreises "Versuchstechnik Fels" der Deutschen Gesellschaft für Geotechnik e. V.: Dreiaxiale Druckversuche an Gesteinsproben.

Salzer, E. (2023). „Die geschichtliche Entwicklung vom „Presserstollen““. Unpublished report.

Schünemann, V. (2023). "Development of an engineering geology model for the construction of a compressed air storage in existing disused mining galleries". Master Thesis. Technische Universität Bergakademie Freiberg, Freiberg.

Šumanovac, F., Alavanja S.D. (2007). "Determination of resolution limits of electrical tomography on the block model in a homogenous environment by means of electrical modelling". Paper. Rudarsko-geološko-naftni zbornik Vol. 19. pp. 47-56. Zagreb.

Thuro, K. (2010). "Empfehlung Nr. 5 „Punktlastversuche an Gesteinsproben“ des Arbeitskreises 3.3 „Versuchstechnik Fels“ der Deutschen Gesellschaft für Geotechnik". In: pp. 55–70.

Zabl, M. (2023). „Report of the geophysical field exercise“. Unpublished report.

7. Appendix

7.1. Appendix A: Samples

Seven images of each drill core (4x mantle; top; bottom; after experiment).

7.2. Appendix B: ERT Evaluation

Table with all ERT measurements taken. Assessment of their quality and usability.

7.3. Appendix C: Steel Arches

Images of the arches in the whole steel arch section.

7.4. Appendix D: Deformation raw data

Table showing the qualitative assessment of each steel arch.

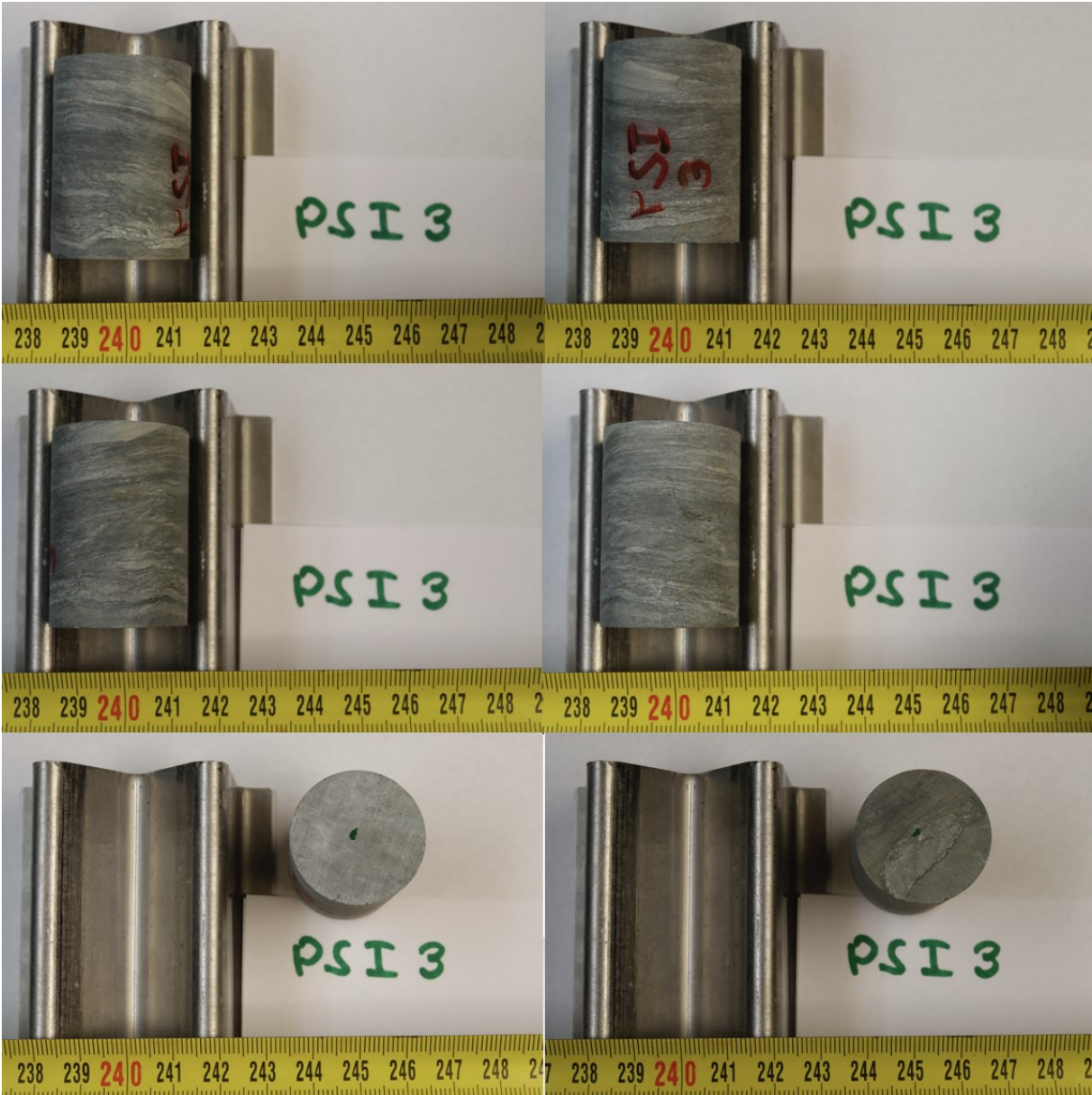
7.5. Appendix E: 3D ERT Tomography

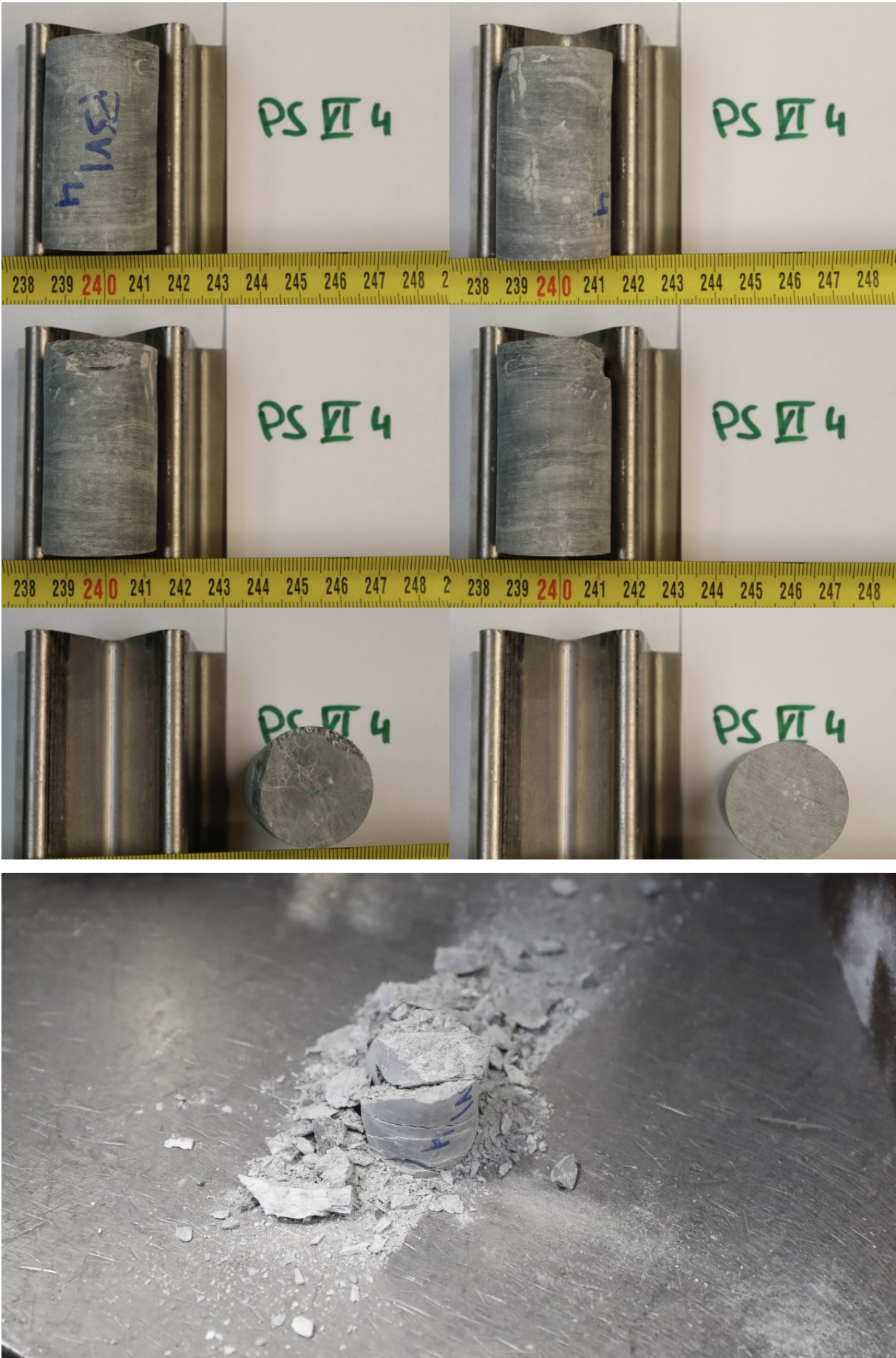
All cross-sections of the 3D ERT Tomography.

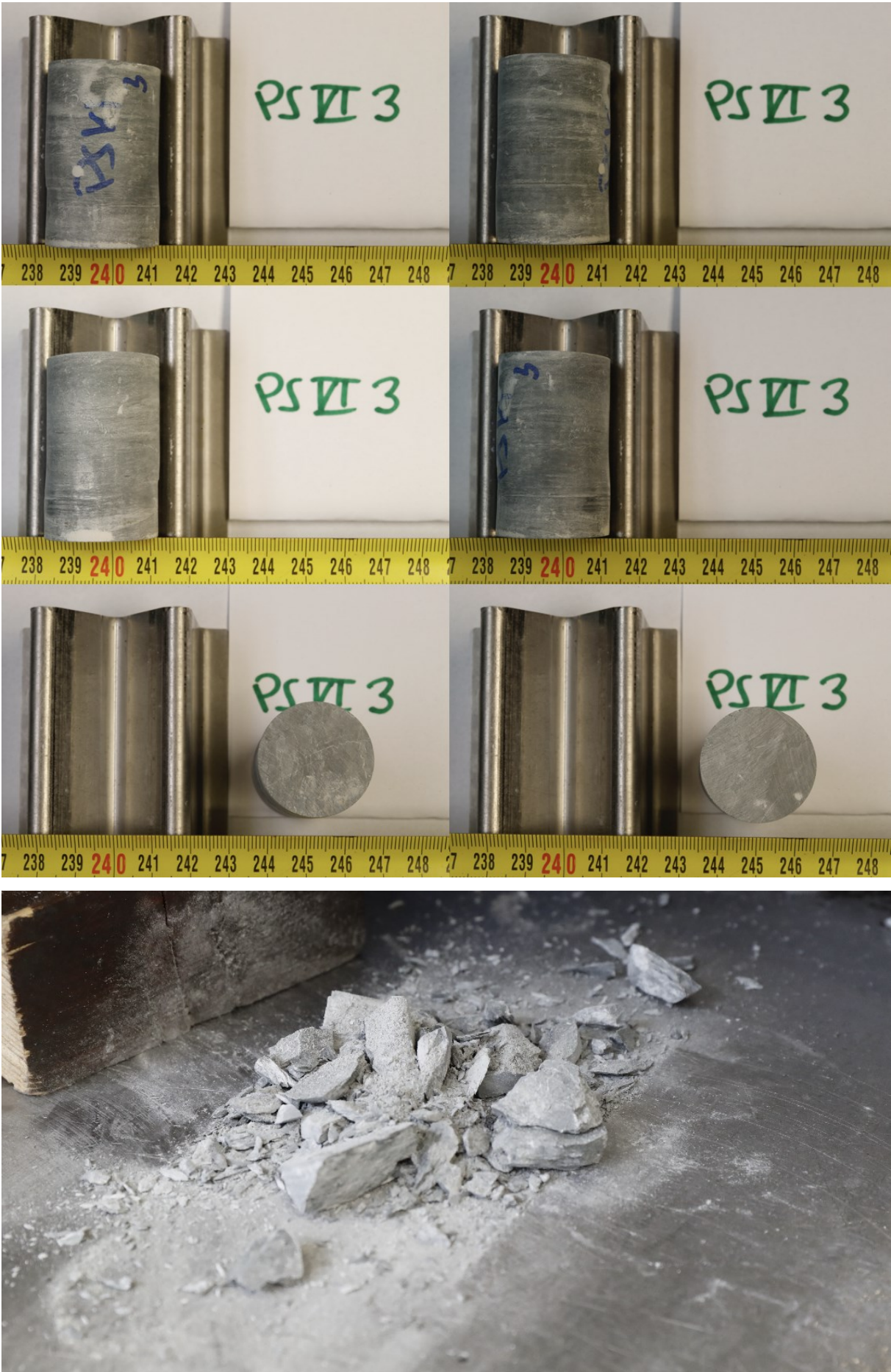
7.6. Appendix F: CAI raw data

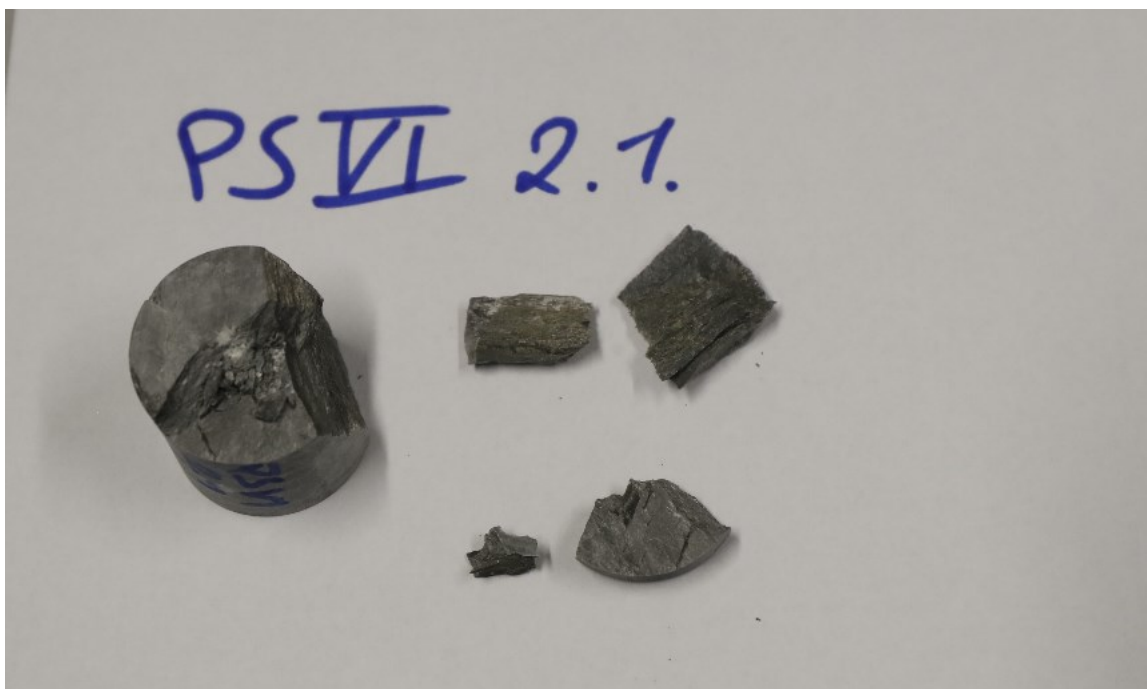
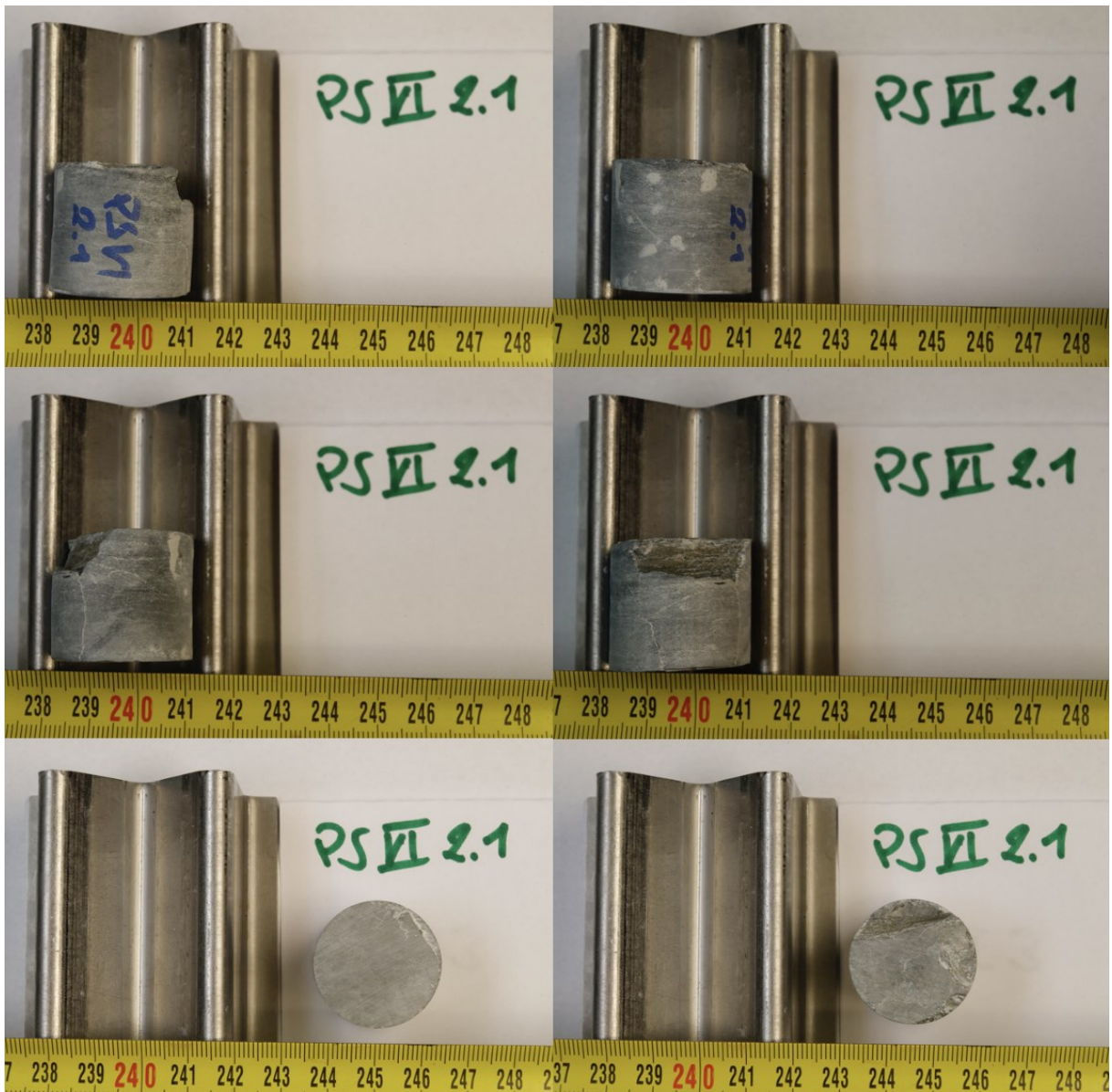
7.7. Appendix G: Sieving raw data

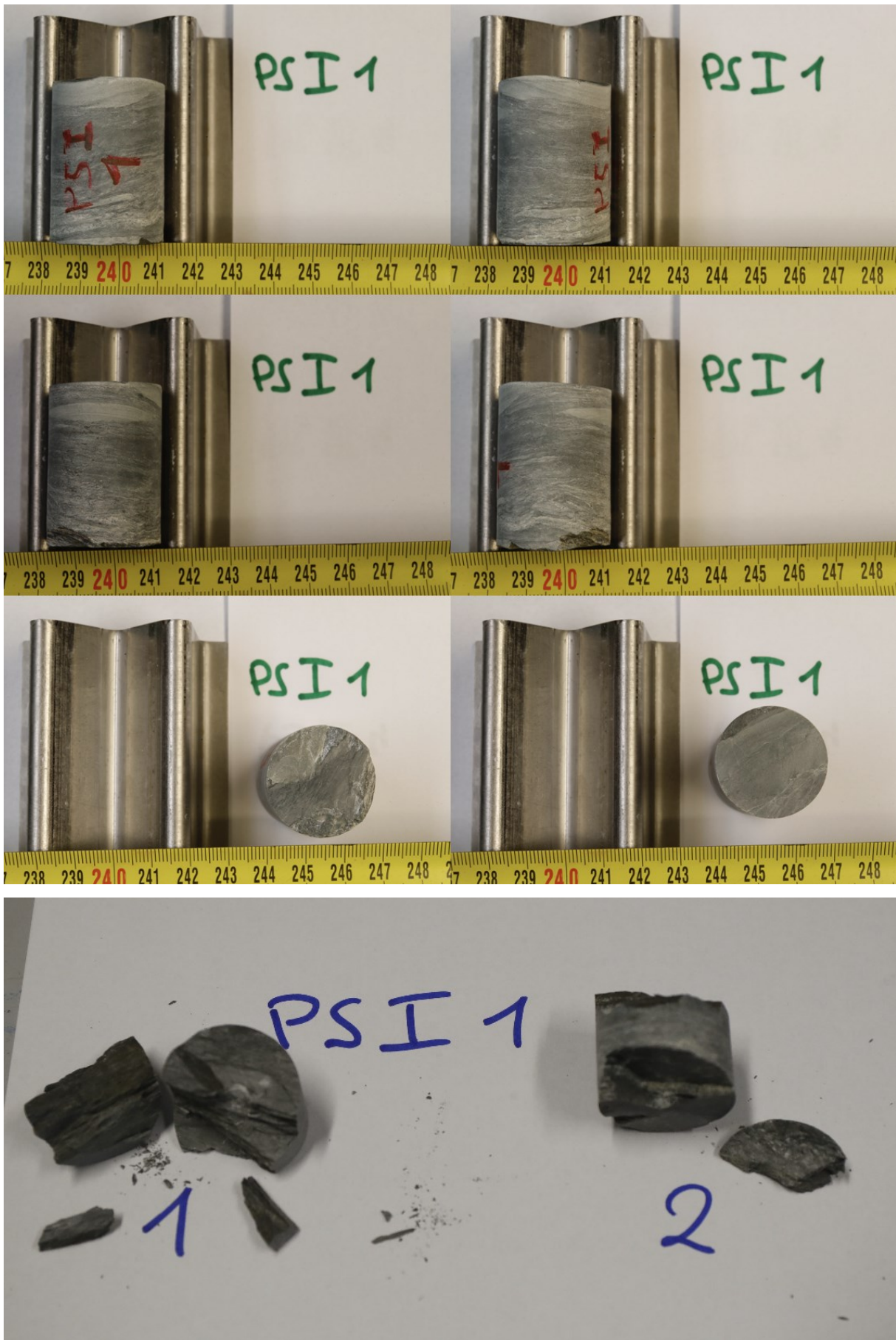
7.1. Appendix A: Samples

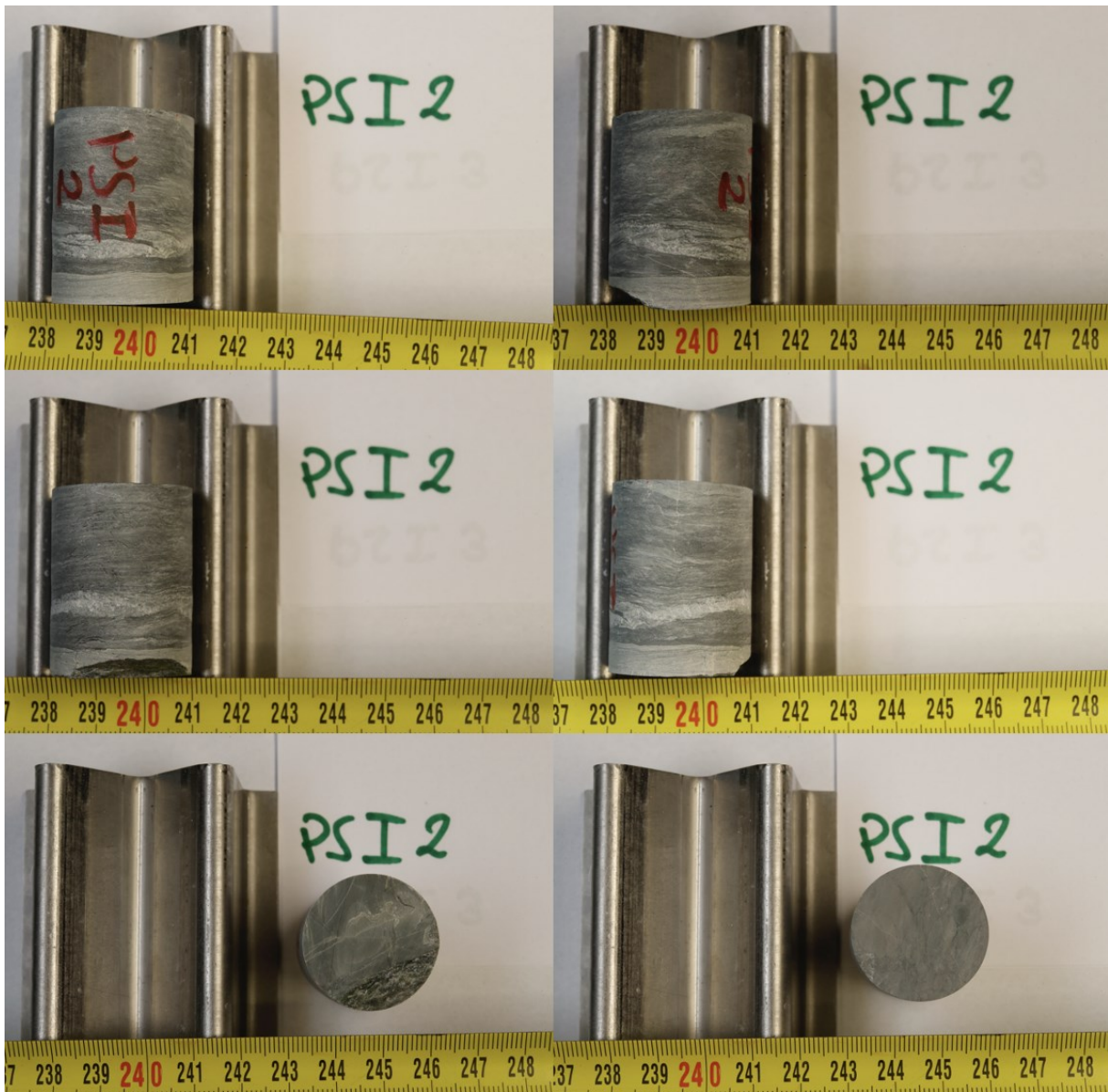


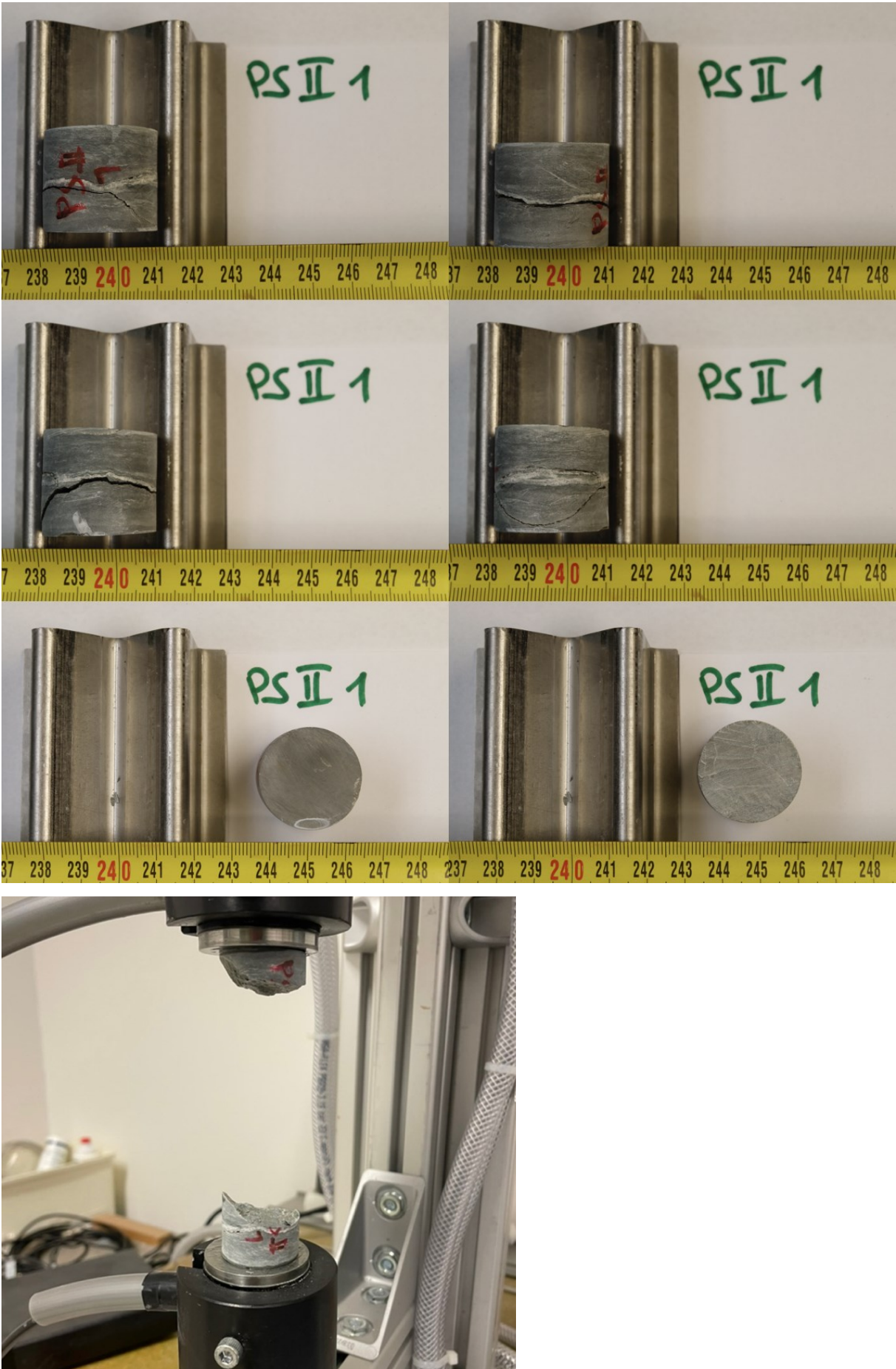


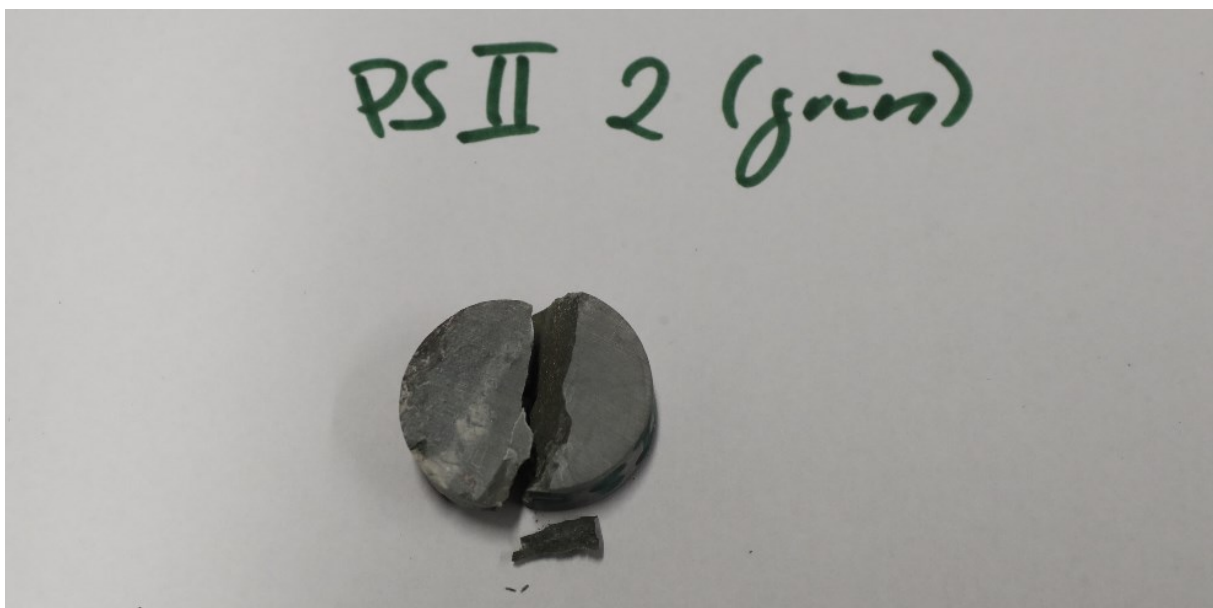
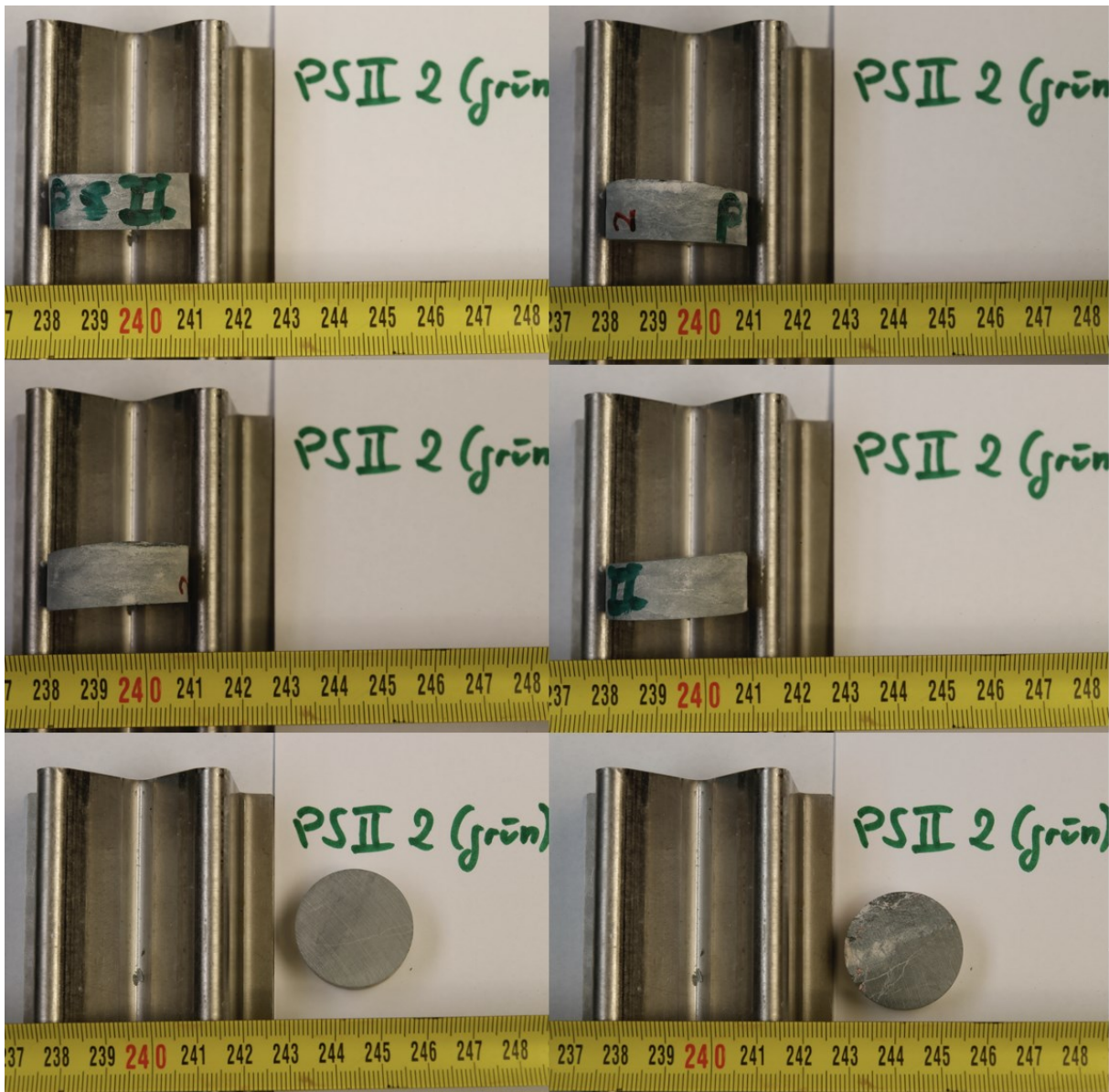


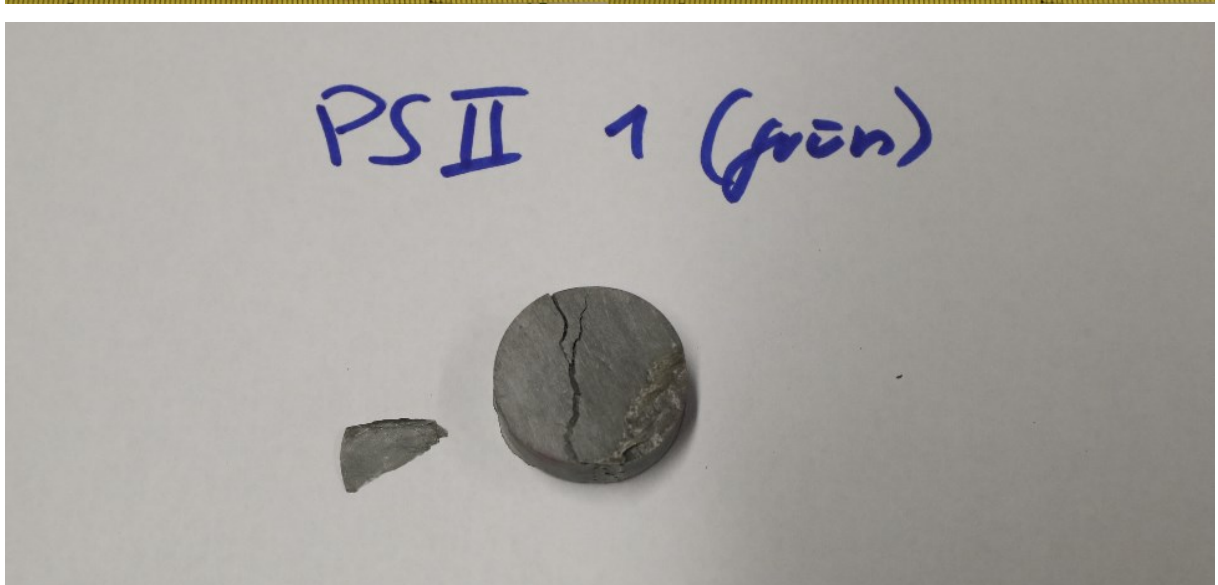
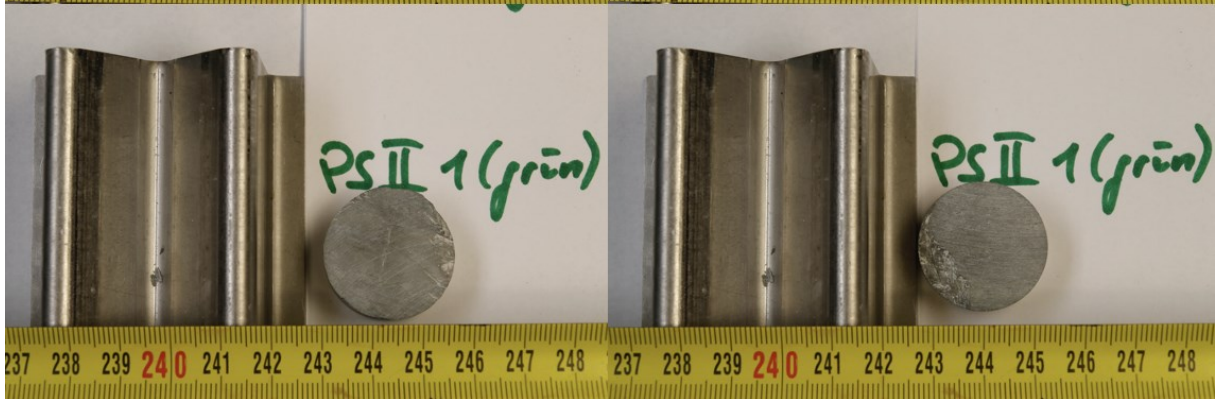
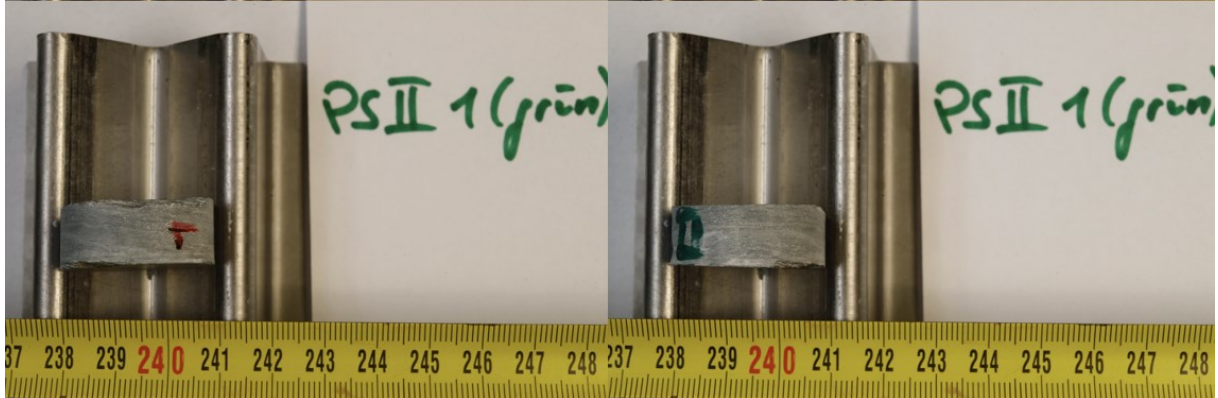
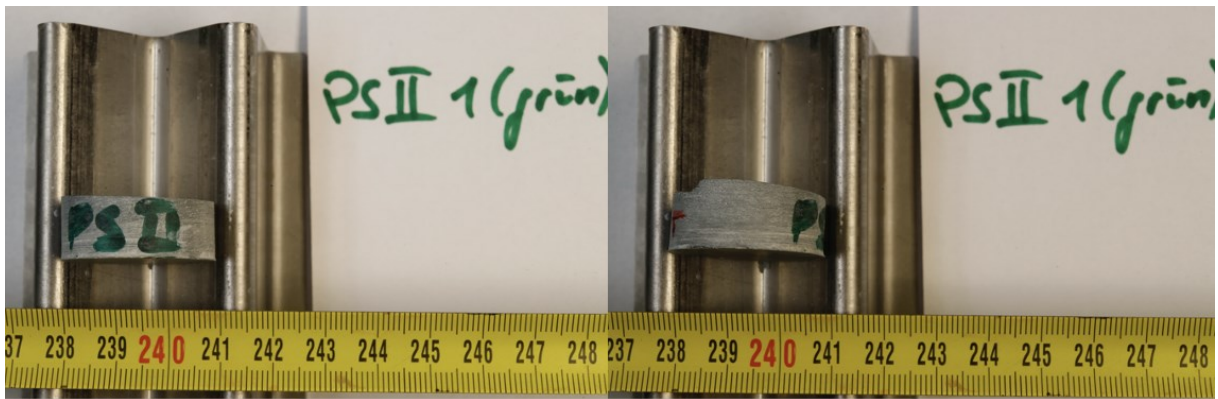


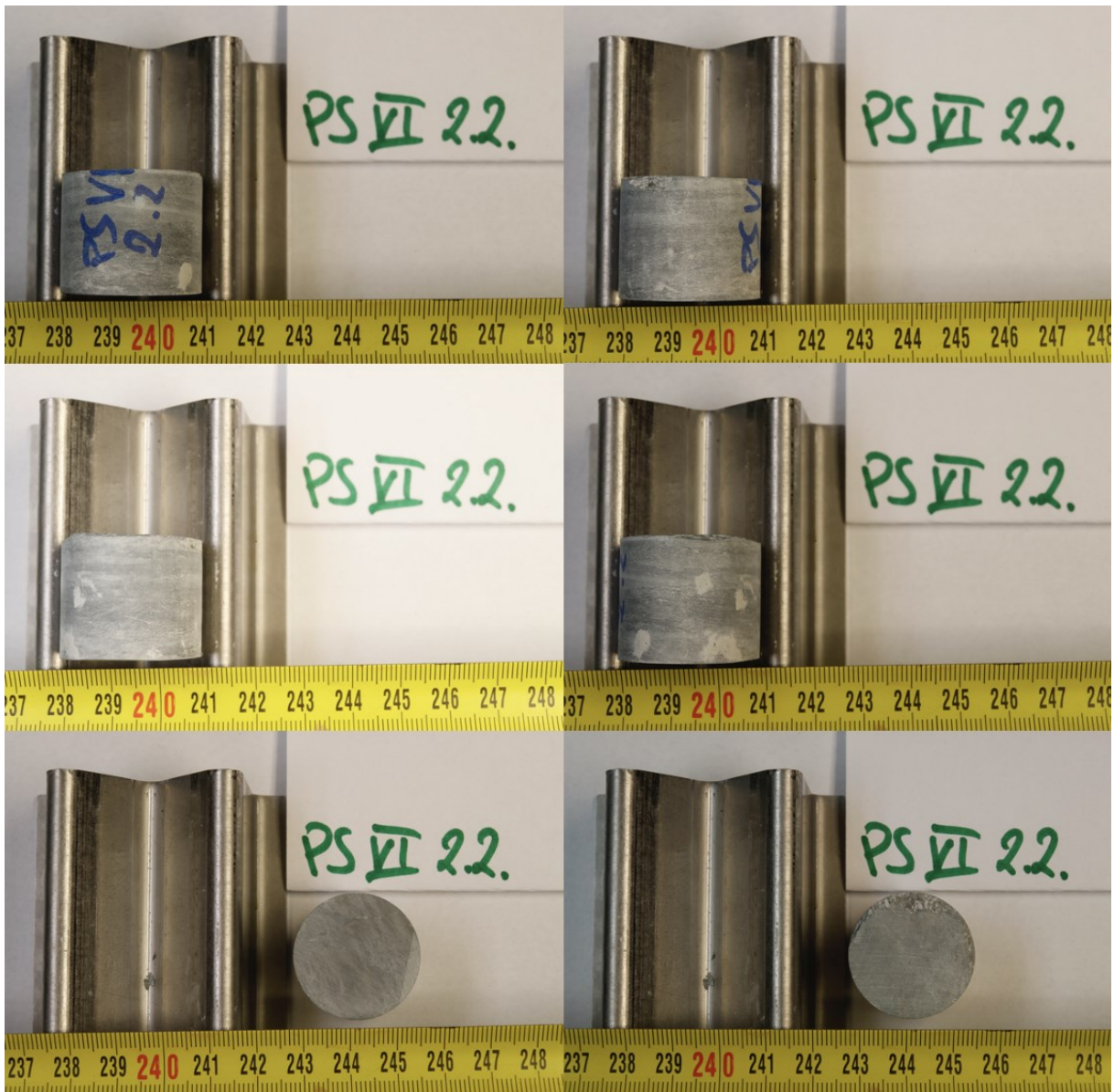


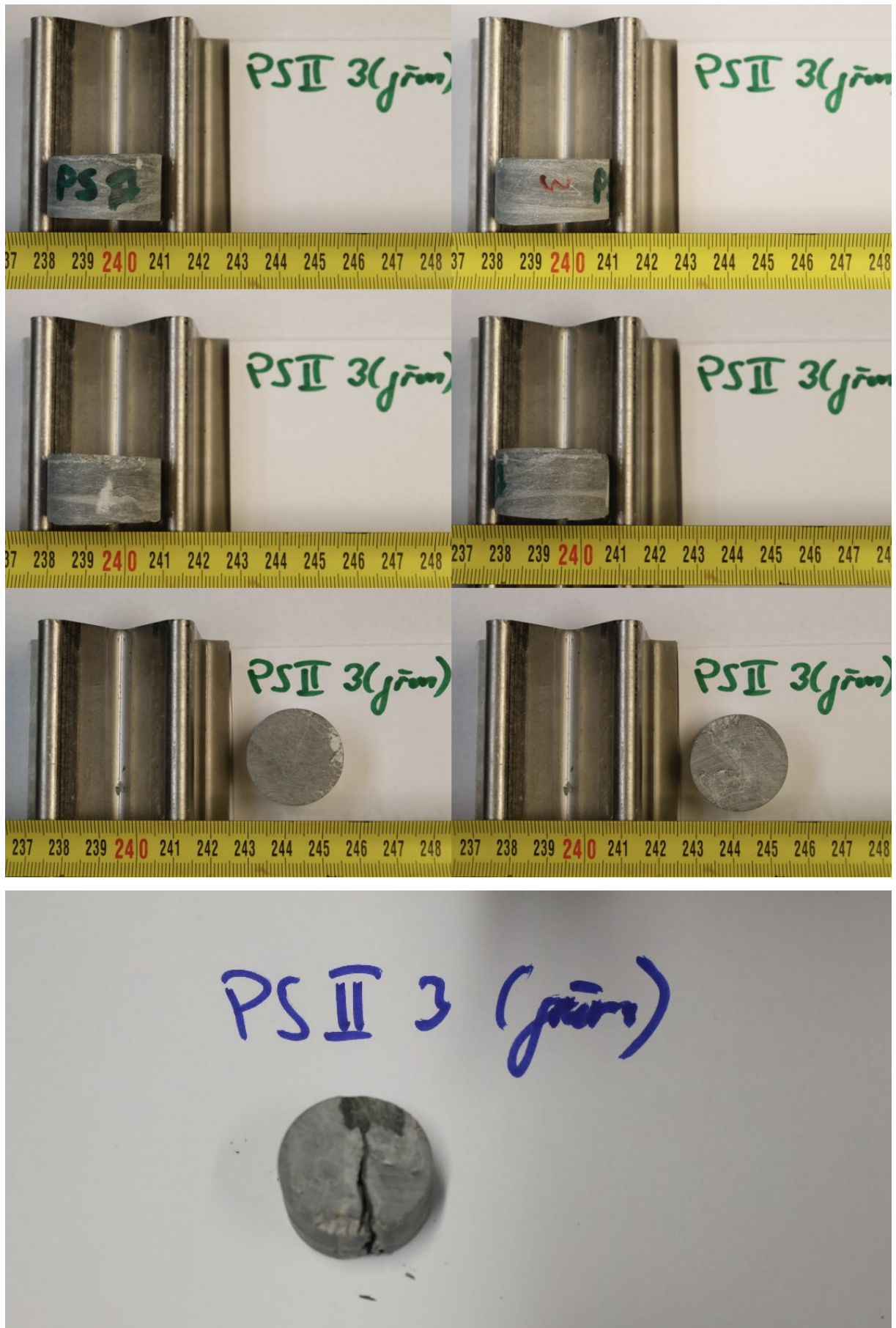


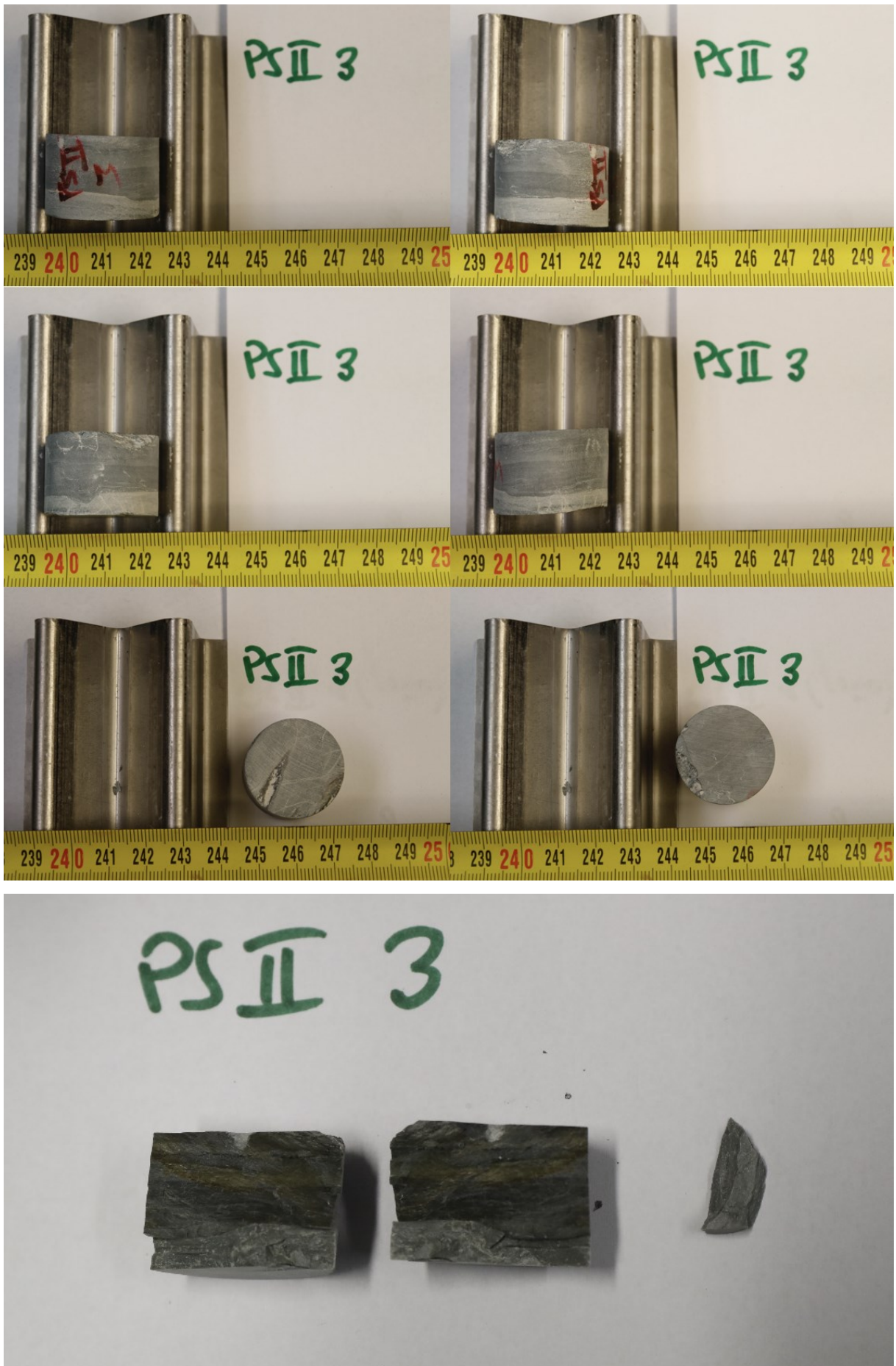


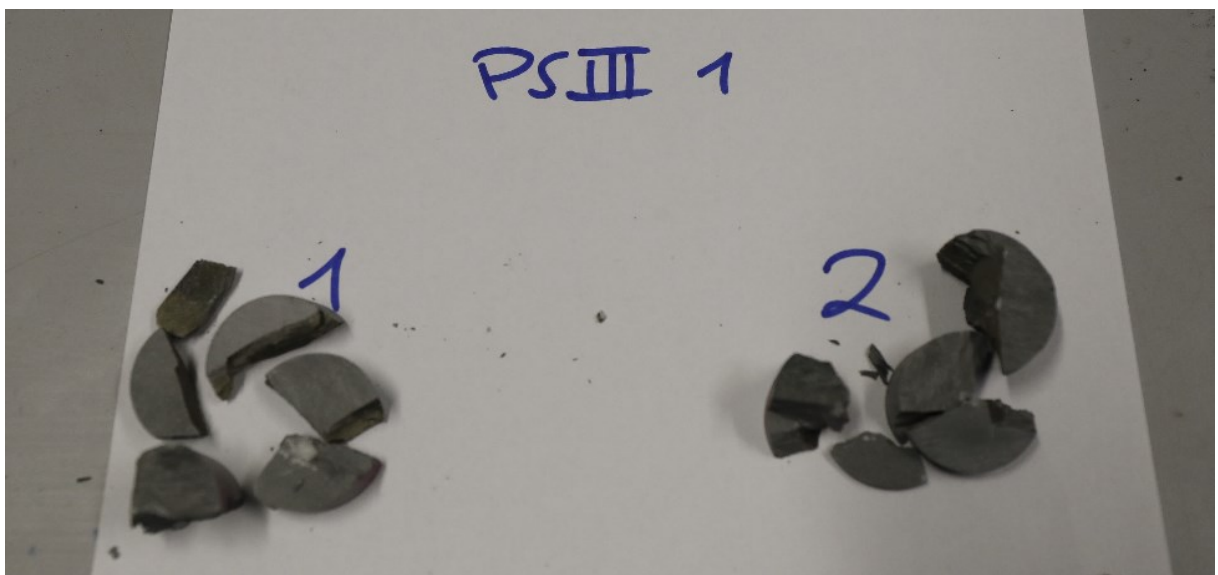
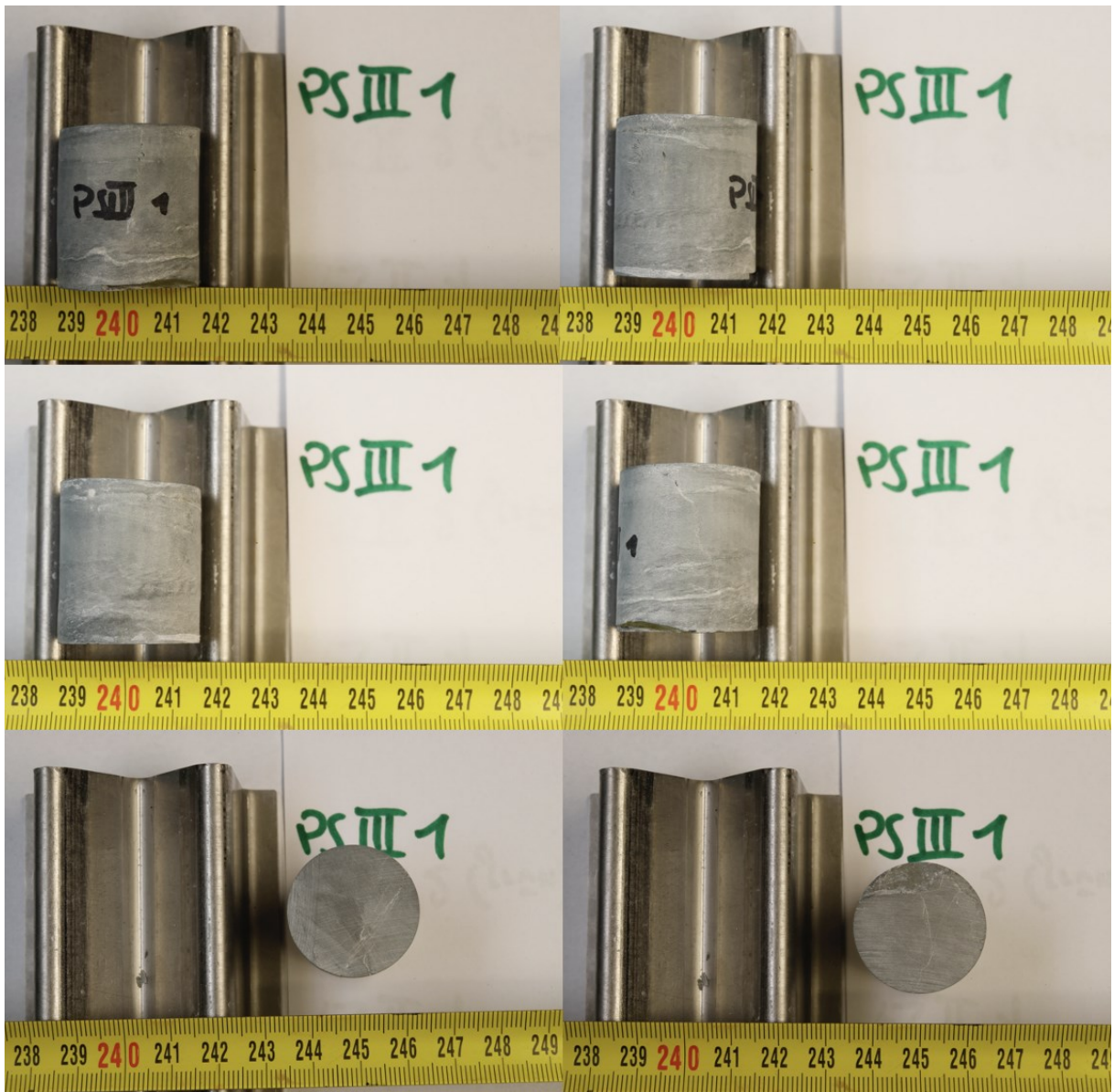


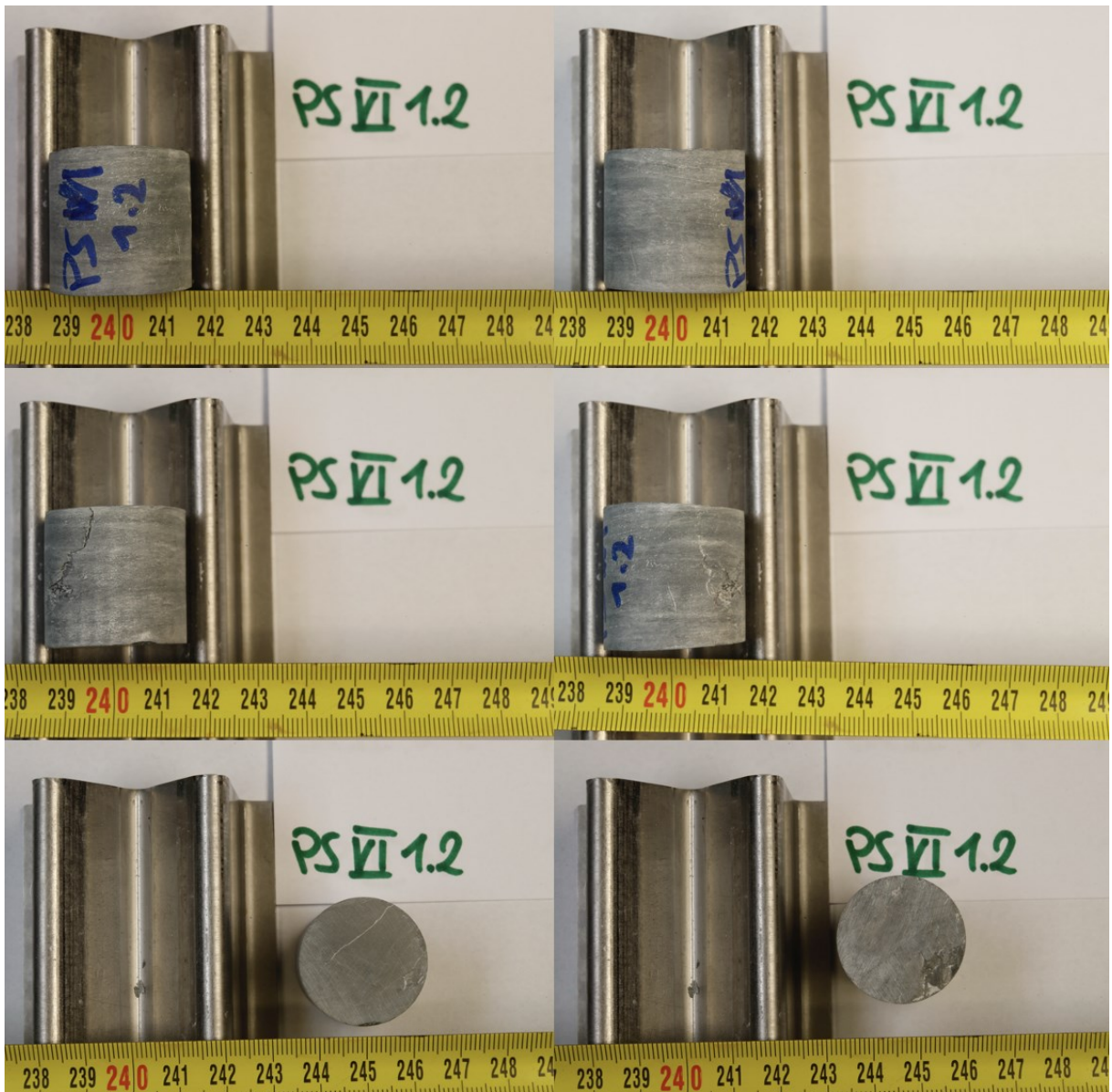


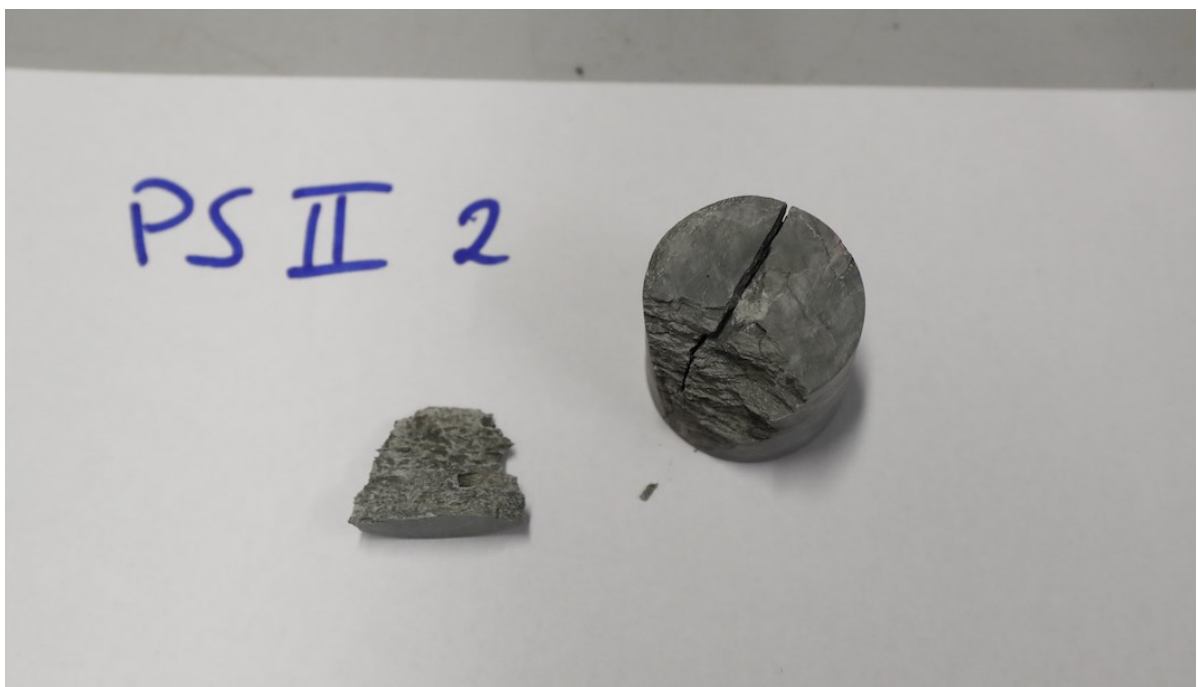
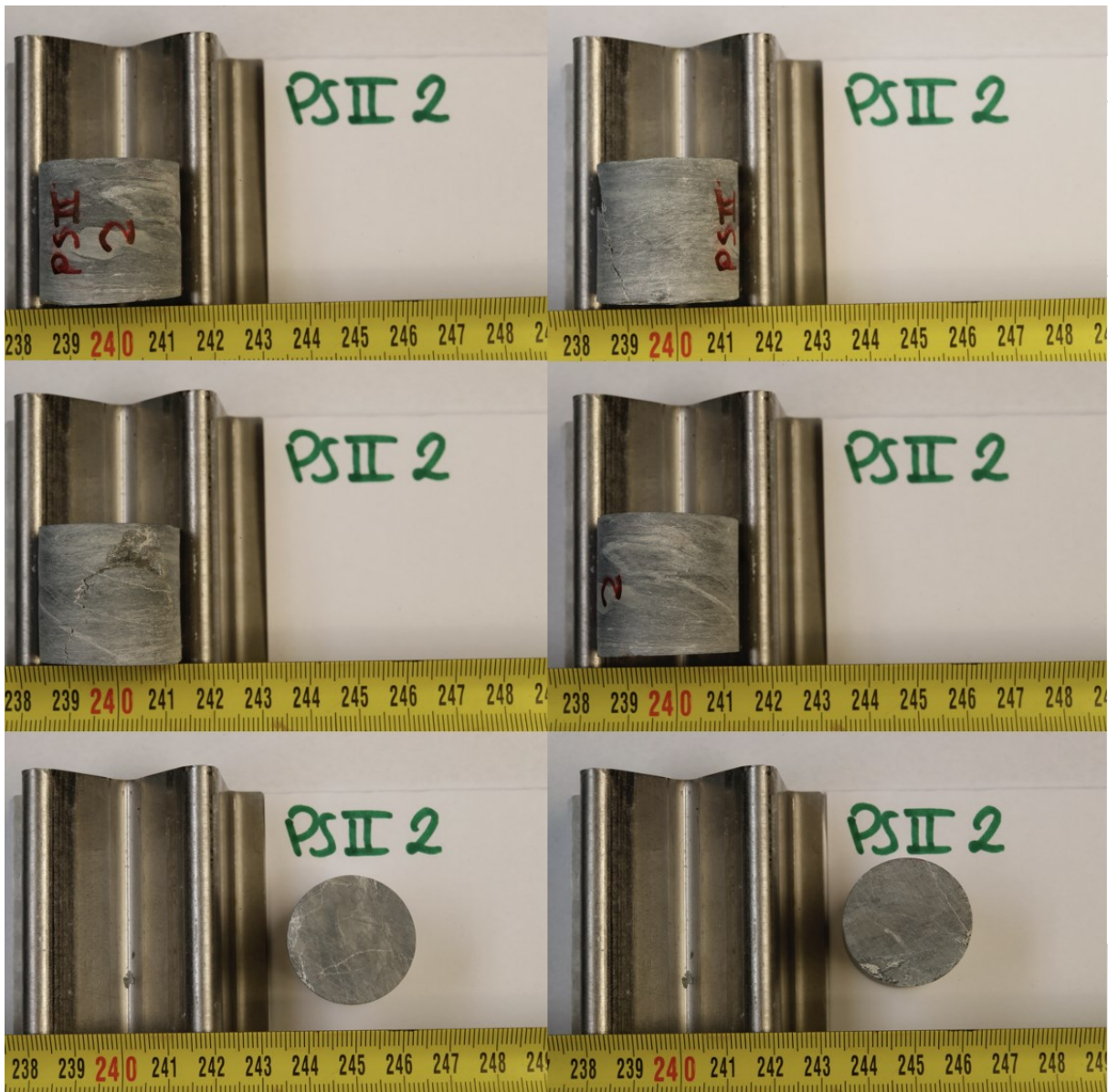


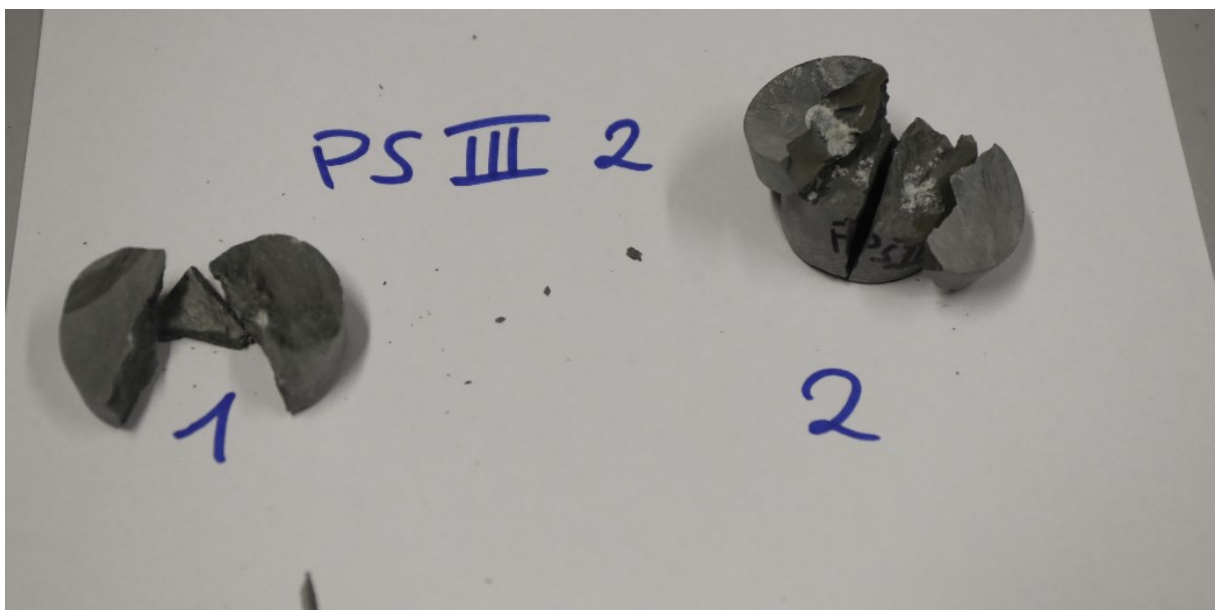
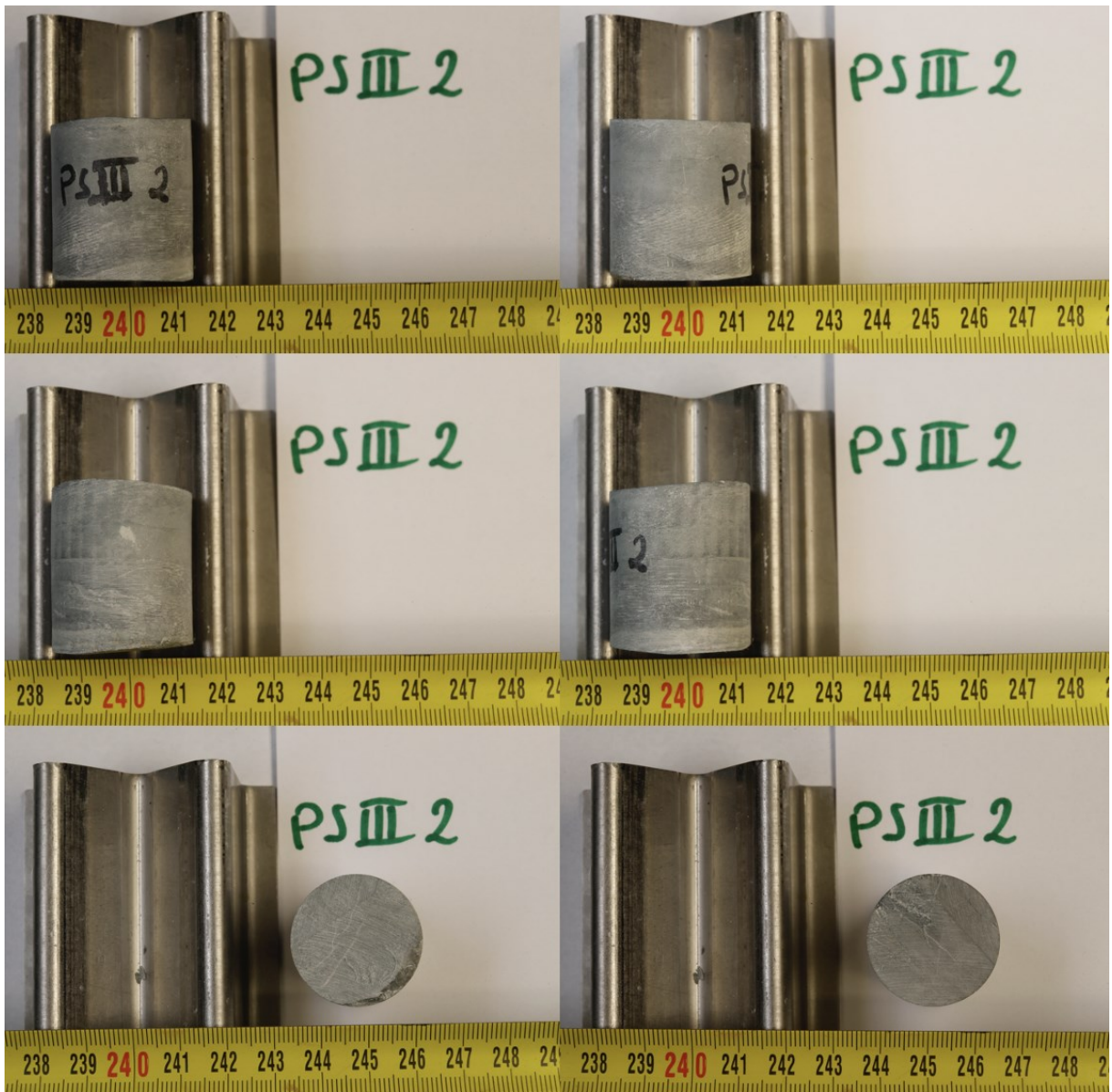


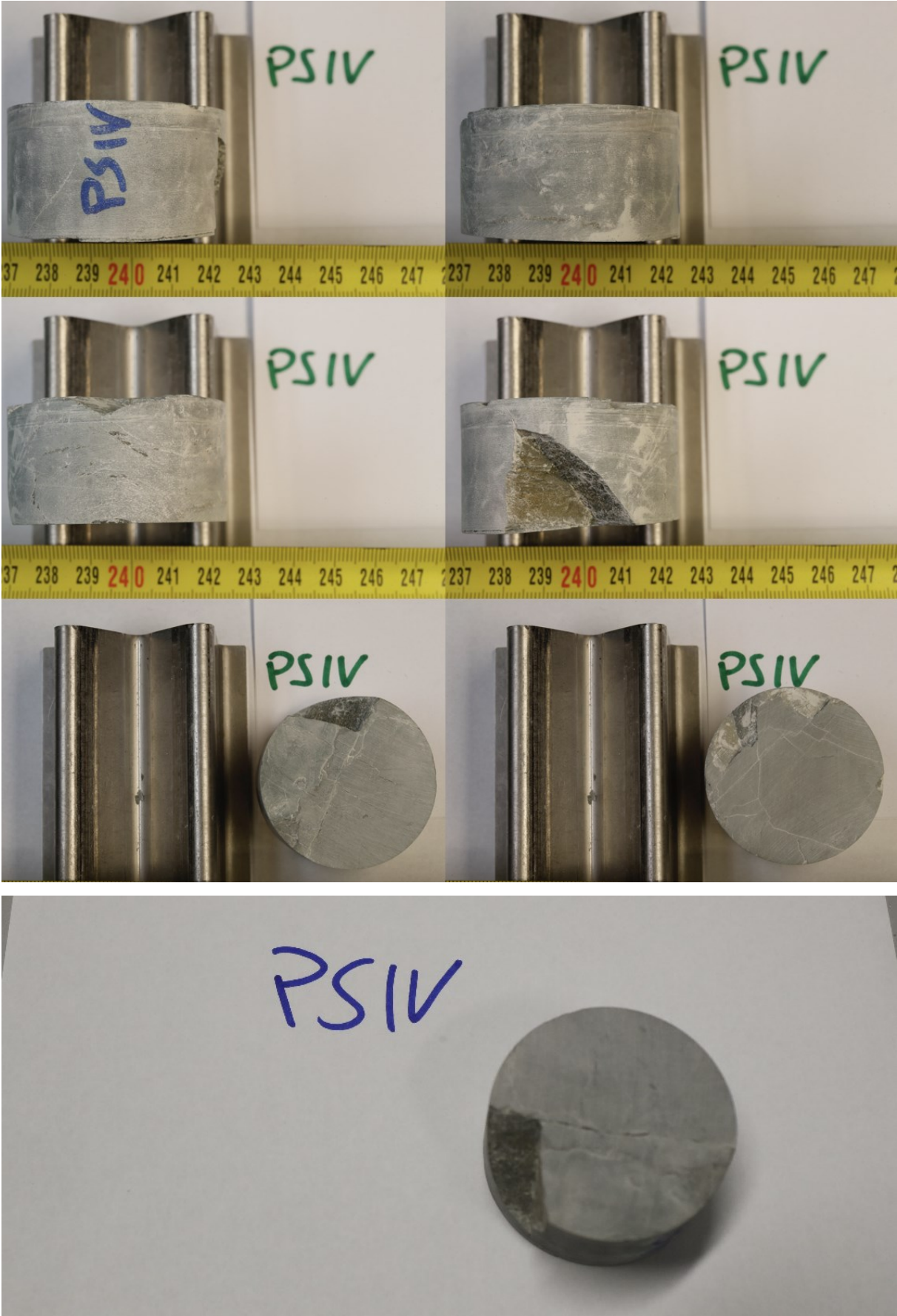


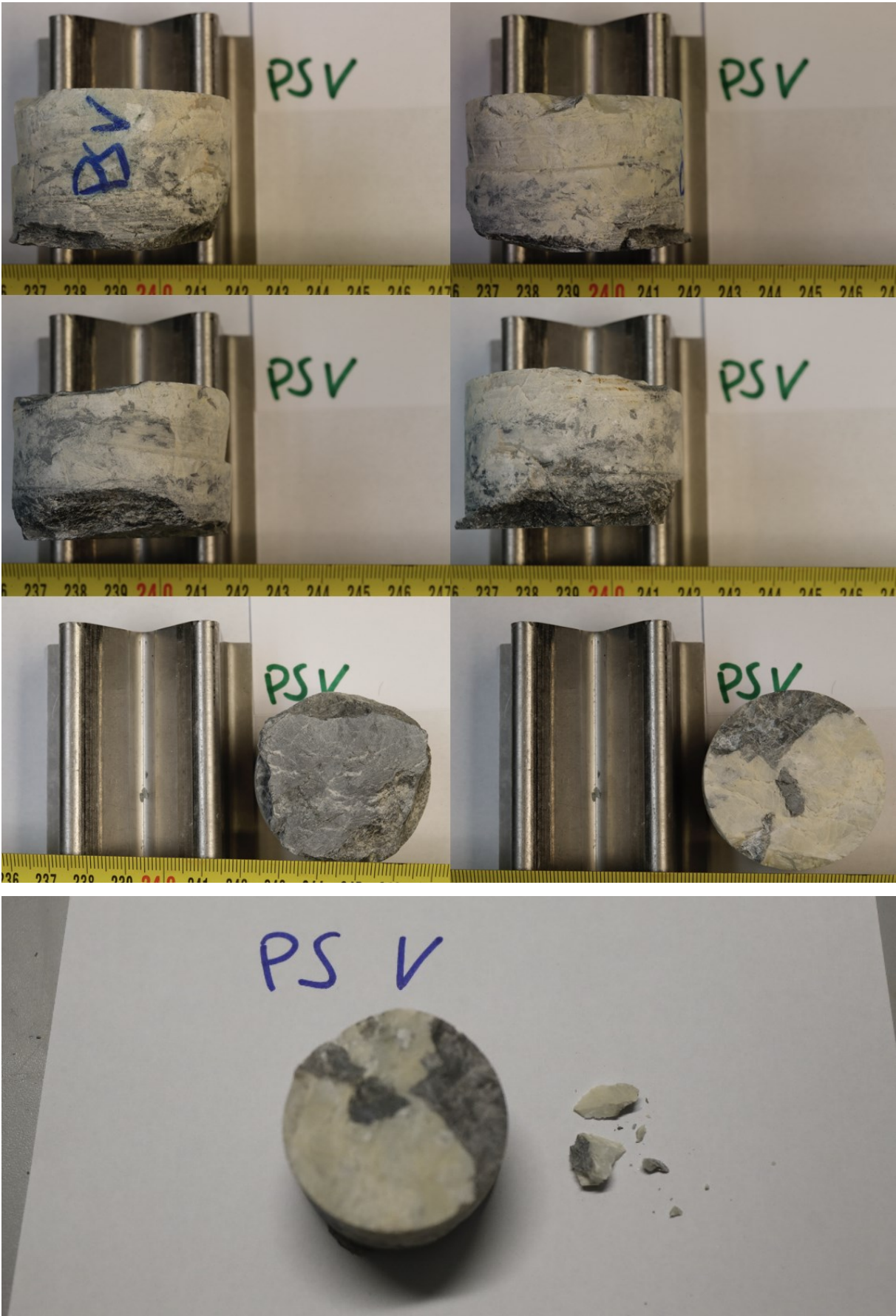












7.2. Appendix B: ERT Evaluation

Table 24: ERT Measurements - Evaluation

original data tx0	array type	remarks and filter details	N (rho<1)	N (dU%>2)	N filtered	dU % mean	rho min	rho mean	rho max	assessment	filtered data tx0
20231102ps1	We map 504		0	0	504	0,42	48	181	318	good	2023-11-02ps1
20231102ps2	PP map 4851		126	6	4719	0,16	1	163	347	good	2023-11-02ps2 F
20231207ps3test	We 1617	measured from e100 with booster at e60; stopped at m1482	87	53	1339	0,12	12	169	1458	bad data e1 to e40	
		bad contact of N to c2, N<41 deleted	1	1	1078	0,06	62	155	1372	pantslegs at e98	

		pantslegs of B at e98 deleted	0	0	1057	0,05	75	152	331	good	2023-12-07we F
20231207ps3tes t2	We 1617	stopped at m885	65	43	748	0,18	6	158	1219	bad data e1 to e40	
		bad contact of N to c2, N<41 deleted	1	17	549	0,10	75	144	333	exclude	
20231207ps3tes t3	DPD P 3370	measured from e100 with booster at e60; stopped at m1341	300	43	968	0,10	7	394	4290 8	bad data e1 to e40	
		bad contact of N to c2, N<41 deleted	0	1	852	0,05	43	143	371	exclude	
20231219ps3we	We 1617	measured from e100 with booster at e60	62	57	1445	0,12	6	156	1287	bad data e1 to e40	
		bad contact of N to c2, N<41 deleted	0	18	1199	0,06	75	158	320	good for ERT profile We	2023-12-19we F
20231219ps3pd p	PDP 1593	measured from e100 with booster at e60	50	63	1456	0,14	57	306	2921	bad data e1 to e40	

		bad contact of N to c2, N<41 deleted	1	39	1156	0,09	59	182	467	good for ERT profile PdP	2023-12- 19pdp F
2023-12-19	PDP 3186	measured between c2 and c3	497	259	2363	0,21	61	213	2775	bad data e1 to e40	
2023-12-19	PDP 3186	bad contact of N to c2, N<41 deleted	0	90	1806	0,10	61	170	404	good	2023-12- 19 F
2023-12-22	PDP 3186	N<41 deleted	1	111	1784	0,09	61	171	406	good	2023-12- 22 F
2023-12-25	PDP 3186	N<41 deleted	0	80	1816	0,09	61	171	407	good	2023-12- 25 F
2023-12-28	PDP 3186	N<41 deleted	0	90	1806	0,09	61	171	405	good	2023-12- 28 F
2023-12-31	PDP 3186	N<41 deleted	0	106	1790	0,10	61	171	404	good	2023-12- 31 F
2024-01-03	PDP 3186	N<41 deleted	0	102	1794	0,09	61	171	619	good	2024-01- 03 F
2024-01-06	PDP 3186	N<41 deleted	0	91	1805	0,09	61	171	406	good	2024-01- 06 F
2024-01-09	PDP 3186	N<41 deleted	3	90	1803	0,09	62	173	1669	exclude	

2024-01-12	PDP 3186	N<41 deleted	11	104	1781	0,09	61	173	1638	exclude	
2024-01-13	PDP 3186	N<41 deleted	21	94	1781	0,09	61	183	4973	exclude	
2024-01-14	PDP 3186	N<41 deleted, pants legs deleted	22	100	1774	0,09	61	184	5361	exclude	
2024-01-15	We 1617	measured from e1	718	172	727	0,31	4	109	1043	bad data e41 to e100	
2024-01-15	We 1617	bad contact of N at c2/c3; N>41 deleted	0	7	373	0,09	70	151	352	good	2024-01- 15 F
2024-01-16	We 1617	N>41 deleted	0	10	370	0,08	70	152	354	good	2024-01- 16 F
2024-01-17	We 1617	N>41 deleted	0	11	369	0,08	70	151	358	good	2024-01- 17 F
2024-01-18	We 1617	N>41 deleted	0	11	369	0,09	69	152	356	good	2024-01- 18 F
2024-01-19	We 1617	N>41 deleted	0	6	374	0,09	70	151	349	good	2024-01- 19 F
2024-01-20	We 1617	N>41 deleted	0	12	368	0,07	70	151	351	good	2024-01- 20 F

filtered data tx0	array type	remarks and filter details	N filtered	dU% mean	rho min	rho mean	rho max
2023-11-02ps1	We map		504	0,42	48	181	318
2023-11-02ps2 F	PP map		4719	0,16	1	163	347
2023-12-19we F	We	data from e41 to e100	1199	0,06	75	158	320
2024-01-21 F	We	data from e1 to e40	369	0,08	69	151	366
		combination e1 to e100	1568	0,06	69	156	366
2023-12-19pdp F	PdP	data from e41 to e100	1156	0,09	59	182	467
filtered data tx0	combined data tx0	inversion data file					
2023-11-02ps1		ERT map We.dat					
2023-11-02ps2 F		ERT map PP.dat					
2023-12-19we F							
2024-01-21 F							

	ERT profile We	ERT profile We Topo.dat					
2023-12-19pdp F		ERT profile PdP Topo.dat					

7.3.Appendix C: Steel Arches





















7.4. Appendix D: Deformation raw data

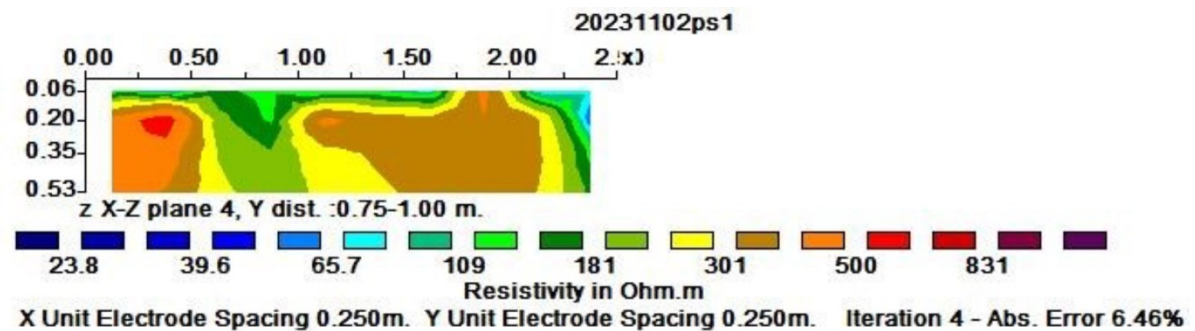
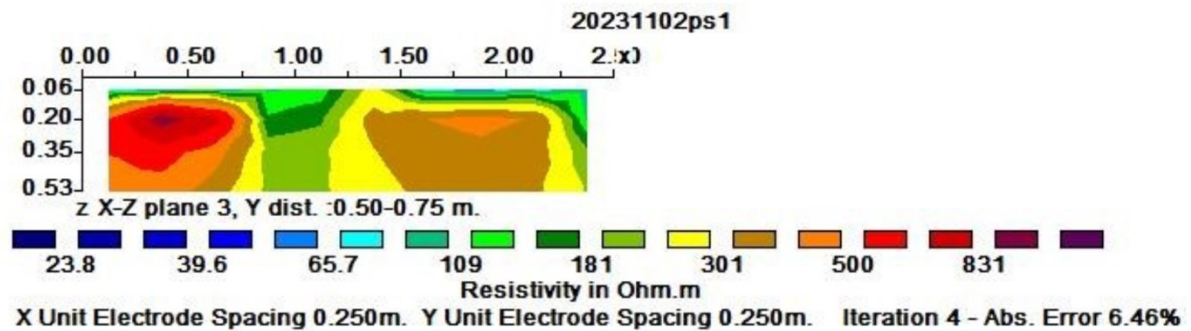
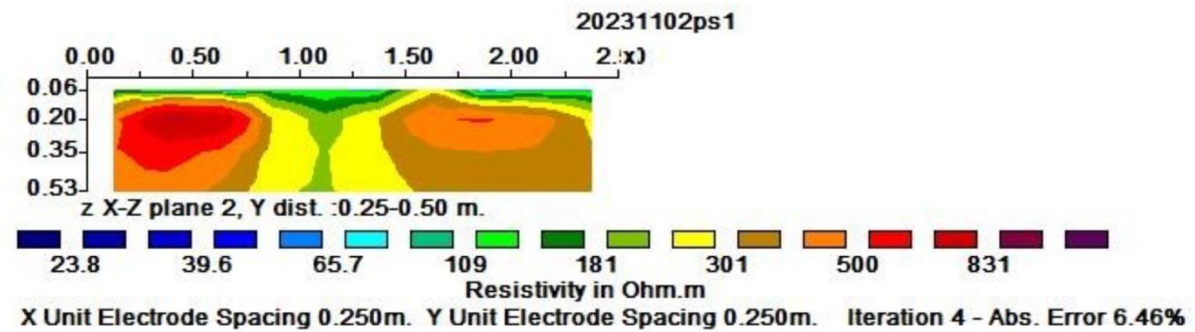
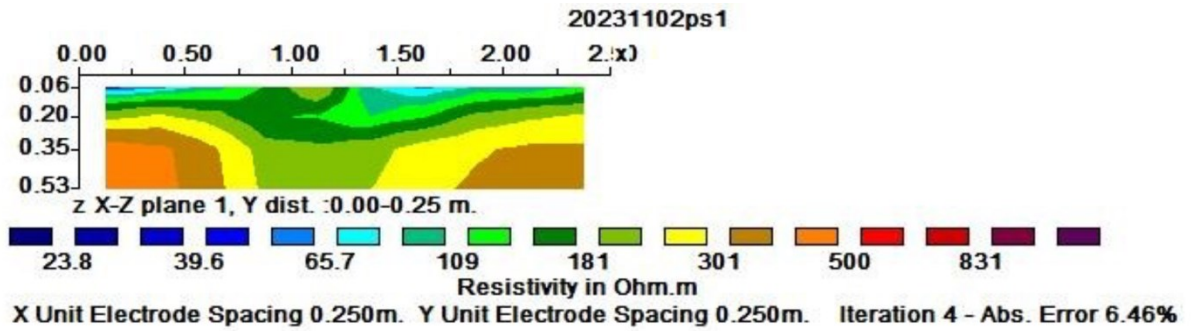
Tunnel meter	Arch Number	Deformation left arch	Deformation top arch	Deformation right arch	Left Arch	Top Arch	Right Arch
0	0	0	0	0			
0,51	1	2	1	2	2,7	1,3	2,3
1,04	2	3	2	3	2,3	1,5	2,5
1,57	3	3	1	2	2,2	1,6	2,6
2,1	4	1	2	3	2,2	2	2,8
2,63	5	2	2	3	2	2	2,6
3,16	6	2	3	3	2	2,2	2,4
3,69	7	2	2	2	2,4	2,4	2,4
4,22	8	3	2	1	2,4	2,4	2,2
4,75	9	3	3	3	2,2	2	1,8
5,26	10	2	2	2	2,2	2	1,8
5,77	11	1	1	1	2,2	2,2	1,8
6,28	12	2	2	2	2,2	2	1,6
6,79	13	3	3	1	2,4	2	1,6
7,3	14	3	2	2	2,8	2,2	1,6
7,81	15	3	2	2	2,8	2,2	1,4
8,3	16	3	2	1	2,6	2	1,4
8,79	17	2	2	1	2,4	2	1,4
9,28	18	2	2	1	2,2	2	1,6
9,77	19	2	2	2	2	2,2	1,8
10,26	20	2	2	3	1,8	2,6	2
10,75	21	2	3	2	1,8	3,2	2,2
11,24	22	1	4	2	2	3,6	2,2
11,73	23	2	5	2	2,4	4,2	1,8
12,22	24	3	4	2	2,6	4,4	1,8
12,71	25	4	5	1	3	4,4	1,8
13,2	26	3	4	2	3,2	4,4	1,8
13,71	27	3	4	2	3,2	4,6	1,8
14,22	28	3	5	2	3	4,6	2,2
14,73	29	3	5	2	2,8	4,4	2,6

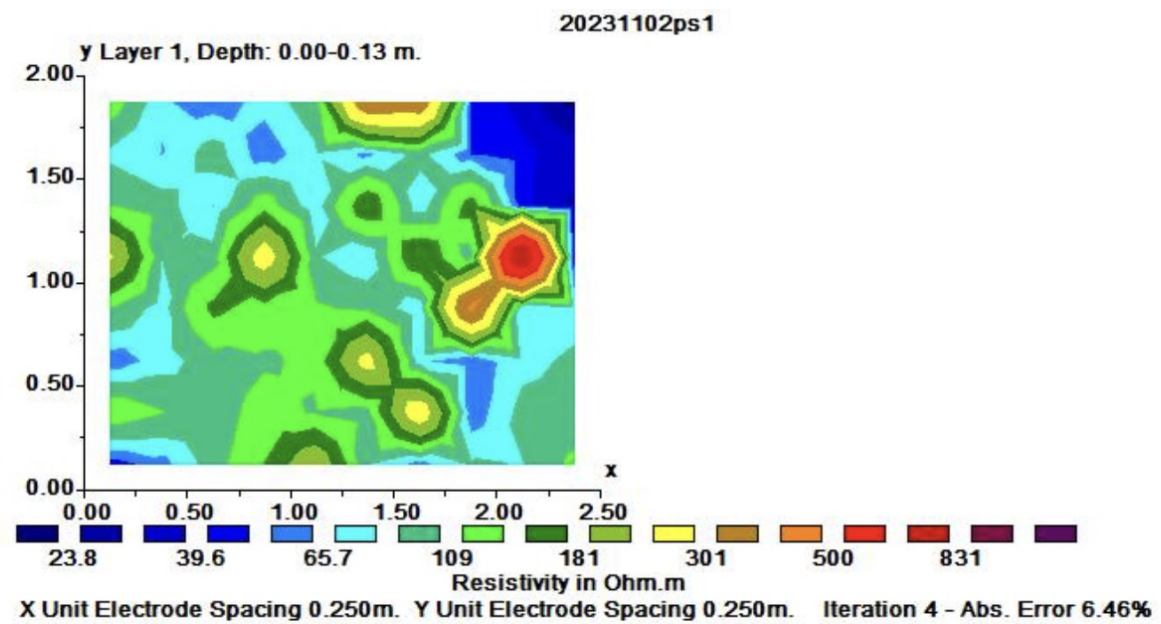
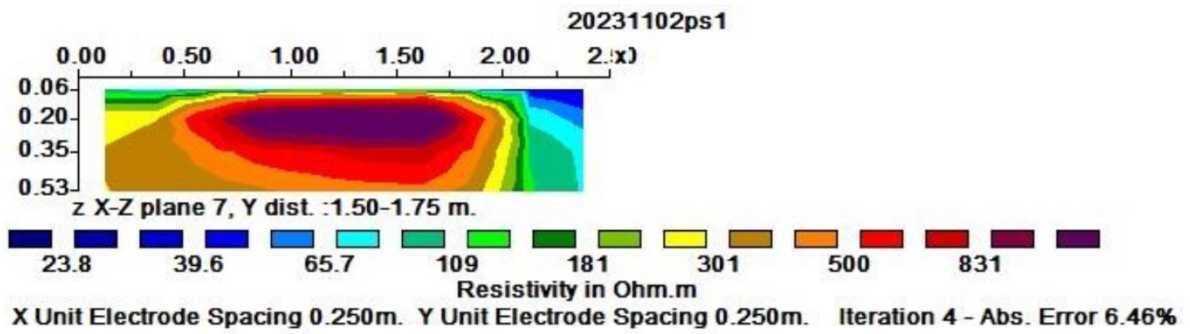
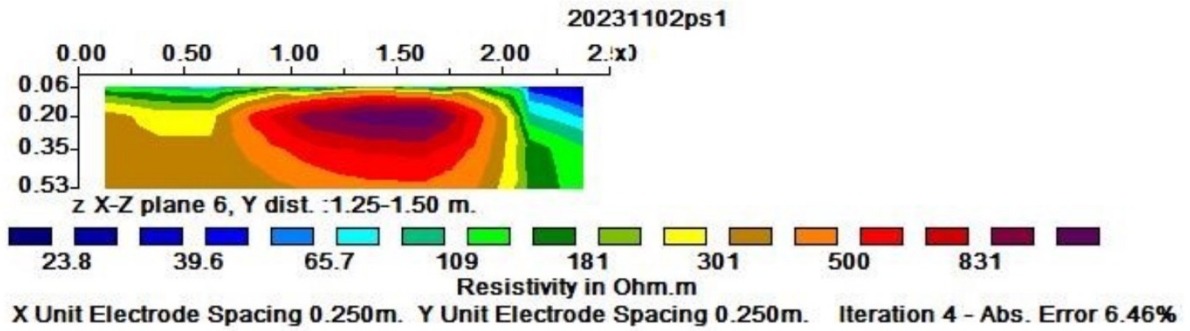
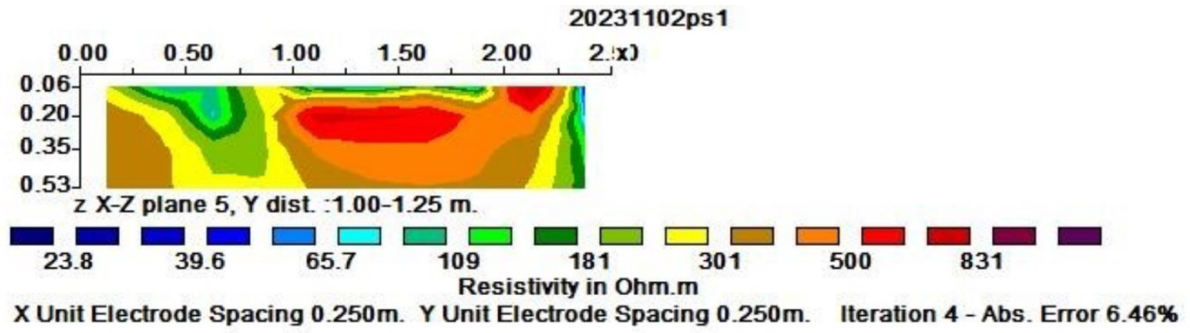
15,21	30	3	5	3	2,8	4	2,8
15,69	31	2	3	4	2,6	3,4	3
16,17	32	3	2	3	2,4	3,2	3,2
16,65	33	2	2	3	2,4	2,8	3
17,13	34	2	4	3	2,4	2,6	2,6
17,61	35	3	3	2	2,2	2,6	2,6
18,09	36	2	2	2	2,4	2,6	2,6
18,63	37	2	2	3	2,6	2,2	2,6
19,17	38	3	2	3	2,6	2	2,8
19,71	39	3	2	3	3	2	3
20,25	40	3	2	3	3,2	2	2,8
20,79	41	4	2	3	3,4	2,6	2,6
21,33	42	3	2	2	3,6	3	2,6
21,87	43	4	5	2	3,6	3,4	2,6
22,38	44	4	4	3	3,4	3,6	2,6
22,89	45	3	4	3	3,4	3,8	2,8
23,4	46	3	3	3	3,2	3,6	2,8
23,91	47	3	3	3	3	3,4	2,8
24,42	48	3	4	2	3	3,2	2,6
24,93	49	3	3	3	3	3,2	2,4
25,44	50	3	3	2	3	3,2	2,2
25,95	51	3	3	2	3,2	3,2	2,2
26,46	52	3	3	2	3,4	3,4	2
26,97	53	4	4	2	3,6	3,8	1,8
27,48	54	4	4	2	3,8	4	1,6
27,99	55	4	5	1	4	4,2	1,4
28,5	56	4	4	1	4	4	1,2
29,01	57	4	4	1	3,8	4	1
29,52	58	4	3	1	3,6	3,8	1
30,03	59	3	4	1	3,6	3,6	1
30,51	60	3	4	1	3,6	3,8	1,2
30,99	61	4	3	1	3,8	4	1,4
31,47	62	4	5	2	4	4,2	1,6

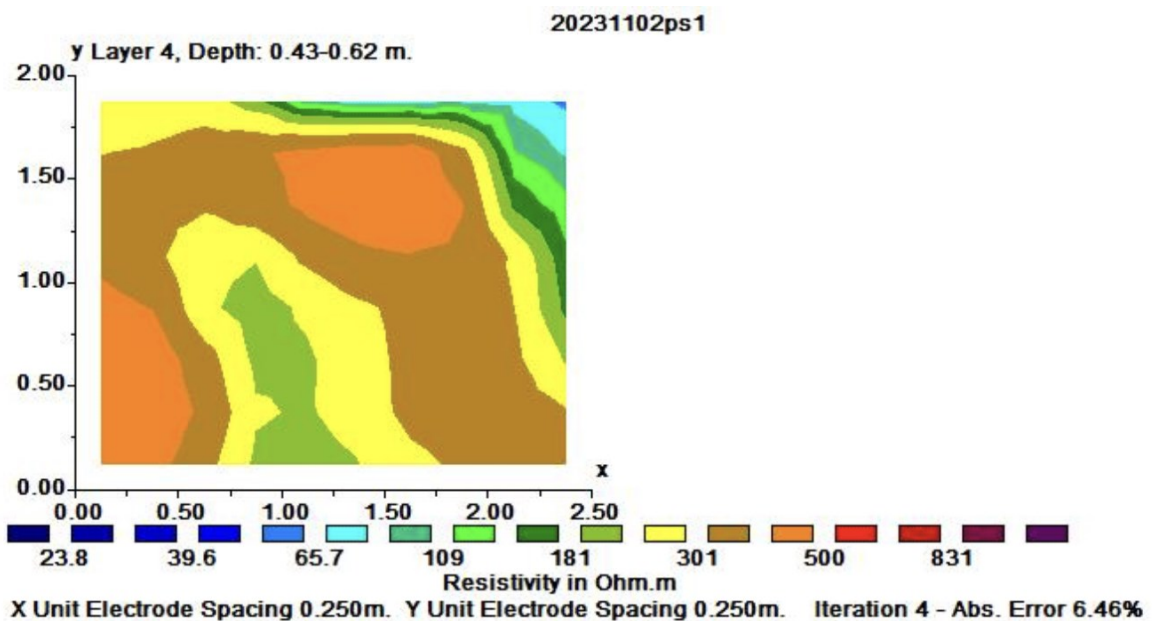
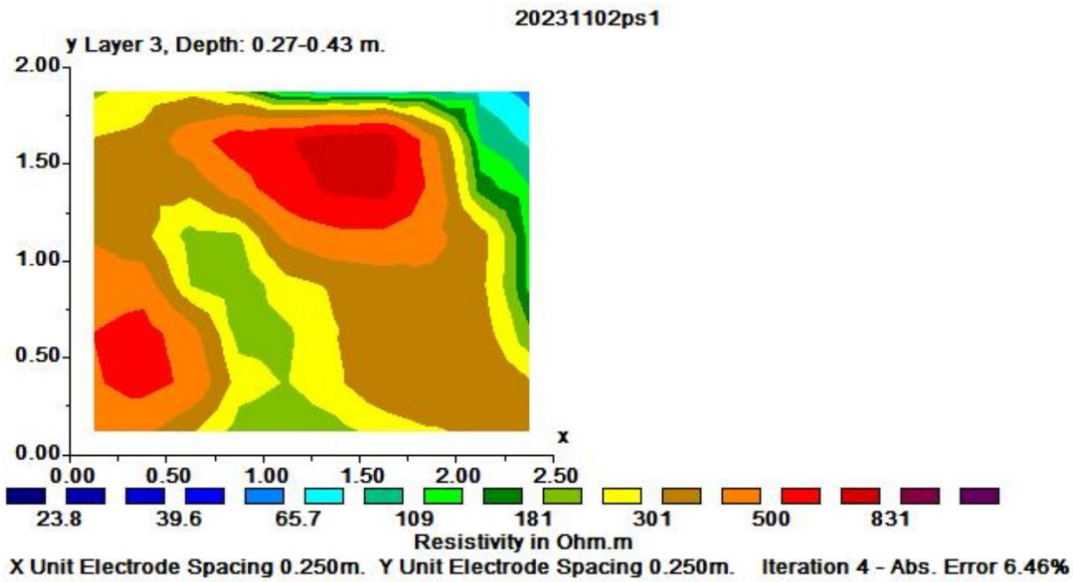
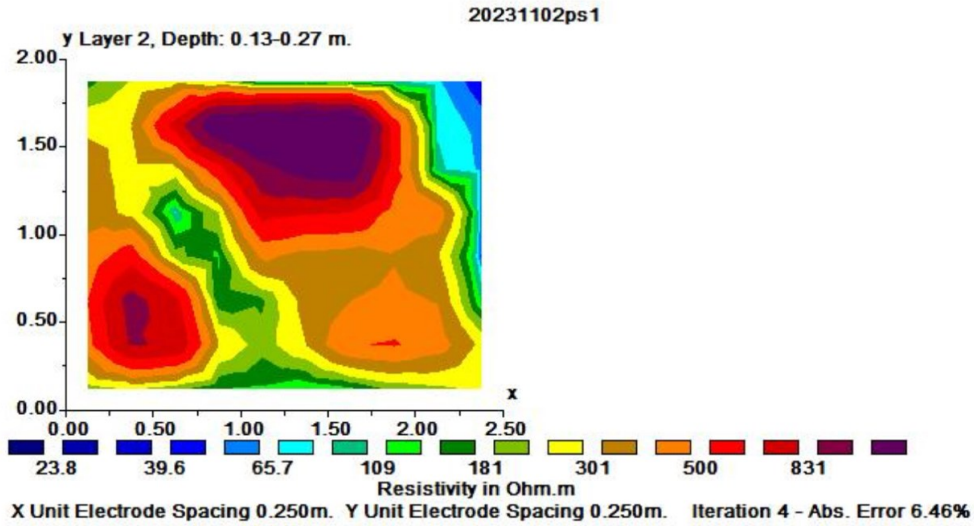
31,95	63	5	4	2	4	4,4	1,6
32,43	64	4	5	2	4,2	4,8	1,6
32,91	65	3	5	1	4,2	4,8	1,4
33,39	66	5	5	1	4	5	1,2
33,87	67	4	5	1	3,8	4,8	1,4
34,33	68	4	5	1	3,8	4,8	1,8
34,79	69	3	4	3	3,8	4,8	2,2
35,25	70	3	5	3	4	4,8	2,4
35,71	71	5	5	3	4	4,6	2,6
36,17	72	5	5	2	4,2	4,6	2,4
36,63	73	4	4	2	4,4	4,4	2,2
37,09	74	4	4	2	4,2	4	2,2
37,55	75	4	4	2	4,2	3,6	2,2
38,01	76	4	3	3	4,2	3,4	2,4
38,51	77	5	3	2	4	3,2	2,6
39,01	78	4	3	3	3,8	2,8	2,8
39,51	79	3	3	3	3,6	2,8	2,6
40,04	80	3	2	3	3,4	3	3
40,57	81	3	3	2	3,4	3	3
41,1	82	4	4	4	3,4	3,2	3,2
41,63	83	4	3	3	3,6	3,6	3,2
42,16	84	3	4	4	3,8	3,8	3,4
42,69	85	4	4	3	3,8	3,6	3
43,22	86	4	4	3	3,6	3,6	2,8
43,75	87	4	3	2	3,6	3,4	2,4
44,28	88	3	3	2	3,4	3,2	2,2
44,81	89	3	3	2	3,2	3	2
45,34	90	3	3	2	2,8	2,8	2
45,87	91	3	3	2	2,8	2,6	2
46,38	92	2	2	2	2,8	2,4	2
46,89	93	3	2	2	2,8	2,2	1,8
47,4	94	3	2	2	2,8	1,8	1,6
47,91	95	3	2	1	3	1,6	1,4

48,42	96	3	1	1	3	1,4	1,2
48,93	97	3	1	1	3	1,2	1
49,44	98	3	1	1	3	1	1
49,95	99	3	1	1	3	1	1
50,46	100	3	1	1	3	1	1
50,97	101	3	1	1	3	1	1

7.5. Appendix E: 3D ERT Tomography







7.6. Appendix F: CAI raw data

Table 25: CAI Raw Data PS III

Typ	Name	ID	Dokument	Länge (μm)	Winkel ($^{\circ}$)
4-Punkt- Winkel		1	Probe 1_Strich2_0.jpg		89,93
Horizontale Linie		2	Probe 1_Strich2_0.jpg	52,80	
4-Punkt- Winkel		1	Probe 1_Strich2_90.jpg		269,86
Horizontale Linie		2	Probe 1_Strich2_90.jpg	38,72	
4-Punkt- Winkel		1	Probe 1_Strich2_180.jpg		90,23
Horizontale Linie		2	Probe 1_Strich2_180.jpg	49,28	
4-Punkt- Winkel		1	Probe 1_Strich2_270.jpg		269,80
Horizontale Linie		2	Probe 1_Strich2_270.jpg	28,16	
4-Punkt- Winkel		1	Probe 1_Strich1_0.jpg		89,95
Horizontale Linie		2	Probe 1_Strich1_0.jpg	45,76	
4-Punkt- Winkel		1	Probe 1_Strich1_90.jpg		269,72
Horizontale Linie		2	Probe 1_Strich1_90.jpg	10,56	
4-Punkt- Winkel		1	Probe 1_Strich1_180.jpg		270,00
Horizontale Linie		2	Probe 1_Strich1_180.jpg	31,68	

4-Punkt- Winkel		1	Probe 1_Strich1_270.jpg		270,04
Horizontale Linie		2	Probe 1_Strich1_270.jpg	14,08	
4-Punkt- Winkel		1	Probe 1_Strich3_0.jpg		269,94
Horizontale Linie		2	Probe 1_Strich3_0.jpg	17,60	
4-Punkt- Winkel		1	Probe 1_Strich3_90.jpg		269,23
Horizontale Linie		2	Probe 1_Strich3_90.jpg	24,64	
4-Punkt- Winkel		1	Probe 1_Strich3_180.jpg		269,93
Horizontale Linie		2	Probe 1_Strich3_180.jpg	17,60	
4-Punkt- Winkel		1	Probe 1_Strich3_270.jpg		269,73
Horizontale Linie		2	Probe 1_Strich3_270.jpg	31,68	
4-Punkt- Winkel		1	Probe 1_Strich4_0.jpg		90,33
Horizontale Linie		2	Probe 1_Strich4_0.jpg	42,24	
4-Punkt- Winkel		1	Probe 1_Strich4_90.jpg		269,59
Horizontale Linie		2	Probe 1_Strich4_90.jpg	52,80	
4-Punkt- Winkel		1	Probe 1_Strich4_180.jpg		269,27
Horizontale Linie		2	Probe 1_Strich4_180.jpg	31,68	

4-Punkt- Winkel		1	Probe 1_Strich4_270.jpg	269,68
Horizontale Linie		2	Probe 1_Strich4_270.jpg	38,72
4-Punkt- Winkel		1	Probe 1_Strich5_0.jpg	89,71
Horizontale Linie		2	Probe 1_Strich5_0.jpg	24,64
4-Punkt- Winkel		1	Probe 1_Strich5_90.jpg	269,88
Horizontale Linie		2	Probe 1_Strich5_90.jpg	10,56
4-Punkt- Winkel		1	Probe 1_Strich5_180.jpg	269,67
Horizontale Linie		2	Probe 1_Strich5_180.jpg	31,68
4-Punkt- Winkel		1	Probe 1_Strich5_270.jpg	269,50
Horizontale Linie		2	Probe 1_Strich5_270.jpg	10,56
4-Punkt- Winkel		1	Probe 1_Strich6_0.jpg	269,48
Horizontale Linie		2	Probe 1_Strich6_0.jpg	21,12
4-Punkt- Winkel		1	Probe 1_Strich6_90.jpg	269,59
Horizontale Linie		2	Probe 1_Strich6_90.jpg	17,60
4-Punkt- Winkel		1	Probe 1_Strich6_180.jpg	269,73
Horizontale Linie		2	Probe 1_Strich6_180.jpg	17,60

4-Punkt-Winkel		1	Bild_11336		269,66
Horizontale Linie		2	Bild_11336	21,12	
Anzahl		48		24	24
Minimum		1,00		10,56	89,71
Maximum		2,00		52,80	270,04
Mittelwert		1,50		28,45	232,27
Standardabweichung		0,51		13,41	74,54

Table 26: CAI raw data PS VI_1 with schistosity

Typ	Name	ID	Dokument	Länge (μm)	Winkel ($^{\circ}$)
4-Punkt-Winkel		1	Strich1_0.jpg		89,71
Horizontale Linie		2	Strich1_0.jpg	28,16	
4-Punkt-Winkel		1	Strich1_90.jpg		89,97
Horizontale Linie		2	Strich1_90.jpg	49,28	
4-Punkt-Winkel		1	Strich1_180.jpg		89,98
Horizontale Linie		2	Strich1_180.jpg	38,72	
4-Punkt-Winkel		1	Strich1_270.jpg		89,70
Horizontale Linie		2	Strich1_270.jpg	35,20	
4-Punkt-Winkel		1	Strich2_0.jpg		90,01

Horizontale Linie		2	Strich2_0.jpg	28,16	
4-Punkt-Winkel		1	Strich2_90.jpg		89,88
Horizontale Linie		2	Strich2_90.jpg	35,20	
4-Punkt-Winkel		1	Strich2_180.jpg		89,91
Horizontale Linie		2	Strich2_180.jpg	38,72	
4-Punkt-Winkel		1	Strich2_270.jpg		89,71
Horizontale Linie		2	Strich2_270.jpg	31,68	
4-Punkt-Winkel		1	Strich3_0.jpg		90,10
Horizontale Linie		2	Strich3_0.jpg	35,20	
4-Punkt-Winkel		1	Strich3_90.jpg		89,81
Horizontale Linie		2	Strich3_90.jpg	17,60	
4-Punkt-Winkel		1	Strich3_180.jpg		89,75
Horizontale Linie		2	Strich3_180.jpg	28,16	
4-Punkt-Winkel		1	Strich3_270.jpg		89,75
Horizontale Linie		2	Strich3_270.jpg	31,68	
4-Punkt-Winkel		1	Frische Spritze.jpg		89,86

4-Punkt- Winkel		1	Strich4_0.jpg		89,94
Horizontale Linie		2	Strich4_0.jpg	38,72	
4-Punkt- Winkel		1	Strich4_90.jpg		89,26
Horizontale Linie		2	Strich4_90.jpg	31,68	
4-Punkt- Winkel		1	Strich4_180.jpg		89,78
Horizontale Linie		2	Strich4_180.jpg	31,68	
4-Punkt- Winkel		1	Strich4_270.jpg		89,15
Horizontale Linie		2	Strich4_270.jpg	35,20	
4-Punkt- Winkel		1	Strich5_0.jpg		89,77
Horizontale Linie		2	Strich5_0.jpg	24,64	
4-Punkt- Winkel		1	Strich5_90.jpg		89,76
Horizontale Linie		2	Strich5_90.jpg	24,64	
4-Punkt- Winkel		1	Strich5_180.jpg		89,91
Horizontale Linie		2	Strich5_180.jpg	35,20	
4-Punkt- Winkel		1	Bild_11499		89,31
Horizontale Linie		2	Bild_11499	31,68	

Anzahl		41		20	21
Minimum		1,00		17,60	89,15
Maximum		2,00		49,28	90,10
Mittelwert		1,49		32,56	89,76
Standardabweichung		0,51		6,65	0,25

Table 27: CAI raw data PS VI_2 against schistosity

Typ	Name	ID	Dokument	Länge (μm)	Winkel ($^{\circ}$)
4-Punkt- Winkel		1	Strich1_0.jpg		89,91
Horizontale Linie		2	Strich1_0.jpg	84,48	
4-Punkt- Winkel		1	Strich1_90.jpg		270,00
Horizontale Linie		2	Strich1_90.jpg	77,44	
4-Punkt- Winkel		1	Strich1_180.jpg		270,38
Horizontale Linie		2	Strich1_180.jpg	80,96	
4-Punkt- Winkel		1	Strich1_270.jpg		269,73
Horizontale Linie		2	Strich1_270.jpg	84,48	
4-Punkt- Winkel		1	Strich2_0.jpg		269,60
Horizontale Linie		2	Strich2_0.jpg	42,24	
4-Punkt- Winkel		1	Strich2_90.jpg		269,50
4-Punkt- Winkel		1	Strich2_180.jpg		268,59

Horizontale Linie		2	Strich2_180.jpg	35,20	
4-Punkt-Winkel		1	Strich2_270.jpg		269,86
Horizontale Linie		2	Strich2_270.jpg	10,56	
Horizontale Linie		2	Strich2_90.jpg	10,56	
4-Punkt-Winkel		1	Strich3_0.jpg		269,55
Horizontale Linie		2	Strich3_0.jpg	21,12	
4-Punkt-Winkel		1	Strich3_90.jpg		269,61
Horizontale Linie		2	Strich3_90.jpg	63,36	
4-Punkt-Winkel		1	Strich3_180.jpg		269,31
Horizontale Linie		2	Strich3_180.jpg	14,08	
4-Punkt-Winkel		1	Strich3_270.jpg		89,82
Horizontale Linie		2	Strich3_270.jpg	59,84	
4-Punkt-Winkel		1	Strich4_0.jpg		269,81
Horizontale Linie		2	Strich4_0.jpg	140,80	
4-Punkt-Winkel		1	Strich4_90.jpg		269,99
Horizontale Linie		2	Strich4_90.jpg	168,96	

4-Punkt- Winkel		1	Strich4_180.jpg		269,36
Horizontale Linie		2	Strich4_180.jpg	123,20	
4-Punkt- Winkel		1	Strich4_270.jpg		269,76
Horizontale Linie		2	Strich4_270.jpg	133,76	
4-Punkt- Winkel		1	Strich5_0.jpg		269,93
Horizontale Linie		2	Strich5_0.jpg	137,28	
4-Punkt- Winkel		1	Strich5_90.jpg		269,34
Horizontale Linie		2	Strich5_90.jpg	334,40	
4-Punkt- Winkel		1	Strich5_180.jpg		269,48
Horizontale Linie		2	Strich5_180.jpg	137,28	
4-Punkt- Winkel		1	Bild_11386		269,47
Horizontale Linie		2	Bild_11386	323,84	
Anzahl		40		20	20
Minimum		1,00		10,56	89,82
Maximum		2,00		334,40	270,38
Mittelwert		1,50		104,19	251,65
Standardabweichung		0,51		90,91	55,33

7.7. Appendix G: Sieving raw data

Korngrößenverteilung ÖNORM B 4412	
Datum	20.11.23
Versuch durchgeführt von	Dominik Kumertz, BSc
Probe	Presserstollen: 2b
Behältermasse	262 [g]
Feuchtmasse + Behälter	3904 [g]
Trockenmasse + Behältermasse	3833 [g]
Trockenmasse	3571 [g]

Korngröße	Tara	Masse Siebrückst. + Tara	Masse Siebrückstand	Siebrückstand	Summe der Siebdurchgänge
[mm]	[g]	[g]	[g]	[%]	[%]
31,5	4,9	0,0	0,0	0,00	100,00
16	4,9	330,4	325,5	9,12	90,88
8	4,9	1066,7	1061,8	29,73	61,15
4	4,9	979,8	974,9	27,30	33,85
2	4,9	511,5	506,6	14,19	19,66
1	4,9	282,3	277,4	7,77	11,89
0,5	4,9	158,1	153,2	4,29	7,60
0,25	4,9	274,6	269,7	7,55	0,05
0,125	0,0	0,0	0,0	0,00	0,05
0,063	0,0	0,0	0,0	0,00	0,05
< 0,063	0,0	0,0	0,0	0,00	0,05
Summe	3569,2	3603,5	3569,2	99,95	
Siebverlust	1,81	[g]	0,05%		

Korngrößenverteilung ÖNORM B 4412	
Datum	20.11.23
Versuch durchgeführt von	Dominik Kumertz, BSc
Probe	Presserstollen: 2b
Behältermasse	355,8 [g]
Feuchtmasse + Behälter	2886 [g]
Trockenmasse + Behältermasse	2664 [g]
Trockenmasse	2308,2 [g]

Korngröße	Tara	Masse Siebrückst. + Tara	Masse Siebrückstand	Siebrückstand	Summe der Siebdurchgänge
[mm]	[g]	[g]	[g]	[%]	[%]
31,5	4,9	0,0	0,0	0,00	100,00
16	4,9	255,2	250,3	10,85	89,15
8	4,9	542,8	537,9	23,31	65,85
4	4,9	380,5	375,6	16,27	49,58
2	4,9	303,1	298,2	12,92	36,66
1	4,9	263,5	258,6	11,21	25,45
0,5	4,9	196,1	191,2	8,28	17,17
0,25	4,9	394,6	389,7	16,88	0,29
0,125	0,0	0,0	0,0	0,00	0,29
0,063	0,0	0,0	0,0	0,00	0,29
< 0,063	0,0	0,0	0,0	0,00	0,29
Summe	2301,46	2335,8	2301,5	99,71	
Siebverlust	6,74	[g]	0,29%		

Korngrößenverteilung ÖNORM B 4412	
Datum	20.11.23
Versuch durchgeführt von	Dominik Kumertz, BSc
Probe	Presserstollen: 2b
Behältermasse	262,3 [g]
Feuchtmasse + Behälter	3069 [g]
Trockenmasse + Behältermasse	2878 [g]
Trockenmasse	2615,7 [g]

Korngröße	Tara	Masse Siebrückst. + Tara	Masse Siebrückstand	Siebrückstand	Summe der Siebdurchgänge
[mm]	[g]	[g]	[g]	[%]	[%]
31,5	4,9	295,6	290,7	11,11	88,89
16	4,9	367,4	362,5	13,86	75,03
8	4,9	410,8	405,9	15,52	59,51
4	4,9	468,2	463,3	17,71	41,80
2	4,9	377,9	373,0	14,26	27,54
1	4,9	293,7	288,8	11,04	16,50
0,5	4,9	189,3	184,4	7,05	9,45
0,25	4,9	251,7	246,8	9,44	0,02
0,125	0,0	0,0	0,0	0,00	0,02
0,063	0,0	0,0	0,0	0,00	0,02
< 0,063	0,0	0,0	0,0	0,00	0,02
Summe	2615,3	2654,5	2615,3	99,98	
Siebverlust	0,43	[g]	0,02%		

Korngrößenverteilung ÖNORM B 4412	
Datum	20.11.23
Versuch durchgeführt von	Dominik Kumertz, BSc
Probe	Presserstollen: 2b
Behältermasse	264,3 [g]
Feuchtmasse + Behälter	3123 [g]
Trockenmasse + Behältermasse	3000 [g]
Trockenmasse	2735,7 [g]

Korngröße	Tara	Masse Siebrückst. + Tara	Masse Siebrückstand	Siebrückstand	Summe der Siebdurchgänge
[mm]	[g]	[g]	[g]	[%]	[%]
31,5	4,9	109,2	104,3	3,81	96,19
16	4,9	542,5	537,6	19,65	76,54
8	4,9	746,8	741,9	27,12	49,42
4	4,9	524,2	519,3	18,98	30,44
2	4,9	330,0	325,1	11,88	18,55
1	4,9	213,1	208,2	7,61	10,94
0,5	4,9	114,1	109,2	3,99	6,95
0,25	4,9	194,1	189,2	6,92	0,04
0,125	0,0	0,0	0,0	0,00	0,04
0,063	0,0	0,0	0,0	0,00	0,04
< 0,063	0,0	0,0	0,0	0,00	0,04
Summe	2734,7	2773,9	2734,7	99,96	
Siebverlust	0,974	[g]	0,04%		

Korngrößenverteilung ÖNORM B 4412	
Datum	20.11.23
Versuch durchgeführt von	Dominik Kumertz, BSc
Probe	Presserstollen: 2b
Behältermasse	465,5 [g]
Feuchtmasse + Behälter	2949,3 [g]
Trockenmasse + Behältermasse	2681 [g]
Trockenmasse	2215,5 [g]

Korngröße	Tara	Masse Siebrückst. + Tara	Masse Siebrückstand	Siebrückstand	Summe der Siebdurchgänge
[mm]	[g]	[g]	[g]	[%]	[%]
31,5	4,9	0,0	0,0	0,00	100,00
16	4,9	73,5	68,6	3,10	96,90
8	4,9	102,0	97,1	4,38	92,52
4	4,9	273,8	268,9	12,14	80,39
2	4,9	359,2	354,3	15,99	64,40
1	4,9	348,3	343,4	15,50	48,90
0,5	4,9	365,6	360,7	16,28	32,61
0,25	4,9	724,2	719,3	32,47	0,15
0,125	0,0	0,0	0,0	0,00	0,15
0,063	0,0	0,0	0,0	0,00	0,15
< 0,063	0,0	0,0	0,0	0,00	0,15
Summe	2212,2	2246,5	2212,2	99,85	
Siebverlust	3,3	[g]	0,15%		

Korngrößenverteilung ÖNORM B 4412	
Datum	20.11.23
Versuch durchgeführt von	Dominik Kumertz, BSc
Probe	Presserstollen: 2b
Behältermasse	267,7 [g]
Feuchtmasse + Behälter	2388,3 [g]
Trockenmasse + Behältermasse	2239 [g]
Trockenmasse	1971,3 [g]

Korngröße	Tara	Masse Siebrückst. + Tara	Masse Siebrückstand	Siebrückstand	Summe der Siebdurchgänge
[mm]	[g]	[g]	[g]	[%]	[%]
31,5	4,9	124,7	119,8	6,07	93,93
16	4,9	391,4	386,5	19,61	74,32
8	4,9	350,5	345,6	17,53	56,79
4	4,9	311,6	306,7	15,56	41,23
2	4,9	235,5	230,6	11,70	29,53
1	4,9	188,4	183,5	9,31	20,22
0,5	4,9	136,3	131,4	6,67	13,56
0,25	4,9	266,8	261,9	13,28	0,27
0,125	0,0	0,0	0,0	0,00	0,27
0,063	0,0	0,0	0,0	0,00	0,27
< 0,063	0,0	0,0	0,0	0,00	0,27
Summe	1966,0	2005,2	1966,0	99,73	
Siebverlust	5,34	[g]	0,27%		

Korngrößenverteilung ÖNORM B 4412	
Datum	20.11.23
Versuch durchgeführt von	Dominik Kumertz, BSc
Probe	Presserstollen: 2b
Behältermasse	671,4 [g]
Feuchtmasse Behälter +	3377 [g]
Trockenmasse Behältermasse +	3205 [g]
Trockenmasse	2533,6 [g]

Korngröße	Tara	Masse Siebrückst. + Tara	Masse Siebrückstand	Siebrückstand	Summe der Siebdurchgänge
[mm]	[g]	[g]	[g]	[%]	[%]
31,5	4,9	0,0	0,0	0,00	100,00
16	4,9	142,8	137,9	5,44	94,56
8	4,9	473,7	468,8	18,50	76,05
4	4,9	472,0	467,1	18,44	57,62
2	4,9	524,9	520,0	20,52	37,09
1	4,9	377,2	372,3	14,69	22,40
0,5	4,9	223,8	218,9	8,64	13,76
0,25	4,9	351,4	346,5	13,67	0,09
0,125	0,0	0,0	0,0	0,00	0,09
0,063	0,0	0,0	0,0	0,00	0,09
< 0,063	0,0	0,0	0,0	0,00	0,09
Summe	2531,4	2565,7	2531,4	99,91	
Siebverlust	2,18	[g]	0,09%		

Korngrößenverteilung ÖNORM B 4412	
Datum	20.11.23
Versuch durchgeführt von	Dominik Kumertz, BSc
Probe	Presserstollen: 2b
Behältermasse	338,3 [g]
Feuchtmasse + Behälter	3079,1 [g]
Trockenmasse + Behältermasse	2947 [g]
Trockenmasse	2608,7 [g]

Korngröße	Tara	Masse Siebrückst. + Tara	Masse Siebrückstand	Siebrückstand	Summe der Siebdurchgänge
[mm]	[g]	[g]	[g]	[%]	[%]
31,5	4,9	82,2	77,3	2,96	97,04
16	4,9	354,9	350,0	13,42	83,62
8	4,9	921,9	917,0	35,15	48,47
4	4,9	533,0	528,1	20,24	28,23
2	4,9	270,0	265,1	10,16	18,06
1	4,9	156,9	152,0	5,83	12,24
0,5	4,9	105,9	101,0	3,87	8,36
0,25	4,9	221,8	216,9	8,32	0,05
0,125	0,0	0,0	0,0	0,00	0,05
0,063	0,0	0,0	0,0	0,00	0,05
< 0,063	0,0	0,0	0,0	0,00	0,05
Summe	2607,5	2646,7	2607,5	99,95	
Siebverlust	1,25	[g]	0,05%		